A 6DOF SIMULATION TOOL FOR AUTONOMOUS UNDERWATER VEHICLES WITH A NOVEL METHOD FOR ADDED MASS-INERTIA CALCULATION

A THESIS SUBMITTED TO
THE GRADUATE SCHOOL OF NATURAL AND APPLIED SCIENCES
OF
MIDDLE EAST TECHNICAL UNIVERSITY

BY

OĞUZHAN TAŞ

IN PARTIAL FULFILLMENT OF THE REQUIREMENTS
FOR
THE DEGREE OF MASTER OF SCIENCE
IN
MECHANICAL ENGINEERING

SEPTEMBER 2018

Approval of the thesis:

A 6DOF SIMULATION TOOL FOR AUTONOMOUS UNDERWATER VEHICLES WITH A NOVEL METHOD FOR ADDED MASS-INERTIA CALCULATION

submitted by **OĞUZHAN TAŞ** in partial fulfillment of the requirements for the degree of **Master of Science in Mechanical Engineering Department, Middle East Technical University** by,

Prof. Dr. Halil Kalıpçılar _____
Dean, Graduate School of **Natural and Applied Sciences**

Prof. Dr. M.A. Sahir Arıkan _____
Head of Department, **Mechanical Engineering**

Assist. Prof. Dr. Özgür Uğraş Baran _____
Supervisor, **Mechanical Engineering Department, METU**

Examining Committee Members:

Prof. Dr. Mehmet Haluk Aksel
Mechanical Engineering Department, METU _____

Assist. Prof. Dr. Özgür Uğraş Baran
Mechanical Engineering Department, METU _____

Assoc. Prof. Dr. Mehmet Metin Yavuz
Mechanical Engineering Department, METU _____

Assoc. Prof. Dr. Cüneyt Sert
Mechanical Engineering Department, METU _____

Assist. Prof. Dr. Onur Baş
Mechanical Engineering Department, TED University _____

Date: _____

I hereby declare that all information in this document has been obtained and presented in accordance with academic rules and ethical conduct. I also declare that, as required by these rules and conduct, I have fully cited and referenced all material and results that are not original to this work.

Name, Last Name: OĞUZHAN TAŞ

Signature :

ABSTRACT

A 6DOF SIMULATION TOOL FOR AUTONOMOUS UNDERWATER VEHICLES WITH A NOVEL METHOD FOR ADDED MASS-INERTIA CALCULATION

TAŞ, OĞUZHAN
M.S., Department of Mechanical Engineering
Supervisor : Assist. Prof. Dr. Özgür Uğraş Baran

September 2018, 112 pages

Autonomouus Underwater Vehicles, AUVs becomes popular with the development of related technologies. An high quality six degrees of motion simulation (6DOF) is a necessary tool for trajectory predictions at the design phase and also autopilot development. 6DOF simulation software for an AUV requires a detailed database of static and dynamic hydrodynamic coefficients of the vehicle in different operational conditions similar to an aircraft simulation. For a underwater vehicle simulation, additionally the added mass/inertia parameters of the vehicle is also required. Calculation of added mass/inertia values have always been challenging task for the developers. Several theoretical, experimental and numerical methods are generated for the calculation of added mass/inertia values. In this study, a 6DOF motion simulation tool is generated in MATLAB Simulink environment. The calculations of parameters necessary for the simulation are generated. Then, a novel refined numerical method for the calculation of added mass/inertia is proposed in this study. The generated 6DOF simulation tool is executed with the CFD based hydrodynamic data

and added mass/inertia values calculated by the proposed method. The verification of the proposed method and the simulation tool are carried out by comparing the results with the experimentally determined added mass values of simple shapes and the experimentally obtained trajectory data of Remus AUV.

Keywords: Hydrodynamics, 6DOF, Autonomous Underwater Vehicle, Added Mass, CFD, Remus

ÖZ

OTONOM SU ALTI ARAÇLARI İÇİN ÖZGÜN EK SU KÜTLESİ VE ATALETİ HESAPLAMA YÖNTEMİ KULLANILARAK GELİŞTİRİLMİŞ 6SER BENZETİM ARACI

TAŞ, OĞUZHAN
Yüksek Lisans, Makina Mühendisliği Bölümü
Tez Yöneticisi : Dr. Öğr. Üyesi Özgür Uğraş Baran

Eylül 2018 , 112 sayfa

Otonom su altı araçlarının tasarlanması ve geliştirilmesi konusunda, aracın yörünge tayinini yapabilme kabiliyeti oldukça önemlidir. Yörünge tayini için en yaygın kullanılan yöntem 6 serbestlik dereceli simülasyon metodlarının kullanımıdır. Bu metodlar ile bir otonom su altı aracının yörünge tayininin yapılabilmesi için, araca ait statik ve dinamik hidrodinamik kuvvet katsayıları ile aracın ek su kütlesi/ataleti gibi değerlerinin bilinmesi gerekmektedir. Bu değerler arasında, özellikle ek su kütlesi oldukça büyük öneme sahiptir. Ek su kütlesi/ataleti değerlerinin elde edilmesi işlemi, tasarımcılar için en zorlayıcı kısımlardan biridir. Araştırmacılar tarafından bu konuda bir çok teorik, deneysel ve numerik yöntem geliştirilmiştir. Bu çalışma kapsamında bir 6 serbestlik dereceli simülasyon aracı MATLAB Simulink ortamında geliştirilmiştir. Geliştirilen bu araçta kulanılmak üzere statik ve dinamik hidrodinamik katsatıların yanısıra ek su kütlesi ve ataleti değerleri de elde edilmiştir. Çalışmanın en önemli kısmı, ek su kütlesi ve ataletinin hesaplanmasında kullanılmak üzere, numerik temelli yeni bir yöntem geliştirilmesi olmuştur. Geliştirilen simülasyon aracı ve ek su kütlesi

hesaplamalarında kullanılan yöntemlerin doğrulaması amacıyla, literatürde deneysel verileri bulunan basit şekiller ile, Remus otonom su altı aracının deneysel yolla elde edilmiş yörünge bilgileri ile karşılaştırmalar yapılmıştır.

Anahtar Kelimeler: Hidrodinamik, Ek Su Kütlesi, HAD, Flowvision, Remus

To my family

ACKNOWLEDGMENTS

I would like to thank my supervisor Dr Özgür Uğraş Baran for his constant support, guidance and friendship. It was a great honor to work with him and benefiting from his invaluable comments, experiences and his endless patience throughout my study. Our cooperation influenced my academical and world view highly. I also would like to thank my former supervisor Professor Mehmet Haluk Aksel for his patient support and guidance from the very begining of my study

My family also provided invaluable support for this work. I would like to thank specially to my wife Zeynep TAŞ. She always make me feel loved and cared. I am also thankful for all the love and support by my father Seyfettin, my mother Fatma and my sisters Şule and Hilal. They have always encouraged me to this work. Without their help and support, this work would never be completed.

A lot of people influenced and supported this work scientifically and their contribution were very valuable for me. My former collegues Nabi Vefa Yavuztürk, Hüseyin Deniz Karaca, Özgün Savaş and Umut Can Küçük has always supported and encouraged me.

I would also like to express my thanks to my dearest friends for their supports

TABLE OF CONTENTS

LIST OF TABLES

LIST OF FIGURES

LIST OF SYMBOLS

α Angle of attack

β Angle of sideslip

ω_n Natural frequency of vibration

ϕ Roll orientation of the body with respect to ICS

ψ Yaw orientation of the body with respect to ICS

ρ Density

θ Pitch orientation of the body with respect to ICS

6DOF 6 Degree of freedom

AUV Autonomous Underwater Vehicle

B Rolling moment coefficient derivative with roll rate

BCS Body Coordinate System

CB Center of buoyancy

CG Center of gravity

C_l Rolling moment coefficient

C_{l_p} Rolling moment coefficient derivative with roll rate

C_{l_r} Rolling moment coefficient derivative with yaw rate

C_m Pitching moment coefficient

C_{m_α} Pitching moment coefficient with angle of attack rate

C_{m_q} Pitching moment coefficient with pitch rate

C_n Yawing moment coefficient

C_{n_p} Yawing moment coefficient derivative with roll rate

C_{n_r} Yawing moment coefficient derivative with yaw rate

C_x Static force coefficient in x direction

C_{x_q} Axial force coefficient derivative with pitch rate

C_y Static force coefficient in y direction

C_{y_p} Lateral force coefficient derivative with roll rate

C_{y_r} Lateral force coefficient derivative with yaw rate

C_z Static force coefficient in z direction

C_{z_q} Normal force coefficient derivative with pitch rate

C_{z_r} Normal force coefficient derivative with yaw rate

e_i Initial excitation of the system

ICS Inertial Coordinate System

K Total moment in x direction

$K_{\dot{p}}$ Added inertia in roll direction due to roll acceleration

$K_{\dot{q}}$ Added inertia in roll direction due to pitch acceleration

$K_{\dot{r}}$ Added inertia in roll direction due to yaw acceleration

$K_{\dot{u}}$ Added inertia in roll direction due to acceleration in axial direction

$K_{\dot{v}}$ Added inertia in roll direction due to acceleration in lateral direction

$K_{\dot{w}}$ Added inertia in roll direction due to acceleration in vertical direction

m Mass of the body

M Total moment in y direction

$M_{\dot{p}}$ Added inertia in pitch direction due to roll acceleration

$M_{\dot{q}}$ Added inertia in pitch direction due to pitch acceleration

$M_{\dot{r}}$ Added inertia in pitch direction due to yaw acceleration

$M_{\dot{u}}$ Added inertia in pitch direction due to acceleration in axial direction

$M_{\dot{v}}$ Added inertia in pitch direction due to acceleration in lateral direction

$M_{\dot{w}}$ Added inertia in pitch direction due to acceleration in vertical direction

N Total moment in z direction

$N_{\dot{p}}$ Added inertia in yaw direction due to roll acceleration

$N_{\dot{q}}$ Added inertia in yaw direction due to pitch acceleration

$N_{\dot{r}}$ Added inertia in yaw direction due to yaw acceleration

$N_{\dot{u}}$ Added inertia in yaw direction due to acceleration in axial direction

$N_{\dot{v}}$ Added inertia in yaw direction due to acceleration in lateral direction

$N_{\dot{w}}$ Added inertia in yaw direction due to acceleration in vertical direction

p Roll velocity in BCS

q Pitch velocity in BCS

r Yaw velocity in BCS

T Period of oscillation

u Forward velocity in BCS

v Lateral velocity in BCS

V Total velocity

w Vertical velocity in BCS

W Weight of the vehicle

x x position of the body with respect to ICS

X_B x-axis of the BCS

X_E x-axis of the ICS

$X_{\dot{p}}$ Added mass in axial direction due to roll acceleration

$X_{\dot{q}}$ Added mass in axial direction due to pitch acceleration

$X_{\dot{r}}$ Added mass in axial direction due to yaw acceleration

$X_{\dot{u}}$ Added mass in axial direction due to acceleration in axial direction

$X_{\dot{v}}$ Rolling moment coefficient derivative with roll rate

$X_{\dot{w}}$ Added mass in axial direction due to acceleration in vertical direction

X Total force in x direction

y y position of the body with respect to ICS

Y_B y-axis of the BCS

Y_E y-axis of the ICS

$Y_{\dot{p}}$ Added mass in lateral direction due to roll acceleration

$Y_{\dot{q}}$ Added mass in lateral direction due to pitch acceleration

$Y_{\dot{r}}$ Added mass in lateral direction due to yaw acceleration

$Y_{\dot{u}}$ Added mass in lateral direction due to acceleration in axial direction

$Y_{\dot{v}}$ Added mass in lateral direction due to acceleration in lateral direction

$Y_{\dot{w}}$ Added mass in lateral direction due to acceleration in vertical direction

Y Total force in y direction

z z position of the body with respect to ICS

Z_B z-axis of the BCS

Z_E z-axis of the ICS

$Z_{\dot{p}}$ Added mass in vertical direction due to roll acceleration

$Z_{\dot{q}}$ Added mass in vertical direction due to pitch acceleration

$Z_{\dot{r}}$ Added mass in vertical direction due to yaw acceleration

$Z_{\dot{u}}$ Added mass in vertical direction due to acceleration in axial direction

$Z_{\dot{v}}$ Added mass in vertical direction due to acceleration in lateral direction

$Z_{\dot{w}}$ Added mass in vertical direction due to acceleration in vertical direction

Z Total force in z direction

CHAPTER 1

INTRODUCTION

From the beginning of the 21^{st} century, unmanned autonomous vehicles became more and more popular, thanks to the recent developments in technology. Today, autonomous unmanned vehicles has many different application areas including research and defense industry. Using autonomous unmanned vehicles not only prevents its users from risking human lives, but also makes possible to carry out operations that are impossible for humans. As an additional benefit, since they do not contain human, the sizes of these vehicles can be very small compared to man-operated versions of them. There are various types of unmanned autonomous vehicles designed and used for variable different objectives. Generally, the autonomous vehicles can be categorized for their mission environments as follows;

- Autonomous Ground Vehicles,
- Autonomous Air Vehicles,
- Autonomous Underwater Vehicles

1.1 Vehicle simulation

The design of an autonomous vehicle is strictly dependent on the environment it is used. However, one common design activity for all three autonomous vehicle categories is the development of the simulation tool and autopilot design using this design tool. In the design phase of an unmanned vehicle, one should be capable of obtaining motion simulation of the vehicle. The motion simulation methodology is the method used for calculating the state of a vehicle in different time instants by using the rela-

tion between the motion of the vehicle and the applied forces. Houpis made a general description of simulation as follows; [1]

The state of a system is a mathematical structure containing a set of n variables $x_1(t)$, $x_2(t)$, $x_3(t)$,..., $x_i(t)$,....$x_n(t)$ called the state variables, such that the initial values $x_i(t_0)$ of this set and the system inputs $u_j(t)$ are sufficient to uniquely describe the system's future response for $t \geq t_0$. There is a minimum set of state variables which is required to represent the system accurately. The m inputs, $u_1(t)$, $u_2(t)$, $u_3(t)$,...,$u_i(t)$,...,$u_n(t)$ are deterministic; i.e., they have specific values for all values of time $t \geq t_0$.

The complexity of the motion simulation is highly dependent on the vehicle type. Different models with different degrees of freedom and different levels of complexity are occupied for ground vehicles, air vehicles and underwater vehicles.

The motion simulation of ground vehicles are relatively simple due to the constraints caused by contact with the ground [2]. Generally, the vertical motion relative to the ground is very small and damped by mechanical means, which simplifies the problem to 3 degrees of freedom motion. Additionally, because of their relatively low speeds the forces due to the interaction with the surrounding fluid is generally dominated by the forces due to mechanical means. Alexander states that often simple kinematic models are enough for wheeled bodies [3].

In comparison with the ground vehicles, simulation of air vehicles is a more complex problem. The vertical component of the motion is not small this time. Additionally, aerodynamic forces acting on the body is very dominant on the motion of the air vehicle and there are no constraints analogous to contact with ground in ground vehicles [2]. However, since the density of the air is very small compared to the density of majority of the air vehicles, there is no significant effect of acceleration-related effects (i.e. added mass) and coupled terms present on air vehicles [4]. Aircraft dynamics are typically well defined, well understood and directly verifiable through visual examination during in-flight tests and wind tunnel experiments [4].

1.2 Underwater autonomous vehicle simulation requirements

In underwater vehicles case, similar to the air vehicle simulation, the motion is also unconstrained in 6 degrees of freedom. In addition to the complexities of air vehicles, several challenges appear when modeling the underwater vehicles. Due to the density of water being very close to those of underwater vehicles in general, the acceleration-related effects and buoyancy effect become very important parameters which are added to the equations of motion.

A 6DOF simulation tool requires the databases of static and hydrodynamic forces and moments as input. Therefore, the force and moments acting on the body for different flow conditions should be generated and supplied to the simulation tool.

One of the important (and the most difficult to find) parameter, making the modeling and simulation of the underwater vehicles so complex is the added mass term which is observed at accelerating submerged bodies in mediums with a fluid of high density. In some cases, the added mass and added inertia magnitudes of underwater vehicles may become even higher than the mass or inertia of the vehicle itself. Moreover, the added mass value of an underwater vehicle is different for accelerations in different directions. Therefore, for the design of an underwater vehicle it's essential to predict the added mass and inertia of the vehicle correctly.

The analytical solution of added mass is calculated by the integration of the pressure around the body along the wetted surface of the submerged body. However this analytical approach is limited to simple geometrical shapes. Since the real-world underwater vehicles have complex shapes including rudders, sensor protuberances etc., calculating exact added mass/added inertia of those by analytical methods is not possible. Therefore, lots of different methodologies for finding the approximate added mass and added inertia of complex shapes are proposed. The methods in the literature can be classified as composite methods, experimental methods and experiment-based empirical correlations. It should be noted that the methodologies in the literature, except the experimental methods still have some major simplifications about the geometries.

1.3 Literature survey

Added mass concept is introduced by Dubua in 1776. Dubua [5] has carried out an experimental study of small oscillations using a spherical pendulum. After Dubua, Green and Stokes has expressed exact formulation for added mass of a sphere [6]. From that time, many researchers studied on the methods of determination of the added mass around bodies of arbitrary shapes moving in different fluids. In 1932, Lamb has constructed a relationship between the added mass and the kinetic energy of the fluid domain [6]. The relation constructed by Lamb was later used by Imlay [7] to derive expressions of added masses of rigid bodies moving in an ideal fluid. Imlay has also stated that the potential flow theory can be a good approximation when calculating added masses in a real fluid [7]. Newman [8], has also related the added mass with the kinetic energy of the fluid. In his book, Newman calculates the added mass of sphere analytically. Additionally, Newman gives formulation of added mass for various basic 2D geometries which have been used by Prestero [9] in his PhD thesis. Prestero benefited from the strip theory for calculating the cross-flow added mass of the body. As explained by Journee [10], the strip theory is used for determining a property and/or quantity related to a three dimensional body by treating the body as a combination of two dimensional sections. Prestero used the formulation of added mass of a 2D cylinder in cross flow for the hull of the body and the formulation of cross flow added mass of a 2D cylinder with fins proposed by Blevins [11] for the section of the body with fins. The integration of the added mass for unit lengths of 2D sections along the length of the body are carried out with the formulation given by Beck [12]. The result of the integration is the cross-flow added mass of the three dimensional body. Humphereys and Watkinson [13] presented an empirical method for calculating the added mass and added inertia terms using the parameters of the body with again the help of the kinetic energy relation on Lamb [6]. They also made the comparison of analytical results with the experimental data of an operational US submersible, obtained by David Taylor Research Center for 15 parameters. The comparisons show that the percent difference with experimental data is grater than 12% for only 4 of 15 parameters. The method proposed by Humphereys and Watkinson has later been used by Arslan [14] in his master thesis. Arslan is also claiming this method to be a good approximation to the real values of added mass and

added inertia.

Apart from the analytical methods, researchers have put considerable effort on experimental methods in order to determine the added mass. Several different experimental methodologies have been proposed for experimental determination of added mass and added inertia. Gertler [15] has defined the Planar Motion Mechanism (PMM) for determining added mass values of water vehicles. In his report, the working principle, along with the detailed description of the system is explained. Palmer [16] showed the relation between the impulse-response of the oscillating bodies and the added masses of them which is proven to be an accurate experimental method of determining the added masses of submerged bodies experimentally. On the other hand, Johnson [17] is known to be the first person who conducted CMM (Coning Motion Mechanism) tests in order to obtain the rolling-related maneuvering coefficients of an underwater vehicle, which can not be determined by conducting PMM tests. On the other hand, Kimber and Scrimshow [18] has conducted Planar Motion Mechanism and RA (Rotating Arm) in order to obtain the added mass and maneuvering derivatives of Autosub AUV by using a 3/4 scaled model. The Autosub AUV can be seen in 1.3.1. More detailed information about the working principles of the experimental mechanisms are given in 3.1.1.1, 3.1.1.2 and 3.1.1.3.

Figure 1.3.1: Autosub AUV [19]

Although there are several analytical and experimental methods for determining the added mass, the time and labor consumption of experimental methods and strict limitations of analytical methods lead some researchers to seek numerical methods of cal-

culating added masses and inertiae. Additionally, as the computational power become cheaper, numerical methods of added mass calculations become feasible. Therefore, many researchers studied on the numerical methods of added mass calculation. The study of Philips et. al. [19] is a good example. In his work, Philips used unsteady RANS solutions to perform virtual simulation of the planar motion mechanism tests of the Autosub AUV. With the usage of commercial finite volume solver Ansys CFX, Philips stated that a full set of maneuvering derivatives of an axi-symmetric underwater vehicle can be obtained within 2 days with a desktop PC, which is very practical compared with the experimental methods. A similar study has also been carried out by Coe and Neu [20]. In this study, Coe and Neu have used the commercial CFD code STAR-CCM+ in order to simulate the planar motion mechanism tests of an elongated spheroid geometry in computer environment. Coe and Neu has also investigated the effects of PMM parameters like oscillation amplitude and oscillation frequency and commented on them. Can [21] has also used the "virtual PMM" method in order to obtain the added mass and added inertia. In his master thesis, Can used the commercial CFD solver Ansys Fluent and the geometry of Autosub has been used as test bed. Song [22] has put effort for calculating added mass of underwater bodies by the solution of Laplace equation using the finite volume methodology. In his work, Song used hybrid unstructured mesh generated by ICEM and the solution of Laplace equation is used to calculate the added masses of a complex shaped underwater vehicle. The method is claimed to be a very accurate and practical way for obtaining added mass values via CFD. In a very recent study of Cura-Hochbaum [23], the added mass and some other coefficients of a ship geometry is obtained by simulating the Planar Motion Mechanism in a numerical environment using RANS. In this study, Cura-Hochbaum has also conducted PMM experiments and the comparisons of the numerical findings with the experimental data show a good agreement to each other.

1.4 Objective of the Study

The objective of this study is to develop a 6DOF simulation tool for underwater vehicles like AUVs and torpedoes and define computational tools to calculate hydrodynamic parameters to be employed in this tool. Therefore, methods for obtaining the

hydrodynamic database, which is necessary for the 6DOF simulations of bodies with complex shapes are defined in this study. The most important part of this study is the definition of a refined numerical method for the calculation of added mass/added inertia of underwater bodies of complex shapes. The method presented on this study is inspired from an experimental study which relates the added mass values of the bodies with their oscillatory response to the initial excitation [11]. New method defines a CFD method to mimic the study of Palmer, who originally developed an experimental method to determine the relation between a mass added to a long cylindrical shell and its vibration characteristics [16]. Current study exploits this idea to determine hydrodynamic added mass of bodies using Blevin's ideas [11]. Selected experimental method is capable of defining added mass values only. In this thesis the experimental method is extended to calculate the added inertia values in numerical environment.

1.5 Organization of the Thesis

This thesis is composed of 5 chapters and an Appendix. Chapter 1 gives an introductory information about unmanned autonomous vehicles, the problem of added mass/inertia, encountered when developing autonomous underwater vehicles. A literature survey concerning the past studies about obtaining the added mass values is also included to this chapter. Additionally, along with a brief information about the proposed solution for obtaining the added mass and inertia values of an AUV, the aim of this thesis is given on this chapter.

Chapter 2 gives detailed information about 6DOF motion simulation methodology. The theory of 6DOF motion simulation, the coordinate systems transformation and the governing equations of motion can be found in this chapter. Additionally, the 6DOF simulation tool, generated for the calculation of trajectories of underwater vehicles is introduced. Information about the unit tests carried out in order to asses the outputs of the 6DOF simulation tool from a logical perspective is also located in this chapter. The detailed explanations about unit tests are not contained in this chapter, instead they are put in Appendix A.

Chapter 3 introduces the theory behind the added mass phenomena. Methods of added mass calculation proposed by different researchers are revised in this chapter. Additionally, a new numerical method is proposed in this chapter. The detailed explanation of the method, theory behind the method, along with the calculation procedure and application of the experimental method in a numerical environment is given in this chapter. The validation studies concerning the proposed method are also placed in this chapter.

Chapter 4 is about the validation of the studies performed in this thesis. The explanations concerning the generation of static and dynamic hydrodynamic databases and added mass values which are used in the 6DOF simulation tool are given in this chapter. The 6DOF simulation tool which uses the added mass and inertia values generated by the proposed method is validated in this chapter. Trajectory results generated by the 6DOF simulation system are compared with the experimentally obtained data found in literature.

As the last chapter, Chapter 5 concludes the study with comments on the results and recommendations for possible future studies.

CHAPTER 2

6DOF MOTION SIMULATION FOR AUVS

In this chapter, 6DOF motion simulations of AUVs will be explained. The details about theory of motion simulation and definitions of the coordinate systems will be given in this chapter. Equations of motion and the net forces and moments acting on the body will also be discussed in this section. Additionally, the information about the organization and the validation of 6DOF simulation tool which is developed for this study will be given.

2.1 Theory of 6DOF motion simulation

The motion simulation can be defined as the calculating of the state of a vehicle at an instance by relating the state variables of previous instance with the rates of change of state variables. In other words, motion simulation is the integration of the rate of changes of state variables over discrete time steps to get the motion of the model. The state of a vehicle is represented by a column vector $\overrightarrow{S}$.

$$\overrightarrow{S} = \begin{bmatrix} u & v & w & p & q & r & x & y & z & \phi & \theta & \psi \end{bmatrix}^T \tag{2.1.1}$$

where u, v, w, p, q, and r are the linear and angular velocities expressed in the BCS and x, y, z, ϕ, θ and ψ are the linear and angular positions of the body expressed in ICS. Note that the rates of change of the last 6 components of the state vector can be calculated by using the first 6 components and their rates. Therefore, the solution of equations of motion involves calculating the rate of changes of the first 6 components of the state vector.

In order to understand 6DOF motion simulation and the rigid body equations of mo-

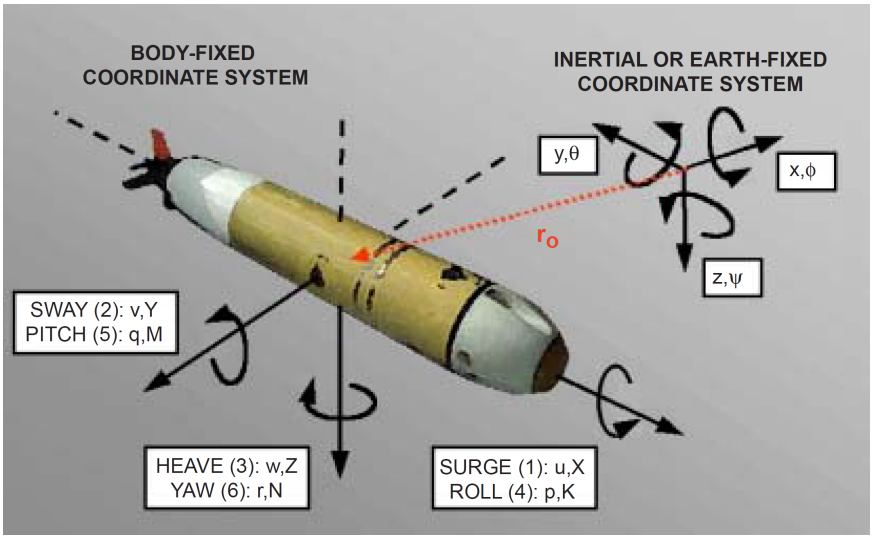

Figure 2.1.1: The body coordinate system and the earth coordinate system[9]

tion, coordinate systems used in these equations and the transformation between them should be given. Therefore, information about the coordinate systems and coordinate system transformation will be given firstly.

2.1.1 Inertial and body coordinate systems

Two coordinate systems to be used in this study are, namely; the Body Coordinate System and the Earth Coordinate System i.e. Inertial Coordinate System as they are shown in Figure 2.1.1. The inertial coordinate system is fixed to earth, so it does not move or rotate with vehicle motion. On the other hand, the body coordinate system is fixed to the body and it translates and rotates with respect to the inertial coordinate system as the body translates or rotates. In other words, the motion of the body coordinate system with respect to earth coordinate system gives the motion of the body in earth coordinate system. The forces and moments acting on the body are defined in the body coordinate system while the motion of the body should be defined in the inertial coordinate system. Therefore, the rates of the state vector should undergo coordinate system transformation in order to obtain the motion of the body. The coordinate system transformation is carried out by transformation matrices. Derivation of the coordinate transformation matrices and the coordinate transformation operation are explained in the following subsections.

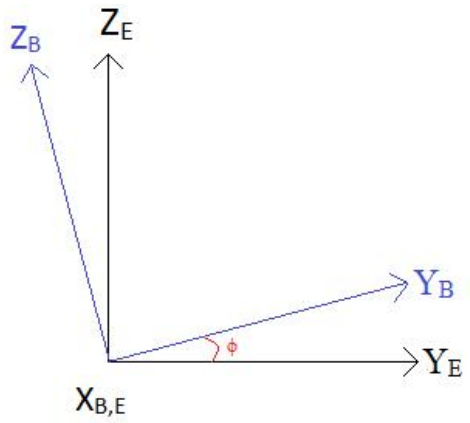

Figure 2.1.2: Simple rotation of YZ plane about x-axis

2.1.1.1 Coordinate transformation

In this part, the procedure of coordinate transformation and the derivation of coordinate transform matrix is explained. Two coordinate transform matrices are defined: first one, $J_1(\eta_2)$, relates linear velocities between body fixed and earth fixed coordinate system, where the other one, $J_2(\eta_2)$ relates the angular (or rotational) velocities.

$J_1(\eta_2)$ is composed of three rotation matrices, which are function of; rotation about x-axis (ϕ), rotation about y-axis (θ) and rotation about z-axis (ψ). These three rotations are also named as Roll, Pitch and Yaw, respectively. In Figure 2.1.2, schematic representation of a simple (single axis) rotation, namely; rotation of YZ plane along x-axis is shown.

Note that the rotation about the x-axis of the body does not change the orientation of body x-axis with respect to inertial axis.

Then, following relationships are obtained;

$$X_E = X_B \tag{2.1.2}$$

$$Y_E = Y_B \cos(\phi) - Z_B \sin(\phi) \tag{2.1.3}$$

$$Z_E = Y_B \sin(\phi) + Z_B \cos(\phi) \tag{2.1.4}$$

or in matrix form;

$$\begin{bmatrix} X_E \\ Y_E \\ Z_E \end{bmatrix} = \begin{bmatrix} 1 & 0 & 0 \\ 0 & \cos(\phi) & -\sin(\phi) \\ 0 & \sin(\phi) & \cos(\phi) \end{bmatrix} \begin{bmatrix} X_B \\ Y_B \\ Z_B \end{bmatrix} \tag{2.1.5}$$

Rewriting Equation (2.1.5)we get;

$$\begin{bmatrix} X_E \\ Y_E \\ Z_E \end{bmatrix} = R(\phi) \begin{bmatrix} X_B \\ Y_B \\ Z_B \end{bmatrix} \tag{2.1.6}$$

Transformation matrices for rotations about y and z axes can also be found by applying the same procedure;

$$R(\theta) = \begin{bmatrix} \cos\theta & 0 & \sin\theta \\ 0 & 1 & 0 \\ -\sin\theta & 0 & \cos\theta \end{bmatrix} \tag{2.1.7}$$

$$R(\psi) = \begin{bmatrix} \cos\psi & -\sin\psi & 0 \\ \sin\psi & \cos\psi & 0 \\ 0 & 0 & 1 \end{bmatrix} \tag{2.1.8}$$

and the multiplication of these three transformation matrices give $J_1(\eta_2)$ as written below ;

$$J_1(\eta_2) = R(\psi)R(\theta)R(\phi) \tag{2.1.9}$$

$$J_1(\eta_2) = \begin{bmatrix} \cos\psi\cos\theta & \cos\psi\sin\theta\sin\phi - \sin\psi\cos\phi & \sin\psi\sin\phi + \cos\phi\cos\psi\sin\theta \\ \sin\psi\cos\theta & \cos\psi\cos\phi + \sin\psi\sin\theta\sin\phi & \cos\phi\sin\psi\sin\theta - \cos\psi\sin\phi \\ -\sin\theta & \cos\theta\sin\phi & \cos\theta\cos\phi \end{bmatrix} \tag{2.1.10}$$

While deriving the coordinate transformation matrices, one should always be aware of the fact that the sequence of the rotations are important. In other words, different sequence of rotations result different coordinate transformation matrices. Another remark about $J_1(\eta_2)$ is its orthogonality, which means;

$$J_1(\eta_2)^{-1} = J_1(\eta_2)^T \tag{2.1.11}$$

The second coordinate transform $J_2(\eta_2)$ relates the rotational velocities between the body axis and the earth axis, in other words, $J_2(\eta_2)$ relates the rate of change of Euler angles with the angular velocities defined in body axis.

As can be understood from the calculation of $J_1(\eta_2)$, the sequences of rotations used in this study is the roll-pitch-yaw order. That means, a vector in body coordinate system is transformed into the earth coordinate system by applications of first roll, then pitch and the last yaw transformations. Since the last transformation applied is the yaw angle transformation, the rate of change of yaw angle of the body coordinate system relative to the inertial coordinate system does not need to be transformed. While the roll angular rate is transformed due to pitch and yaw angles and the pitch angular rate is transformed due to yaw angle.

$$\begin{bmatrix} p \\ q \\ r \end{bmatrix} = \begin{Bmatrix} 0 \\ 0 \\ \dot{\psi} \end{Bmatrix} + R(\psi) \begin{Bmatrix} 0 \\ \dot{\theta} \\ 0 \end{Bmatrix} + R(\psi)R(\theta) \begin{Bmatrix} \dot{\phi} \\ 0 \\ 0 \end{Bmatrix} \tag{2.1.12}$$

As a result, the transformation matrix takes the following form

$$J_2(\eta_2) = \begin{bmatrix} 1 & 0 & -\sin\theta \\ 0 & \cos\phi & \sin\phi\cos\theta \\ 0 & -\sin\phi & \cos\phi\cos\theta \end{bmatrix} \tag{2.1.13}$$

taking the inverse gives,

$$\begin{bmatrix} \dot{\phi} \\ \dot{\theta} \\ \dot{\psi} \end{bmatrix} = \begin{bmatrix} 1 & \sin\phi tan\theta & \cos\phi tan\theta \\ 0 & \cos\phi & -\sin\phi \\ 0 & \sin\phi/\cos\theta & \cos\phi/\cos\theta \end{bmatrix} \begin{bmatrix} p \\ q \\ r \end{bmatrix} \tag{2.1.14}$$

which concludes

$$J_2(\eta_2) = \begin{bmatrix} 1 & sin\phi tan\theta & cos\phi tan\theta \\ 0 & cos\phi & -sin\phi \\ 0 & sin\phi/cos\theta & cos\phi/cos\theta \end{bmatrix} \tag{2.1.15}$$

Note that the $J_2(\eta_2)$ matrix is singular for pitch angle $\pm 90^o$ due to the cosine term in the denominator of the elements of third raw. However, it does not pose to be a problem for AUV case, because the Autonomous Underwater Vehicles does not ordinarily reach the pitch angles of 90^0.

2.1.2 Equations of motion

As stated previously, equations of motion relates the net forces and moments on the body with the movement of the body. In this part, equations of motion in six degree of freedom will be discussed. First, equations of motion which relates the forces with the motion of the body is explained, then equations relating the moments and the motion of the body.

In the simplest form, according to Newton's second law, the force acting on the body cause the rate of change of linear momentum. It can be written as;

$$\overrightarrow{F} = \frac{d(m\overrightarrow{V})}{dt} \tag{2.1.16}$$

However, Equation (2.1.16) is only valid for $\overrightarrow{F}$ and $\overrightarrow{V}$ defined in an inertial coordinate system. However, in our case these two vectors are defined in body coordinates. For our case, Newton's second law can be rewritten as;

$$\overrightarrow{F} = m\left(\frac{d\overrightarrow{V}}{dt} + \overrightarrow{\omega} \times \overrightarrow{V}\right) \tag{2.1.17}$$

In open form;

$$\begin{bmatrix} X \\ Y \\ Z \end{bmatrix} = m \begin{bmatrix} \dot{u} \\ \dot{v} \\ \dot{w} \end{bmatrix} + \begin{bmatrix} p \\ q \\ r \end{bmatrix} \times \begin{bmatrix} u \\ v \\ w \end{bmatrix} \tag{2.1.18}$$

After the summations and operation of vector product, Equation (2.1.18) takes the following form;

$$\begin{bmatrix} X \\ Y \\ Z \end{bmatrix} = m \begin{bmatrix} \dot{u} + wq - vr \\ \dot{v} + ur - wp \\ w + v\dot{p} - uq \end{bmatrix} \tag{2.1.19}$$

Just like the force equation, moments are also related to the rate of change of angular momentum of the body. Since the moments are also defined in the body coordinate system, Newton's second law will be written as;

$$\overrightarrow{M} = \frac{d(I\overrightarrow{\omega})}{dt} + \overrightarrow{\omega} \times I\overrightarrow{\omega} \tag{2.1.20}$$

$$
\begin{aligned}
\begin{bmatrix} K \\ M \\ N \end{bmatrix} &= \begin{bmatrix} I_{xx} & -I_{xy} & -I_{xz} \\ -I_{yx} & I_{yy} & -I_{yz} \\ -I_{zx} & -I_{zy} & I_{zz} \end{bmatrix} \begin{bmatrix} \dot{p} \\ \dot{q} \\ \dot{r} \end{bmatrix} + \begin{bmatrix} p \\ q \\ r \end{bmatrix} \times \begin{bmatrix} I_{xx} & -I_{xy} & -I_{xz} \\ -I_{yx} & I_{yy} & -I_{yz} \\ -I_{zx} & -I_{zy} & I_{zz} \end{bmatrix} \begin{bmatrix} p \\ q \\ r \end{bmatrix} \\
&= \begin{bmatrix} I_{xx}\dot{p} - I_{xy}\dot{q} - I_{xz}\dot{r} \\ I_{yy}\dot{q} - I_{yx}\dot{p} - I_{yz}\dot{r} \\ I_{zz}\dot{r} - I_{zx}\dot{p} - I_{zy}\dot{q} \end{bmatrix} + \begin{bmatrix} p \\ q \\ r \end{bmatrix} \times \begin{bmatrix} I_{xx}p - I_{xy}q - I_{xz}r \\ I_{yy}q - I_{yx}p - I_{yz}r \\ I_{zz}r - I_{zx}p - I_{zy}q \end{bmatrix} \qquad (2.1.21) \\
&= \begin{bmatrix} I_{xx}\dot{p} + (I_{zz} - I_{yy})qr - (\dot{r} + pq)I_{xz} + (r^2 - q^2)I_{yz} + (pr - \dot{q})I_{xy} \\ I_{yy}\dot{q} + (I_{xx} - I_{zz})rp - (\dot{p} + qr)I_{xy} + (p^2 - r^2)I_{xz} + (qp - \dot{r})I_{yz} \\ I_{zz}\dot{r} + (I_{yy} - I_{xx})pq - (\dot{q} + rp)I_{yz} + (q^2 - p^2)I_{xy} + (rq - \dot{p})I_{xz} \end{bmatrix}
\end{aligned}
$$

Note that the off-diagonal elements of the inertia matrix are products of inertia which emerge due to the imbalances in the mass distribution of the body. When the shapes and mass properties of AUVs are considered, the mass imbalances are not very significant, which makes the product of inertia terms negligibly small or zero. For such a case, Equation (2.1.21) can be simplified to the following.

$$
\begin{bmatrix} K \\ M \\ N \end{bmatrix} = \begin{bmatrix} I_{xx}\dot{p} + (I_{zz} - I_{yy})qr \\ I_{yy}\dot{q} + (I_{xx} - I_{zz})rp \\ I_{zz}\dot{r} + (I_{yy} - I_{xx})pq \end{bmatrix} \qquad (2.1.22)
$$

At the end, by combining Equation (2.1.18) and Equation (2.1.22) we get the equations of motion in 6 degrees of freedom as shown in the following equation.

$$
\begin{bmatrix} X \\ Y \\ Z \\ K \\ M \\ N \end{bmatrix} = \begin{bmatrix} m(\dot{u} + wq - vr) \\ m(\dot{v} + ur - wp) \\ m(w + vp - uq) \\ I_{xx}\dot{p} + (I_{zz} - I_{yy})qr \\ I_{yy}\dot{q} + (I_{xx} - I_{zz})rp \\ I_{zz}\dot{r} + (I_{yy} - I_{xx})pq \end{bmatrix} \qquad (2.1.23)
$$

One should be aware of the fact that; all these equations relating the forces and moments to the motion of the body are written under the assumption of the origin of the body coordinate system is located at the center of gravity (CG) of the vehicle. When dealing with aerodynamics, this assumption is almost always satisfied. However, in underwater applications, since the hydrostatic forces are very effective on the motion of the body, the origin of the body coordinate system is generally located at the center of buoyancy (CB) of the vehicle. Therefore, the equations of motion are revised by the following procedure;

$\overrightarrow{r_g} = \begin{bmatrix} x_g & y_g & z_g \end{bmatrix}^T$ being the position vector of CG with respect to CB (i.e. the origin of the body coordinate system), Equation (2.1.23) takes the following form;

$$\begin{bmatrix} X \\ Y \\ Z \\ K \\ M \\ N \end{bmatrix} = \begin{bmatrix} m\{\dot{u} + wq - vr - x_g(q^2 + r^2) + y_g(pq - \dot{r}) + z_g(pr + \dot{q})\} \\ m\{\dot{v} + ur - wp - y_g(r^2 + p^2) + z_g(qr - \dot{p}) + x_g(qp + \dot{r})\} \\ m\{w + vp - uq - z_g(p^2 + q^2) + x_g(rp - \dot{q}) + y_g(rq + \dot{p})\} \\ I_{xx}\dot{p} + (I_{zz} - I_{yy})qr + m\{y_g(\dot{w} - uq + vp) - z_g(\dot{v} - wp + ur)\} \\ I_{yy}\dot{q} + (I_{xx} - I_{zz})rp + m\{z_g(\dot{u} - vr + wq) - x_g(\dot{w} - uq + vp)\} \\ I_{zz}\dot{r} + (I_{yy} - I_{xx})pq + m\{x_g(\dot{v} - wp + ur) - y_g(\dot{u} - vr + wq)\} \end{bmatrix} \tag{2.1.24}$$

Note that the left-hand sides of Equation (2.1.23) and Equation (2.1.24), represent the total net forces and moments acting on the body. The net force and moment on the body are composed of the the hydrostatic forces and hydrodynamic forces. The detailed explanation of the forces acting on the body and the methods used to calculate the forces will be discussed in the following section.

2.1.3 Forces acting on a submerged body

This section deals with the forces and moments acting on an underwater vehicle in detail. The forces/moments can be divided into four sub-categories;

- Hydrostatic Forces (Forces due to weight & buoyancy)
- Static Hydrodynamic Forces

- Hydrodynamic Damping Effects

- Forces due to Added Mass

2.1.3.1 Hydrostatic forces

Hydrostatic forces emerges as a result of weight and buoyancy of the vehicle, since the weight and buoyancy forces are always in the opposite directions. Keeping in mind that the positive z axis shown in Figure 2.1.1 is toward downwards, one can write the following.

$$\overrightarrow{F_{HS}} = \overrightarrow{f_G} - \overrightarrow{f_B} \tag{2.1.25}$$

It is important to note that the weight and buoyancy are defined in earth-fixed coordinate system, to express these in body coordinates, transformation applies as following;

$$\overrightarrow{f_G}(\eta_2) = J^{-1} \begin{bmatrix} 0 \\ 0 \\ W \end{bmatrix} \tag{2.1.26}$$

and

$$\overrightarrow{f_B}(\eta_2) = J^{-1} \begin{bmatrix} 0 \\ 0 \\ B \end{bmatrix} \tag{2.1.27}$$

At the end of the transformation to body axis, the weight and buoyancy force vectors

takes the following form.

$$\overrightarrow{f_G} = \begin{bmatrix} W\,(-sin\theta) \\ W\,(cos\theta sin\phi) \\ W\,(cos\theta cos\phi) \end{bmatrix}$$
$$\overrightarrow{f_B} = \begin{bmatrix} B\,(-sin\theta) \\ B\,(cos\theta sin\phi) \\ B\,(cos\theta cos\phi) \end{bmatrix} \tag{2.1.28}$$

Then equation Equation (2.1.25) takes its final form;

$$\overrightarrow{F_{HS}} = \begin{bmatrix} X_{HS} \\ Y_{HS} \\ Z_{HS} \end{bmatrix} = (W - B) \begin{bmatrix} -sin\theta \\ cos\theta sin\phi \\ cos\theta cos\phi \end{bmatrix} \tag{2.1.29}$$

Hydrostatic moments are also calculated using similar methodologies, the only difference is that the cross product of the position vectors of the CG and CB with the weight and buoyancy forces are calculated.

$$\overrightarrow{M_{HS}} = \overrightarrow{r_G} \times \overrightarrow{f_G} - \overrightarrow{r_B} \times \overrightarrow{f_B} \tag{2.1.30}$$

where

$$\overrightarrow{r_G} = \begin{bmatrix} x_g & y_g & z_g \end{bmatrix}^T \tag{2.1.31}$$

and

$$\overrightarrow{r_B} = \begin{bmatrix} x_b & y_b & z_b \end{bmatrix}^T \tag{2.1.32}$$

$$\overrightarrow{r_G} \times \overrightarrow{f_G} = \begin{bmatrix} x_g \\ y_g \\ z_g \end{bmatrix} \times \begin{bmatrix} W\left(-sin\theta\right) \\ W\left(cos\theta sin\phi\right) \\ W\left(cos\theta cos\phi\right) \end{bmatrix} = W \begin{bmatrix} y_g\left(cos\theta cos\phi\right) - z_g\left(cos\theta sin\phi\right) \\ -x_g\left(cos\theta cos\phi\right) - z_g sin\theta \\ x_g\left(cos\theta sin\phi\right) + y_g sin\theta \end{bmatrix} \tag{2.1.33}$$

and

$$\overrightarrow{r_B} \times \overrightarrow{f_B} = \begin{bmatrix} x_b \\ y_b \\ z_b \end{bmatrix} \times \begin{bmatrix} B\left(-sin\theta\right) \\ B\left(cos\theta sin\phi\right) \\ B\left(cos\theta cos\phi\right) \end{bmatrix} = B \begin{bmatrix} y_b\left(cos\theta cos\phi\right) - z_b\left(cos\theta sin\phi\right) \\ -x_b\left(cos\theta cos\phi\right) - z_b sin\theta \\ x_b\left(cos\theta sin\phi\right) + y_b sin\theta \end{bmatrix} \tag{2.1.34}$$

at the end, equation Equation (2.1.30) takes the following form;

$$\overrightarrow{M_{HS}} = \begin{bmatrix} (y_g W - y_b B)cos\theta cos\phi - (z_g W - z_b B)cos\theta sin\phi \\ -\left(x_g W - x_b B\right)cos\theta cos\phi - \left(z_g W - z_b B\right)sin\theta \\ \left(x_g W - x_b B\right)cos\theta sin\phi + \left(y_g W - y_b B\right)sin\theta \end{bmatrix} \tag{2.1.35}$$

2.1.3.2 Static hydrodynamic forces

The static hydrodynamic forces are the static forces which occur as a result of the pressure distribution around the body and the viscous friction due to the motion in the fluid. Generally, these forces are expressed as non-dimensional force/moment coefficients. The non-dimensionalization is shown in the following equation where ξ represents any force, ζ represents any moment, Q is the dynamic pressure, S_{ref} and L_{ref} are the reference area and length, respectively.

$$C_\xi = \xi/(Q * S_{ref}) \qquad and\ C_\zeta = \zeta/(Q * S_{ref} * L_{ref}) \tag{2.1.36}$$

The formulae associated with S_{ref}, L_{ref} and Q are given in the following;

$$\begin{aligned} L_{ref} &= D \\ S_{ref} &= \tfrac{1}{4}\pi D^2 \\ Q &= \tfrac{1}{2}\rho V^2 \end{aligned} \tag{2.1.37}$$

In Equation (2.1.37), ρ is the fluid density while V is the total velocity (magnitude of the velocity of the body relative to fluid) and D is the maximum diameter of the hull cross-section of the body. The necessary static hydrodynamic force and moment coefficients, which are defined in the body axis are namely; the axial force coefficient (C_x) and rolling moment coefficient (C_l) defined in x-axis, lateral force coefficient (C_y) and pitching moment coefficient (C_m) defined in y-axis, and normal force coefficient (C_z) yawing moment coefficient (C_n) defined in z-axis, . There are several methods of calculating the static hydrodynamic force and moment coefficients. Each method requires different level of labor and computational effort and also provide different levels of accuracy. These methods are:

- Analytical/Empirical Methods
- Numerical Methods
- Experimental Methods

It's a known fact that the analytical methods lack accuracy and limited by simplifications on the model geometry. On the other hand, experimental methods not only require a proper setup and test facilities that may not be available to developer but also significant financial resources. Therefore, in this study, the static hydrodynamic forces are decided to be obtained by numerical methods. For the numerical derivation of static hydrodynamic forces, Fluent commercial CFD code is used. The details and parameters about the generation of static hydrodynamic database is given in the proceeding chapters.

2.1.3.3 Hydrodynamic damping effects

Hydrodynamic damping effects emerge due to the viscous dissipation observed at unsteady motion of the submerged body in the fluid and generally referred as dy-

namic derivatives. Unlike the static hydrodynamic forces, damping derivatives observed in dynamic conditions, in other words hydrodynamic damping effect become present when the rotation rates of the vehicle are non-zero . Dynamic derivatives of the vehicles are generally represented as non-dimensional coefficients. The non-dimensionalization of the dynamic derivatives are carried out by using the rotation rate of the vehicle in the corresponding direction and total velocity of the vehicle. As an example, non-dimensionalization of pitching moment coefficient derivative with pitch rate is shown in the following equation.

$$C_{M_q} = \partial C_m / \partial \left(q L_{ref} / 2 / V \right) \tag{2.1.38}$$

The dynamic derivatives are obtained using the Missile DATCOM semi-empirical tool in this study.

2.1.3.4 Forces due to added mass

As stated before, the forces due to added mass are occurring proportional to the acceleration of the vehicle in that direction, therefore these effects are treated as mass. Since they are treated as mass, they are included into the mass matrix of the 6DOF equations of motion rather than the forces side.

2.1.3.5 Combination

After having an understanding of the theory of added mass and 6DOF motion simulation, the calculation of the forces and moments acting on the body can be performed. The total forces and moments acting on the body can be found by the summation of the static hydrodynamic forces, dynamic hydrodynamic forces and forces due to added mass. For example, the total force calculation on the x-axis is done by the following equations.

$$X = X_{static} + X_{dynamic} + X_{added\,mass} \tag{2.1.39}$$

$$X_{static} = C_x Q S_{ref} \tag{2.1.40}$$

$$X_{dynamic} = C_{x_q} \left(qL_{ref}/2/V\right) \left(QS_{ref}\right) \tag{2.1.41}$$

and

$$X_{added\,mass} = X_{\dot{u}}\dot{u} + X_{\dot{v}}\dot{v} + X_{\dot{w}}\dot{w} + X_{\dot{p}}\dot{p} + X_{\dot{q}}\dot{q} + X_{\dot{r}}\dot{r} \tag{2.1.42}$$

Note that in Equation (2.1.41), the term C_{x_q} is the damping coefficient along x-axis due to the rotation rate in pitch direction. The total moments acting on the body can be found by the following equations;

$$K = K_{static} + K_{dynamic} + K_{addedmass} \tag{2.1.43}$$

$$K_{static} = C_l Q S_{ref} Lref \tag{2.1.44}$$

$$K_{dynamic} = \left(C_{l_p} p + C_{l_p} r\right) \left(L_{ref}/2/V\right) Q S_{ref} L_{ref} \tag{2.1.45}$$

$$K_{addedmass} = K_{\dot{u}}\dot{u} + K_{\dot{v}}\dot{v} + K_{\dot{w}}\dot{w} + K_{\dot{p}}\dot{p} + K_{\dot{q}}\dot{q} + K_{\dot{r}}\dot{r} \tag{2.1.46}$$

Applying the same procedure to forces and moments along the y and z axes, all forces and moments along x, y and z axes are calculated as shown in the following equation.

$$
\begin{aligned}
X &= \left\{C_x + C_{x_q}\left(qL_{ref}/2/V\right)\right\}\left(QS_{ref}\right) \\
&\quad + X_{\dot{u}}\dot{u} + X_{\dot{v}}\dot{v} + X_{\dot{w}}\dot{w} + X_{\dot{p}}\dot{p} + X_{\dot{q}}\dot{q} + X_{\dot{r}}\dot{r} \\
Y &= \left\{C_y + \left(C_{y_r}r + C_{y_p}p\right)\left(L_{ref}/2/V\right)\right\}\left(QS_{ref}\right) \\
&\quad + Y_{\dot{u}}\dot{u} + Y_{\dot{v}}\dot{v} + Y_{\dot{w}}\dot{w} + Y_{\dot{p}}\dot{p} + Y_{\dot{q}}\dot{q} + Y_{\dot{r}}\dot{r} \\
Z &= \left\{C_z + \left(C_{z_q}q + C_{z_r}r\right)\left(L_{ref}/2/V\right)\right\}\left(QS_{ref}\right) \\
&\quad + Z_{\dot{u}}\dot{u} + Z_{\dot{v}}\dot{v} + Z_{\dot{w}}\dot{w} + Z_{\dot{p}}\dot{p} + Z_{\dot{q}}\dot{q} + Z_{\dot{r}}\dot{r} \\
K &= \left\{C_l + \left(C_{l_p}p + C_{l_r}r\right)\left(L_{ref}/2/V\right)\right\}\left(QS_{ref}L_{ref}\right) \\
&\quad + K_{\dot{u}}\dot{u} + K_{\dot{v}}\dot{v} + K_{\dot{w}}\dot{w} + K_{\dot{p}}\dot{p} + K_{\dot{q}}\dot{q} + K_{\dot{r}}\dot{r} \\
M &= \left\{C_m + \left(C_{m_q}q + C_{m_\alpha}\alpha\right)\left(L_{ref}/2/V\right)\right\}\left(QS_{ref}L_{ref}\right) \\
&\quad + M_{\dot{u}}\dot{u} + M_{\dot{v}}\dot{v} + M_{\dot{w}}\dot{w} + M_{\dot{p}}\dot{p} + M_{\dot{q}}\dot{q} + M_{\dot{r}}\dot{r} \\
N &= \left\{C_n + \left(C_{n_p}p + C_{n_r}r\right)\left(L_{ref}/2/V\right)\right\}\left(QS_{ref}L_{ref}\right) \\
&\quad + N_{\dot{u}}\dot{u} + N_{\dot{v}}\dot{v} + N_{\dot{w}}\dot{w} + N_{\dot{p}}\dot{p} + N_{\dot{q}}\dot{q} + N_{\dot{r}}\dot{r}
\end{aligned}
\tag{2.1.47}
$$

Note that Equation (2.1.47) contain the forces and moments due to all 36 components added mass, however, in the case of underwater vehicle applications, many of these 36 terms will be zero due to the symmetry of the vehicle in horizontal, vertical or lateral planes.

2.2 6DOF simulation tool

Since the theory of motion simulation is based on the calculation of rates of change of state variables, Equation (2.1.24) and Equation (2.1.47) are written in the open form, then rearranged accordingly. Combining Equation (2.1.24) and Equation (2.1.47) and rewriting in open form we get:

$$
\begin{aligned}
m\left\{\dot{u}+wq-vr-x_g(q^2+r^2)+y_g(pq-\dot{r})+z_g(pr+\dot{q})\right\} &= \\
\left\{C_x+C_{x_q}\left(qL_{ref}/2/V\right)\right\}\left(QS_{ref}\right) & \\
+X_{\dot{u}}\dot{u}+X_{\dot{v}}\dot{v}+X_{\dot{w}}\dot{w}+X_{\dot{p}}\dot{p}+X_{\dot{q}}\dot{q}+X_{\dot{r}}\dot{r} &
\end{aligned}
$$

$$
\begin{aligned}
m\left\{\dot{v}+ur-wp-y_g(r^2+p^2)+z_g(qr-\dot{p})+x_g(qp+\dot{r})\right\} &= \\
\left\{C_y+\left(C_{y_r}r+C_{y_p}p\right)\left(L_{ref}/2/V\right)\right\}\left(Q*S_{ref}\right) & \\
+Y_{\dot{u}}\dot{u}+Y_{\dot{v}}\dot{v}+Y_{\dot{w}}\dot{w}+Y_{\dot{p}}\dot{p}+Y_{\dot{q}}\dot{q}+Y_{\dot{r}}\dot{r} &
\end{aligned}
$$

$$
\begin{aligned}
m\left\{w+vp-uq-z_g(p^2+q^2)+x_g(rp-\dot{q})+y_g(rq+\dot{p})\right\} &= \\
\left\{C_z+\left(C_{z_q}q+C_{z_r}r\right)\left(L_{ref}/2/V\right)\right\}\left(Q*S_{ref}\right) & \\
+Z_{\dot{u}}\dot{u}+Z_{\dot{v}}\dot{v}+Z_{\dot{w}}\dot{w}+Z_{\dot{p}}\dot{p}+Z_{\dot{q}}\dot{q}+Z_{\dot{r}}\dot{r} &
\end{aligned}
$$

(2.2.1)

$$
\begin{aligned}
I_{xx}\dot{p}+(I_{zz}-I_{yy})qr+m\left\{y_g\left(\dot{w}-uq+vp\right)-z_g\left(\dot{v}-wp+ur\right)\right\} &= \\
\left\{C_l+\left(C_{l_p}p+C_{l_r}r\right)\left(L_{ref}/2/V\right)\right\}\left(QS_{ref}L_{ref}\right) & \\
+K_{\dot{u}}\dot{u}+K_{\dot{v}}\dot{v}+K_{\dot{w}}\dot{w}+K_{\dot{p}}\dot{p}+K_{\dot{q}}\dot{q}+K_{\dot{r}}\dot{r} &
\end{aligned}
$$

$$
\begin{aligned}
I_{yy}\dot{q}+(I_{xx}-I_{zz})rp+m\left\{z_g\left(\dot{u}-vr+wq\right)-x_g\left(\dot{w}-uq+vp\right)\right\} &= \\
\left\{C_m+\left(C_{m_q}q+C_{m_\alpha}\alpha\right)\left(L_{ref}/2/V\right)\right\}\left(QS_{ref}L\right) & \\
+M_{\dot{u}}\dot{u}+M_{\dot{v}}\dot{v}+M_{\dot{w}}\dot{w}+M_{\dot{p}}\dot{p}+M_{\dot{q}}\dot{q}+M_{\dot{r}}\dot{r} &
\end{aligned}
$$

$$
\begin{aligned}
I_{zz}\dot{r}+(I_{yy}-I_{xx})pq+m\left\{x_g\left(\dot{v}-wp+ur\right)-y_g\left(\dot{u}-vr+wq\right)\right\} &= \\
\left\{C_n+\left(C_{n_p}p+C_{n_r}r\right)\left(L_{ref}/2/V\right)\right\}\left(QS_{ref}*L\right) & \\
+N_{\dot{u}}\dot{u}+N_{\dot{v}}\dot{v}+N_{\dot{w}}\dot{w}+N_{\dot{p}}\dot{p}+N_{\dot{q}}\dot{q}+N_{\dot{r}}\dot{r} &
\end{aligned}
$$

By rearranging Equation (2.2.1) and writing in matrix form, the final version of the 6DOF equations of motion takes the following form.

$$\begin{bmatrix} m-X_{\dot{u}} & -X_{\dot{v}} & -X_{\dot{w}} & -X_{\dot{p}} & mz_g-X_{\dot{q}} & -my_g-X_{\dot{r}} \\ -Y_{\dot{u}} & m-Y_{\dot{v}} & -Y_{\dot{w}} & mz_g-Y_{\dot{p}} & -Y_{\dot{q}} & mx_g-Y_{\dot{r}} \\ -Z_{\dot{u}} & -Z_{\dot{v}} & m-Z_{\dot{w}} & my_g-Z_{\dot{p}} & mx_g-Z_{\dot{q}} & -Z_{\dot{r}} \\ -K_{\dot{u}} & -mz_g-K_{\dot{v}} & my_g-K_{\dot{w}} & I_{xx}-K_{\dot{p}} & -K_{\dot{q}} & -K_{\dot{r}} \\ mz_g-M_{\dot{u}} & -M_{\dot{v}} & -mx_g-M_{\dot{w}} & -M_{\dot{p}} & I_{yy}-M_{\dot{q}} & -M_{\dot{r}} \\ -my_g-N_{\dot{u}} & mx_g-N_{\dot{v}} & -N_{\dot{w}} & -N_{\dot{p}} & -N_{\dot{q}} & I_{zz}-N_{\dot{r}} \end{bmatrix}.$$

$$\begin{bmatrix} \dot{u} \\ \dot{v} \\ \dot{w} \\ \dot{p} \\ \dot{q} \\ \dot{r} \end{bmatrix} = \begin{bmatrix} \sum X \\ \sum Y \\ \sum Z \\ \sum K \\ \sum M \\ \sum N \end{bmatrix} \quad (2.2.2)$$

Since the added mass is an effect that resists to the acceleration, the calculated added mass values should take negative sign in order to conform with the sign convention.

The trajectory calculations in this thesis are performed by using the 6DOF simulation tool developed by the author in MATLAB-Simulink environment. The software development is carried out by making use of the tools readily found in MATLAB Simulink library. Outline view of the developed simulation tool is given in Figure 2.2.1.

Simulation tool first reads the input data such as initial conditions, hydrodynamic coefficients, added mass values and the vehicles physical properties from the provided input files and keeps them in the workspace of MATLAB. Then, it performs the trajectory calculations and writes the motion data into the workspace for every time step. The simulation tool is composed of 5 main blocks. The core of the simulation tool consist of the the block named "Sixdof_by_OTAS", which is derived from the block named "6DOF (Euler Angles)" of Simulink . This block calculates the state variables of the indicated time by using the forces, moments and the state variables of the previous time step and feeds the data to the block named Motion. Note that, direct usage of the "6DOF (Euler Angles)" block of Simulink is not compatible with the addition

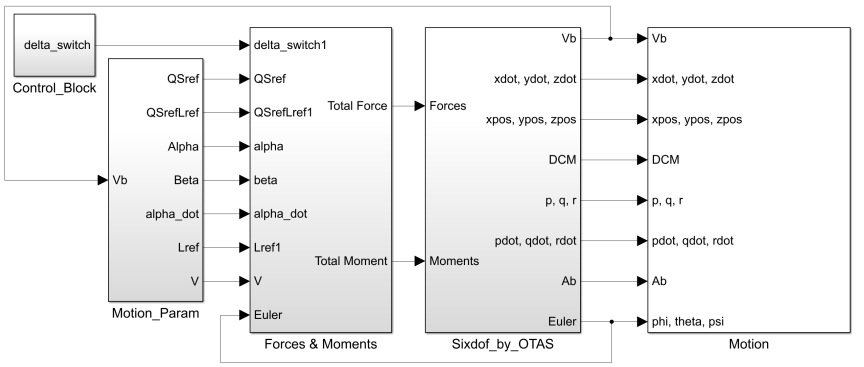

Figure 2.2.1: Outline view of the simulation tool

of added mass terms because the mass of the vehicle is represented by one scalar in the equations of motion. In order to make the block compatible with the addition of added mass, the part that calculates the rates from the forces is changed. The matrix solution of Equation (2.2.1) is implemented to the indicated block. On the other hand, the Direction Cosine Matrix (DCM) and Euler angle calculations have undergone necessary modifications in order to be compatible with the rotation order adapted in this thesis.

The Control_Block arranges the deflections of the control surfaces by using the input data provided to the tool. It employs time switches to give the desired control surface deflections at the desired instances of the simulation.

As can be inferred from its name, Force & Moments block calculates the net forces and moments on the vehicle by using the force and moment coefficients readily placed in the workspace and the state variables. n-D lookup tables are used with the data provided from the workspace and Motion_Param block in order to get the hydrodynamic coefficients corresponding to the flow conditions around the vehicle.

The Motion_Param block calculates the angle of attack and angle of sideslip of the vehicle by processing the velocity in body axis data. The required data for Motion_param block is supplied by the Motion block. In the Motion block, no calculation is performed. This block is used to gather the state variables of the vehicle from the Sixdof_by_OTAS block and save them to the workspace so that they can be

utilized in post-processing the results.

The outputs of the simulation tool for various conditions are also tested with performing unit tests.

2.2.1 Unit tests of the simulation tool

Before doing any comparisons with the output of the developed 6DOF simulation tool, it's desired to see the output of the tool for various input conditions for which the resultant motion of the vehicle can be foreseen by logical means. For this purpose, unit tests are performed using the simulation tool for several combinations of inputs and initial conditions. The different inputs include the mass properties of the vehicle and the control inputs given to the vehicle. The output trajectory and the time variation of the net forces and moments on the vehicle are observed. Other aspects of these unit tests are to see the behavior of the resultant trajectory of a vehicle for different conditions.

The unit test variables are listed below.

- Axial CG location
- Lateral CG location
- Vertical CG location
- Deflections of the control surfaces
- Initial velocity
- Initial angular position
- Propeller thrust and torque

The 6DOF simulation tool has given very reasonable and logically meaningful results in the unit tests. Test conditions and the trajectory results of unit tests can be found in Appendix A.

CHAPTER 3

ADDED MASS CALCULATION METHODOLOGY

In this chapter, information about the methodologies used for the calculation of added mass/inertia values are explained. The theory of added mass and the experimental, theoretical and numerical methods used for added mass calculation are explained in detail. Additionally, the numerical method presented in this study for calculating added mass is explained in this chapter.

3.1 Added Mass concept

When a body moves in a fluid, it should also move some amount of fluid, too. Likewise, when a body accelerates, some amount of surrounding fluid is also accelerated, which leads to the net force required to accelerate a body in a fluid greater than the multiplication of the mass of the body and the amount of acceleration. Researchers have found out that this extra force changes proportionally with the amount of acceleration. The same behaviour can be observed if the body moves in the vacuum and extra mass is attached to this mass. Therefore this effect is called “added mass”.

Since the added mass effect is a result of the acceleration of some amount of surrounding fluid, the added mass value of a body is only dependent on the shape of the body and the density of the surrounding fluid. Additionally, researchers have proven that the added mass effect is seen not only in the real fluids, but also in the ideal fluids with zero viscosity. This claim is supported by the study of Conca which proves that the added mass values are not dependent on the viscosity of the fluid [24] . Although added mass effects are present in all fluid mediums, when the density of the fluid is too small compared to the density of the moving body, amount added mass

is negligible compared to the mass of body. However, when the fluid density is at a comparable level to the body density, which is the case in water, added mass value becomes very significant. In some cases, added mass/inertia values of submerged bodies can become even higher than the mass/inertia of the moving body itself.

In short, added mass is almost always negligible for air vehicles while it's a very significant parameter for bodies accelerating under water. Besides the shape of the body and the density of surrounding fluid, added mass is dependent on the direction of acceleration. For linear accelerations, it is called added mass. Similarly, for angular accelerations it is called "added inertia". In the most generalized case, the added mass matrix of a body is composed of added mass values effective on 6 modes of motion (3 linear and 3 angular motions in x, y and z directions) occurring as a result of accelerations in 6 different modes. In other words, added mass due to an acceleration in only one direction is effective for all 6 modes of the motion, but the values of added masses/added inertia's effective on each of 6 directions are different. Each row of the added mass matrix represents the added mass/inertia effective on one mode of motion resulting due to accelerations in 6 different directions. Likewise, each column of the added mass matrix contains the added mass values effective on 6 different directions due to the motion of one mode. The resulting added mass matrix of a generalized body is represented by a 6x6 matrix shown below.

$$m_{added} = \begin{bmatrix} X_{\dot{u}} & X_{\dot{v}} & X_{\dot{w}} & X_{\dot{p}} & X_{\dot{q}} & X_{\dot{r}} \\ Y_{\dot{u}} & Y_{\dot{v}} & Y_{\dot{w}} & Y_{\dot{p}} & Y_{\dot{q}} & Y_{\dot{r}} \\ Z_{\dot{u}} & Z_{\dot{v}} & Z_{\dot{w}} & Z_{\dot{p}} & Z_{\dot{q}} & Z_{\dot{r}} \\ K_{\dot{u}} & K_{\dot{v}} & K_{\dot{w}} & K_{\dot{p}} & K_{\dot{q}} & K_{\dot{r}} \\ M_{\dot{u}} & M_{\dot{v}} & M_{\dot{w}} & M_{\dot{p}} & M_{\dot{q}} & M_{\dot{r}} \\ N_{\dot{u}} & N_{\dot{v}} & N_{\dot{w}} & N_{\dot{p}} & N_{\dot{q}} & N_{\dot{r}} \end{bmatrix} \tag{3.1.1}$$

Note that, for most application cases, due to the symmetry on XY and/or XZ planes of the body, the majority of the off-diagonal elements in Equation (**??**) are zero and some of the non-zero elements have the same value. For example, for a body having a symmetric shape in both XY and XZ planes, there is no added mass effect in the lateral direction due to the acceleration in vertical or axial direction. In such a case,

the added inertia value in the yaw direction due to the change of yaw rate is equal to the added inertia in the pitch direction due to the change of pitch rate. The added mass matrix for an AUV with symmetric body and fins reduce to the following.

$$m_{added} = \begin{bmatrix} X_{\dot{u}} & 0 & 0 & 0 & 0 & 0 \\ 0 & Y_{\dot{v}} & 0 & 0 & 0 & Y_{\dot{r}} \\ 0 & 0 & Z_{\dot{w}} & 0 & Z_{\dot{q}} & 0 \\ 0 & 0 & 0 & K_{\dot{p}} & 0 & 0 \\ 0 & 0 & M_{\dot{w}} & 0 & M_{\dot{q}} & 0 \\ 0 & N_{\dot{v}} & 0 & 0 & 0 & N_{\dot{r}} \end{bmatrix} \tag{3.1.2}$$

The exact solution of added mass is possible by the integration of the pressure along the surface area of the body. However this analytical approach is limited to very basic shapes. Since the underwater vehicles of real world are far from having very basic shapes, finding their added mass/inertia values by analytical methods is usually impossible. Therefore, lots of different methodologies for finding the added mass values of complicated shapes are proposed. In early times, most of the researchers used analytical correlations. However, due to the limitations to simple geometries and lacking of applicability to arbitrary shapes, analytical methods does not provide high levels of applicability. On the other hand, experimental determination of added mass is also possible. The detailed explanations about the experimental methods are given in the following subsections.

3.1.1 Experimental determination of added mass and inertia

The experimental determination of the added mass/inertia values of the bodies are possible by using some specialized mechanisms. The most common experimental setups used for the determination of added mass values are the Planar Motion Mechanism (PMM), proposed by Gertler [15], the Coning Motion Mechanism, used by Johnson [17] and the Rotating Arm Mechanism (RA).

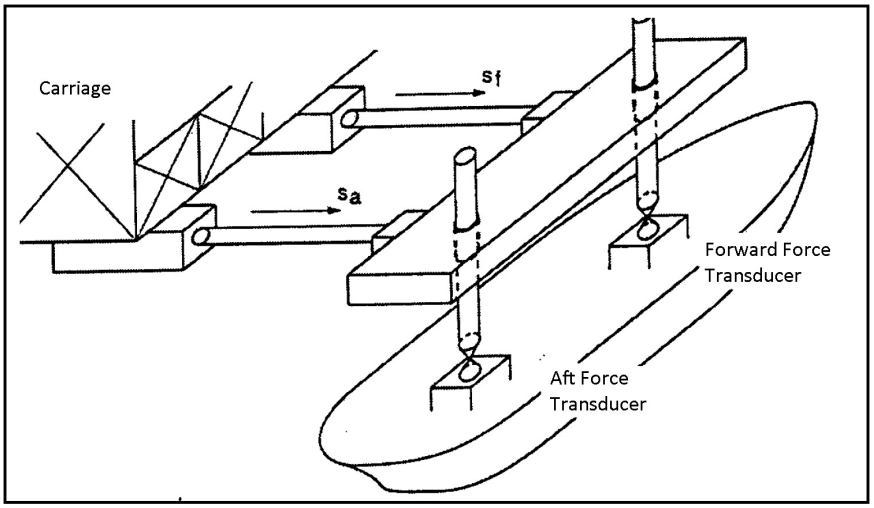

Figure 3.1.1: Schematic representation of planar motion mechanism. [25]

3.1.1.1 Planar motion mechanism

Planar motion mechanism is used for the determination of added mass coefficients of a water vehicle. The mechanism is composed of a carriage for moving the mechanism in forward and aft directions, two actuating struts for applying harmonic oscillations to the body and two force transducers for collecting the forces acting on the struts. The mechanism is constructed onto a towing tank. The schematic representation of the mechanism is given in Figure 3.1.1.

With the arrangement of the relative motions of the forward and aft struts, different modes of harmonic motions, for example, pure sway, pure yaw and combination of both can be obtained using the PMM arrangement shown in Figure 3.1.2. Similarly, by using a 90 degree rotated model, vertical modes of these harmonic motions; pure heave, pure pitch and the combinations of pitch and heave motions can also be simulated.

During PMM tests, the carriage is moving at a constant speed and the planar motion mechanism apply sinusoidal traverse, yawing, or longitudinal motions [27]. With the help of these predefined oscillatory motions, the acceleration-related derivatives (i.e. Added Mass) are obtained. In his technical report, Gertler defines the working principle of the planar motion mechanism [15]. Additionally, calculation procedure of added masses and added inertia by using the relating the forces exerted on the model

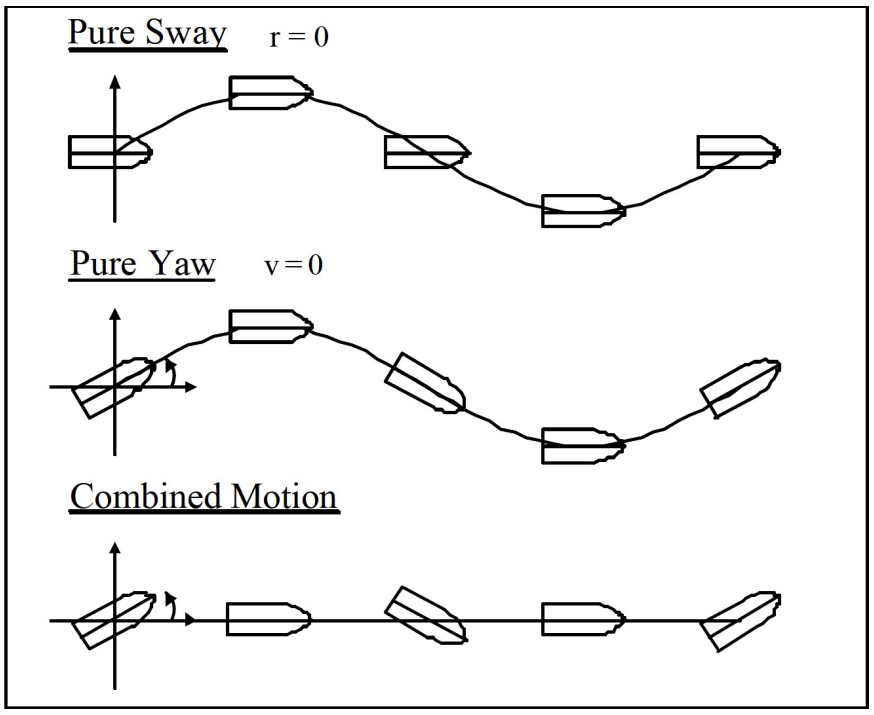

Figure 3.1.2: Different modes of motion in PMM [26]

with the predefined forced motion of the model is explained by Gertler [15]. As an example, calculation procedure of cross-flow lateral added mass value $Y_{\dot{v}}$ induced by the pure sway motion is explained in the following equations.

Below equations show the linear displacement, velocity and accelerations of the model under forced sinusoidal sway motion with an oscillating frequency of ω, where a is the maximum displacement, v_0 is the maximum velocity and $\dot{v}_0$ is the maximum acceleration.

$$y = asin\left(\omega t\right) \tag{3.1.3}$$

$$\dot{y} = \omega acos\left(\omega t\right) = v_0 cos\left(\omega t\right) \tag{3.1.4}$$

$$\ddot{y} = -\omega^2 asin\left(\omega t\right) = -\dot{v}_0 sin\left(\omega t\right) \tag{3.1.5}$$

The resultant force exerted on any strut is defined below. Here one should notice that

the value of the force on the strut is not having the same phase with the sinusoidal oscillation, but has a phase difference. The phase difference is represented by ϕ in the calculations.

$$\begin{aligned} Y_R = Y_0 sin\left(\omega t - \phi\right) &= Y_0 cos\left(\phi\right) sin\left(\omega t\right) \\ &\quad - Y_0 sin\left(\phi\right) cos\left(\omega t\right) \end{aligned} \tag{3.1.6}$$

In equation Equation (3.1.6), it can be seen that first term of the right-hand side is "in-phase" with the oscillation, while the second term is "out-phase". Therefore, one can define the magnitude of in-phase and out-phase forces as follows.

$$\begin{aligned} Y_{in} &= Y_0 cos\left(\phi\right) \\ Y_{out} &= Y_0 sin\left(\phi\right) \end{aligned} \tag{3.1.7}$$

In conclusion, by considering the Newton's 2nd law, the relation in equation Equation (**??**) can be constructed where $\left(Y_{forward}\right)_{in}$ and $\left(Y_{aft}\right)_{in}$are the in-phase forces exerted on the forward and aft struts, respectively.

$$Y_{\dot{v}} = \frac{\partial \left[\left(Y_{forward}\right)_{in} + \left(Y_{aft}\right)_{in}\right]}{\partial \dot{v}_0} \tag{3.1.8}$$

Again, more detailed explanations about the mechanism and its working principle can be found in Gertler's study [15].

3.1.1.2 Coning motion mechanism

Coning motion can be defined as the continuous rolling motion of the models longitudinal axis about the free stream velocity vector. Coning motion mechanism is used for the determination of static and dynamic effects on an underwater vehicle

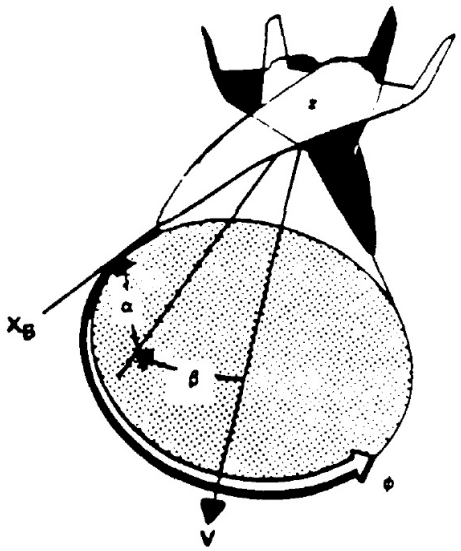

Figure 3.1.3: The coning motion[17]

due to rolling motion and the coupled effects on yaw and pitch due to rolling in non-symmetrical bodies. With the usage of planar motion mechanism, added mass coefficients of a vehicle for heave, sway and yaw motions and their combinations can be calculated. However, the effects due to rolling motion can not be determined by planar motion mechanism tests. Especially for the bodies with no appendages the derivatives of rolling motion is very small compared to other modes of motion and generally neglected. However, for the bodies with appendages, the rotation derivatives can become important. Johnson used the coning motion in order to determine the rotation related hydrodynamic coefficients of an underwater vehicle for first time [17]. The coning motion mechanism is an apparatus which is integrated to the tow tank carriage. The mechanism is set to a cone angle and rotates the model while the carriage is traveling in forward direction. The hydrodynamic force and moment data on the model is collected by the mechanism. Then the forces and moments are used for the calculation of roll dependent variables as added mass/inertia due to rolling motion and derivatives of hydrodynamic force/moments based on roll rate. The schematic representation of the coning motion can be seen in Figure 3.1.3.

In Figure 3.1.3 α_c represents the coning angle i.e. the angle between the model and rotation axis, β represents the sideslip angle, ϕ represents the body roll angle and x_B represents the longitudinal distance of center of the body with respect to the motion

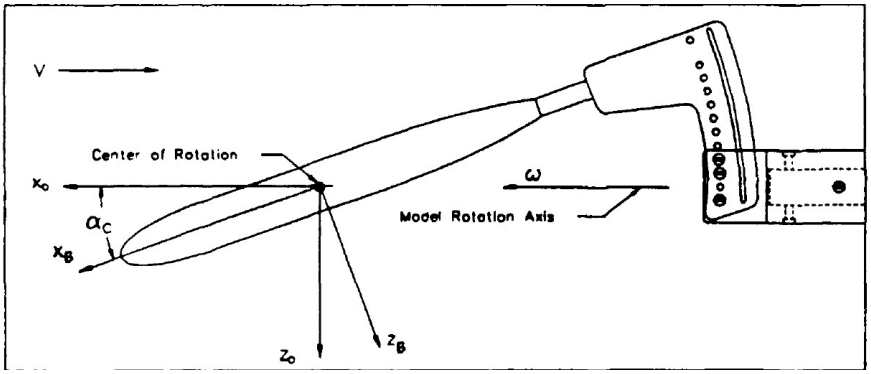

Figure 3.1.4: The coning motion mechanism [17]

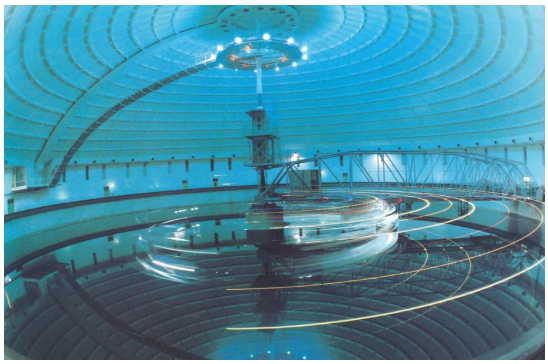

Figure 3.1.5: Rotating arm mechanism [14]

axis. The coning motion mechanism can be seen in Figure 3.1.4.

As seen in Figure 3.1.4, the model is rotated about the model rotation axis with a rotational speed of ω, with a cone angle α_c. Since the scope of this study does not involve the usage of CMM mechanism, detailed expressions relating the forces and moments with the roll dependent parameters is not given in this study. The detailed explanation and the calculation procedure can be found in Johnson's study [17].

3.1.1.3 Rotating arm mechanism

As can be inferred from its name, rotating arm mechanism employs a rotating arm with adjustable velocity and turning radius. The model is fixed to the end of the rotating arm and the arm rotates with an angular speed. Then, forces and moments on the body are measured. Figure 3.1.5 shows the rotating arm mechanism.

Since the body weight and buoyancy are known, the hydrodynamic forces and mo-

ments acting on the body due to rotation are extracted from the forces measured while the arm rotates. By using different turning radii and rotational speeds, the effect of the coefficients are calculated from the changes in the measured forces and moments. By the usage of rotating arm mechanism, not only the added mass values, bu also the maneuvering derivatives of the vehicle are obtained. Detailed information about the mechanism and working principle can be found in Jeong's article [28].

3.1.2 Numerical methods

Note that, none of the three experimental methods is capable of determination of all components of the added mass of an underwater vehicle. They are supplementing each other for obtaining the added mass parameters of the vehicle. Although they are accurate methods for obtaining the added mass values, experimental studies generally require too much time, human effort and financial resources. Therefore, experimental methods are not accessible for all. In addition to the analytical and experimental methods, there are also several numerical methods presented in literature used for the determination of added mass and inertia. Most of the numerical methods found in the literature employs Computational Fluid Dynamics (CFD) tools. Thanks to the increase in technology and computational power being more and more affordable, numerical methods are becoming a feasible choice for added mass calculations the researchers.

The general numerical approach for the determination of added mass/inertia parameters in numerical environment is based on the differences between the statically and dynamically applied forces to the body. In other words, the difference between the forces acting on the body at static and dynamic movements are treated as acceleration related effects and used in the added mass calculations. The numerical methods for added mass also obtain the numerical applications of the experimental setups mentioned in this work. The work of Philips [19], usage of CFD in order to replicate the PMM test in a numerical environment can be a good example for that. With the CFD application of the experimental methods, one can save time and financial resources while getting results with an acceptable level of accuracy. Detailed explanation about the numerical method used in this study will be given in the following section.

3.2 New method for calculation of added mass

The method developed within this thesis is the numerical application of an experimental method which benefits from the 1DOF oscillation of a simple spring-mass system underwater. The method is based on the idea stated in Blevin's book[11].

3.2.1 Review of oscillation based studies for Added Mass/ Inertia

Blevins [11] stated that the behavior of the vibrating structures in a fluid and in the vacuum is different due to the fluid effects. Blevins also states that the natural frequency of the system decreases and the damping on the system increases due to the fluid effect. He argues that the decrease in the natural frequency is caused by added mass and the added mass effect are independent of viscosity of the surrounding fluid. Chen has put considerable effort on cylindrical structures in his experimental and analytical study. Chen has constructed a 1DOF vibration system submerged in the water and inspected the effects of added mass on the vibration characteristics of a cylindrical structure. Additionally, Chen proposed expressions for calculating the added mass of cylindrical structures [29] using potential flow theory in which the inviscid and irrotational flow is assumed. Additionally, a relation between the natural frequencies of the structures and the added mass values are constructed and a calculation procedure of natural frequencies under the effect of added mass is proposed in Chen's study.

Planchard has carried out a numerical study of the natural frequencies of the tube bundle, which are often used as heat exchangers in an incompressible fluid [30]. In his study, Planchard utilized added mass values of the tube elements in order to obtain the natural frequencies. In his paper, it's also stated that the natural frequencies in water are lower than the natural frequencies in the vacuum. Another study for determining the effect of added mass on the vibration characteristics of objects has been carried out by Fu [31]. Fu has studied the hydroelastic vibration behaviors of flat plates which are partially or fully immersed in water. Fu has constructed a relation between the reduction of the resonant frequency due to added mass and the ratio of immersed part to the plate length. Additionally, the interaction between the vibrating structure and the free surface in partially submerged or near the surface conditions

has also been shown. The comparisons between the experimental outcomes and the theoretical findings have also been presented in the study of Fu. Haddara has also conducted a similar study aiming to develop a relation between resonance frequency and submerged length ratio of plates immersed in water [32]. Results of the experimental study have shown a good agreement with the analytical results. Haddara has also derived an expression for obtaining the added mass of flat plates, which is aimed to be used for determining oscillation characteristics of the internal structures of tankers and fluid cargo carriers. Similar to studies of Fu and Haddara, Vu has also conducted an experimental study in order to determine the vibration characteristics of partial or fully immersed flat plates at different depths [33]. The added mass values of flat plates which are partially or fully immersed are found by making use of the change of modal frequency of oscillation between air and water environments. Vu also shows the effect of the ratio of the submerged part to the length of the plate. The experimental results are also compared with the results of several analytical and theoretical correlations.

Bavsic has conducted a study of comparisons of added mass values in ship vibrations obtained by numerical and analytical methods [34]. The added mass values of the ships are not only important for modeling the motion, but also very essential by means of structural design due to its effect of resonant frequency. In his work, Bavsic used a finite element method called "Boundary Element Method" in order to calculate the wetted natural frequencies of a pontoon boat and compared the results with the analytical findings and reached good levels of agreement. He also derived the added mass values of the models by using the difference between dry and wetted natural frequencies of the model.

Addition to the methods proposed by the researchers, an experimental method can be derived from the ideas of Blevins and Palmer [11, 16]. This experimental method for determining the added masses may be the usage of 1DOF oscillatory mechanism. This method is based on the Palmer's study [16]. Palmer shows the relation between the vibration characteristics with the mass added to long cylindrical shells. Palmer's idea is exploited with idea of Blevins who states that the vibration characteristics of bodies in water and in vacuum differs from each other due to added mass effects [11]. By using the two ideas, a mechanism composed of a a mass and a connected spring

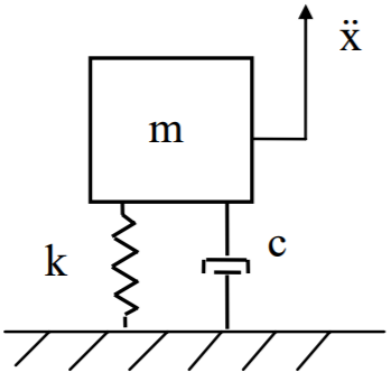

Figure 3.2.1: Simple 1-dof spring-mass-damper system

submerged in the water can be constructed to calculate the added mass of objects. It's an interesting fact that this idea was not used in any study. As stated in Palmer's study, oscillation characteristics of a body is dependent on its mass [16], stiffness of the spring and the damping ratio. Since the added mass effect acts as an additional mass connected to the body, the vibration characteristics of the system in water and in vacuum will be different [11]. Detailed information about this method and the equations relating the oscillation characteristics with added mass values are given in section 3.2.2.

3.2.2 Theory

In order to develop the theory behind the proposed method of relating the oscillatory behaviour with the added mass, free vibrations of single degree of freedom systems to initial excitation should be explained. As the simplest form, a 1DOF oscillatory system can be represented as a spring, mass and damper as shown in Figure 3.2.1.

The equation of motion of free vibration of this system can be written as follows [35].

$$m\ddot{x} + c\dot{x} + kx = 0 \tag{3.2.1}$$

where x is the deflection of the system from the equilibrium position, m is the mass, c is the damping coefficient and k is the spring constant. Since the system oscillates freely, i.e. no external harmonic excitation is applied to the system, the oscillation

frequency corresponds to the natural frequency of the system such as:.

$$\omega_n = \sqrt{\left(\frac{k}{m_{eq}}\right)} \tag{3.2.2}$$

When the system oscillates in a fluid, due to the added mass, the natural frequency of the system will be different from its natural frequency in the vacuum. Therefore, natural frequency equation can be rewritten as follows.

$$\omega_n = \sqrt{(k/\left(m + m_a\right))} \tag{3.2.3}$$

where m_a is the added mass of the body due to acceleration in the corresponding direction. So that, when the oscillatory behavior of a system moving in a fluid is inspected, one can see the effect of added mass by extracting the natural frequency of the system.

3.2.3 CFD solutions of frequency of damped system

The relation between natural frequency of vibration and the added mass was used by Chen in his study [29]. He obtained the added mass and damping values of a circular cylinder in different fluids. However, it should be kept in mind that in such an experimental setup, there is always an interaction between the mechanism and the test object. Additionally, since the experimental setup is also partly or completely submerged, added mass effect on the elements of the setup is also present in the results. Additionally, one should note that the experimental setup of a linear spring-mass system is capable of obtaining only the linear added mass effects. The added inertia's can not be found by this method, since they can only be calculated by rotating the body. However, thanks to the CFD, the added inertia can also be calculated by applying a very similar methodology with linear added-mass by using a torsional spring instead of a linear one. In this way, Equation (3.2.2) can be rewritten to relate the natural frequency of angular oscillation of a torsional spring-mass system as the following.

$$\omega_n = \sqrt{\left(\frac{k_t}{I_{eq}}\right)} \tag{3.2.4}$$

where k_t is the torsional spring constant and I_{eq} is the equivalent inertia in the corresponding direction.

Another advantage of employing CFD methods is the isolation of the model from the exciters. Since the spring is not present in the flow domain but modeled numerically as an external force, the flow around the model will not be affected by the existence of the spring present in an experimental setup.

In order to apply the presented methodology in the numerical environment, FlowVision CFD software is used. There are several reasons which lead the study to use FlowVision software. Some of these reasons are, the easiness and speed of re-meshing thanks to the Cartesian grid, the speed of the time dependent computations and the simplicity of defining force or moment on the model as a function of position of the model. In order to obtain the response of the oscillatory system in a numerical environment, Unsteady Reynolds Averaged Navier Stokes (URANS) equations are solved. A spring-mass system without any structural damping is implemented in CFD environment. In order to simulate the force due to spring effect in the computational domain, the force applied on the body is defined as a linear function of the position of the body as follows. Additionally, during the oscillatory motion of complex bodies, due to the body shape and/or numerical errors, one can expect to see different modes of oscillation at the same time. To prevent this conjunction, only the forces or moments acting on the direction of the oscillation is set to be effective on the motion of the body.

$$F = -k_v \left(P + e_i\right) \tag{3.2.5}$$

In equation above, P represents the position of the moving body, where k_v is the "virtual" spring constant of the spring. Since the initial velocity is set to zero, initial excitation, denoted as e_i, is given to the system in order to trigger the oscillatory motion. The free response position data of the model is utilized for determining the period T of the oscillations. Then the natural frequency of the system is obtained as follows.

$$\omega_n = \frac{2\pi}{T} \tag{3.2.6}$$

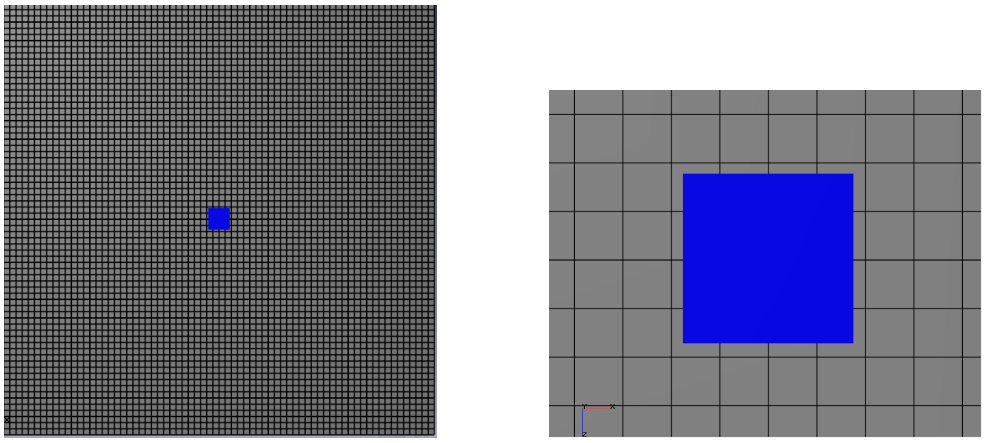

(a) Background grid around cube geometry (generalized view)

(b) Initial grid around cube geometry (close-up view)

Figure 3.2.2: Background Grid Generated Around Cube Geometry

The obtained natural frequency value is then substituted into Equation (3.2.2). Since the physical mass of the model and the spring constant is known, the added mass value of the model is calculated.

For the application of the proposed method in CFD, FlowVision CFD solver is chosen. There are several reasons for choosing FlowVision, some of them are; the fast calculation of time steps, ability to work with large time step sizes, fast remeshing thanks to Cartesian grid. FlowVision CFD solver uses a Cartesian grid to discretize the domain. The determination of the domain and grid dimensions are applied by relating the grid size with the length of the geometry. For the analysis, a cube-shaped structured grid is used with a cube-shaped domain. The domain size is arranged such that one side length of the domain is 50 times the length of the moving body. The background grid is defined as 130 divisions at each direction, which makes the background grid size about 0.4 times the model length. The background grid around a 0.1m cube can be seen in Figure 3.2.2

As can be seen from Figure 3.2.2, the background grid is too large when the dimensions and the geometry of the model are considered. Therefore, the grid refinement is done in the near vicinity of the body. The refinement is carried out up to 5th level, which results in cells nearest to the model having dimensions of 1/100'th of model length. Additionally, the number of layers having minimum cell size around the body

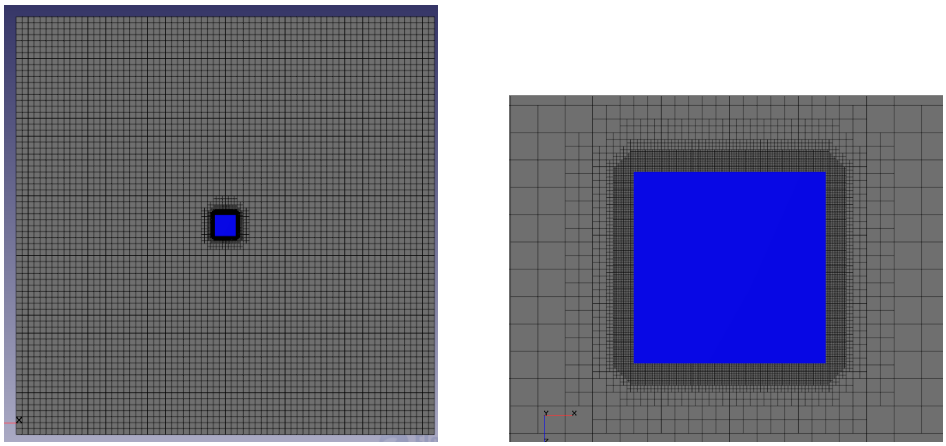

(a) Refined grid around cube (generalized view)

(b) Refined grid around cube (close-up view)

Figure 3.2.3: Refined grid near cube geometry

is arranged as 12. The grid near the cube geometry can be seen in Figure 3.2.3.

The resultant grid contains between 4 and 5.5 million cubic cells depending on the complexity of the geometry. To prevent the setup being more complex, the gravity vector which has no effect on the natural frequency of an oscillation is not included in the calculations.

The only drawback of the proposed method is that by using this method, only the added mass/inertia values for the corresponding mode of motion is obtained. In other words, only the diagonal elements of the added mass/inertia matrix given in Equation (**??**) can be obtained. Nevertheless, it's essential to keep in mind that the off-diagonal elements of the added mass matrix are almost always either equal to zero or very small to be considered.

3.3 Validation of the added mass calculation method

In this section, the verification of the proposed methodology to calculate added mass is presented. The first objective of the added mass validation is the verification of time step independence of the proposed numerical method. The second objective is the validation of the resultant added mass values obtained by the proposed methods

Table 3.1: The time steps used for dependency analysis

Name	Time Step	Ratio to T_{vacuum}	Non-dimensional Time Step
Case #1	0.05000	1/10.5	$\pi/5.20$
Case #2	0.01250	1/41.8	$\pi/20.9$
Case #3	0.00500	1/104.8	$\pi/52.0$
Case #4	0.00125	1/418	$\pi/209$
Case#5	0.00050	1/1048	$\pi/520$

by comparing the results with the analytically or experimentally obtained values in the literature.

3.3.1 Time step independence

In order to assess the time-step size dependency, free oscillations of a cube having 5m side length have been used as the test case. Five different time step values are used for this purpose. Since the time scale of the motion is determined by the period, it is better to express the time step values as non-dimensional terms. It's known that the period T is the required time for an oscillation of 2π radians, therefore, the time steps are nondimensionalized by using the period value. The time steps used in the time step dependency analyses are given in Table 3.1.

The computations are performed for the first 10 cycles of the motion due to the limitations on computational power. The change of velocity with time for five different time steps are given in Figure 3.3.1.

As it can be seen in Figure 3.3.1, the oscillation amplitude decreases as the time step increases which shows that the viscous dissipation of the body kinetic energy is dependent on the time step size. In order to see the damping characteristic obtained in different time steps more clearly, the amplitudes of the oscillation velocities changing with time and the corresponding damping factors, extracted from the exponential decay of the oscillation amplitudes are given in Figure 3.3.2.

Figure 3.3.2 shows that the damping factor obtained by using different time steps are highly different from each other. Additionally, when the damping parameters changing with time step is considered, there seems to be a time step convergence

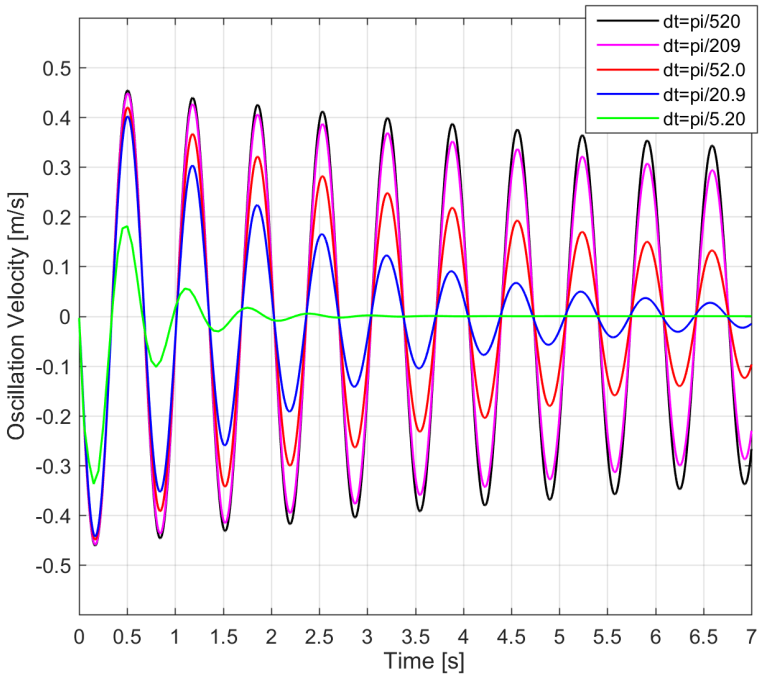

Figure 3.3.1: The velocities for five time steps

about 10^{-3} radians of the non-dimensional time step. This can be interpreted as so; when dealing with the damping of the surrounding fluid on the free vibrations of a body, one should use a very small time step compared to the period of the oscillation.

It's crucial to note that, the main perspective of this work is not to obtain the damping but the added mass values. In order to better perceive the problem, one should realize that the added mass is not affected by the viscous dissipation. Added mass is, in fact, a product of the kinetic energy that is gained by the fluid from the accelerating object in it, not the kinetic energy dissipated in the fluid because of the viscosity [24]. Therefore, the periods of the oscillation is the main object of consideration. From the results, one can see that the velocities for four cases, namely Case#2, Case#3, Case#4 and Case#5 cross the $V = 0$ line almost at the same times, which concludes the result of that the oscillations found by these four different time steps employ practically identical periods. The periods found by using five cases and the percent differences from the case of smallest time step are given in Table 3.2. The change of added mass values with respect to time step are shown in Figure 3.3.3.

In Figure 3.3.3, it is clearly seen that the added mass values convergence with time

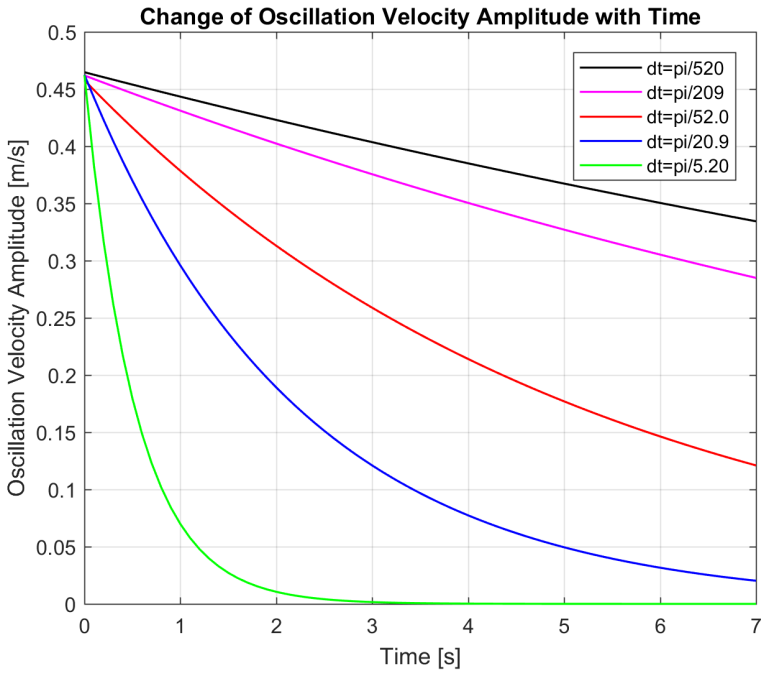

(a) Oscillation velocity magnitude

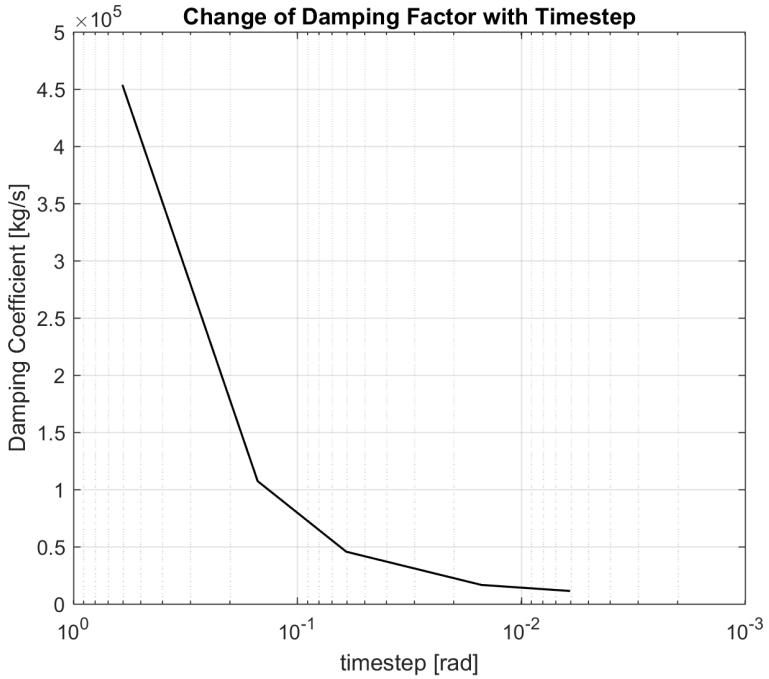

(b) Damping factor

Figure 3.3.2: The oscillation velocity magnitudes and corresponding damping factors

Table 3.2: Periods of oscillation for five different time steps

Case	Time Step	Period $[s]$	% Difference
Case#1	$\pi/520$	0.6761	—
Case#2	$\pi/209$	0.6763	+0.03
Case#3	$\pi/52.0$	0.6760	-0.01
Case#4	$\pi/20.9$	0.6740	-0.31
Case#5	$\pi/5.20$	0.6358	-5.95

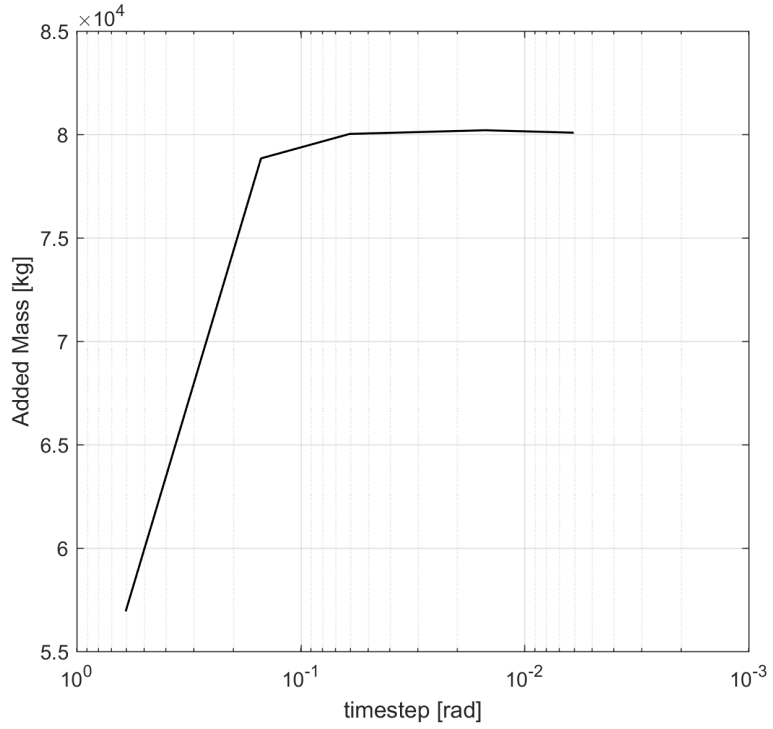

Figure 3.3.3: Change of added mass value with time step

Table 3.3: The parameters for cube geometry

Side Length [m]	Mass [kg]	k [N/m]	Initial Excitation [m]	T in the Vacuum [s]
0.1	4	144	0.3	1.0471

step occurs very rapidly. As a result, it can be said that, except the largest time step, the periods obtained with four different time steps and corresponding added mass values are virtually identical to each other. Since, the calculation of damping of water effective on the vibrating bodies by the numerical method is not in the scope of this work, time step values can be chosen by considering only the periods. Although the time step value of Case#2 ($\pi/20.9$) seems to be reasonable, in order to be on the conservative side and use the computational power wisely without sacrificing accuracy of the added mass of the body, the time step in is used in the simulations chosen as equal or less than that of Case#3 ($\pi/52.0$).

The time step value determined by this study is used for all the simulations performed in FlowVision CFD software.

3.3.2 Validation of the added mass results

This section provides information about the studies performed to validate the proposed method for obtaining added mass values. For this purpose, basic geometries like the cube and the sphere are utilized. Since added mass of these geometries are available in the literature through analytical solutions and or experimental studies.

3.3.2.1 Added mass for cube geometry

First validation study is performed by using a cube geometry having one side length of 0.1m. The numerically defined mass, virtual spring constant, initial excitation parameters are chosen to have a period about 1 seconds and have the oscillation velocity amplitude-based Reynolds number between 10^1 and 10^5. The chosen parameters and the corresponding period in the vacuum are tabulated in Table 3.3.

The change of velocity amplitude with time is given in Figure 3.3.4. The period of os-

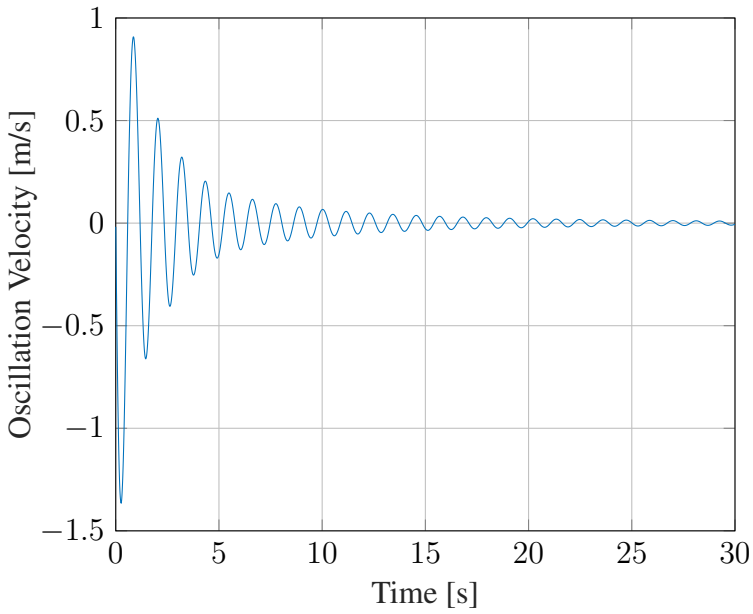

Figure 3.3.4: Oscillating velocity of the cube geometry

Table 3.4: The periods and corresponding added masses of the cube geometry

T in the Vacuum [s]	T in Water [s]	Calculated m_{added}	Analytical m_{added}	% Difference
1.0471	1.1298	0.66 kg	0.67 kg	1.49

cillation change with Reynolds number for cube geometry can be seen in Figure 3.3.5.

As it can be observed from Figure 3.3.4 and Figure 3.3.5 , the magnitude of velocity diminishes with time and reaches a value very close to zero. On the other hand, observing the oscillation periods, an unusual change with Reynolds number based on the oscillatory velocity can be realized. Thus when calculating the added mass values, it's more convenient to take the values at where separation is not expected. The resultant periods of oscillations with corresponding added mass values, compared with the experimental results given by Blevins [11] are tabulated in Table 3.4.

From Table 3.4, It is concluded that there exist an excellent agreement between the results of the proposed method and those obtained by experimental method for the cube case.

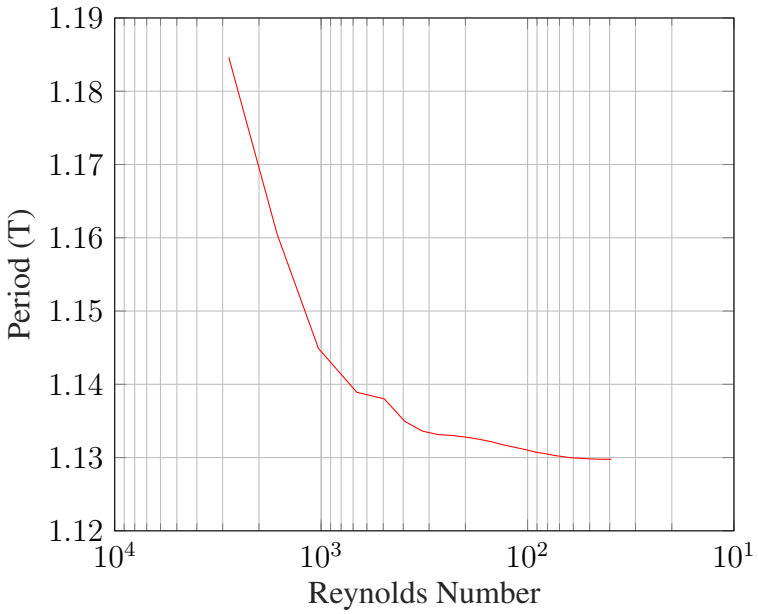

Figure 3.3.5: The period of oscillation for cube geometry

Table 3.5: Parameters of sphere cases

Radius [m]	Mass [kg]	k [N/m]	Initial Excitation	T in the Vacuum [s]
0.31	120	17280	0.05	0.5236

3.3.2.2 Added mass for sphere geometry

The other validation study is performed using a sphere geometry, for which analytically exact solution of added mass exists in the literature. The parameters about the sphere geometry and the input parameters defined in order to have a body density close to the density of water and a low maximum velocity in order to have the Reynolds number between 10^1 and 10^5. The chosen parameters are given in Table 3.5.

The velocity amplitude changes with time and period of oscillation change with Reynolds number for sphere geometry is given in Figure 3.3.6 and Figure 3.3.7, respectively.

In Figure 3.3.7, the value of the oscillation period seem to be changing with respect to the Reynolds number. However, the range of the vertical axis of the plot is very small compared to the value of the period itself. The resultant values along with the comparison with the analytical results are tabulated in Table 3.6

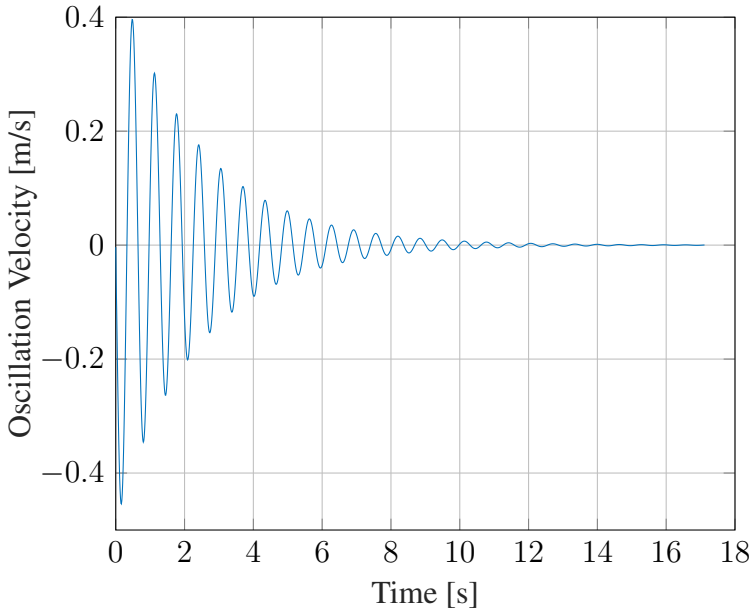

Figure 3.3.6: Oscillating Velocity in Sphere Case

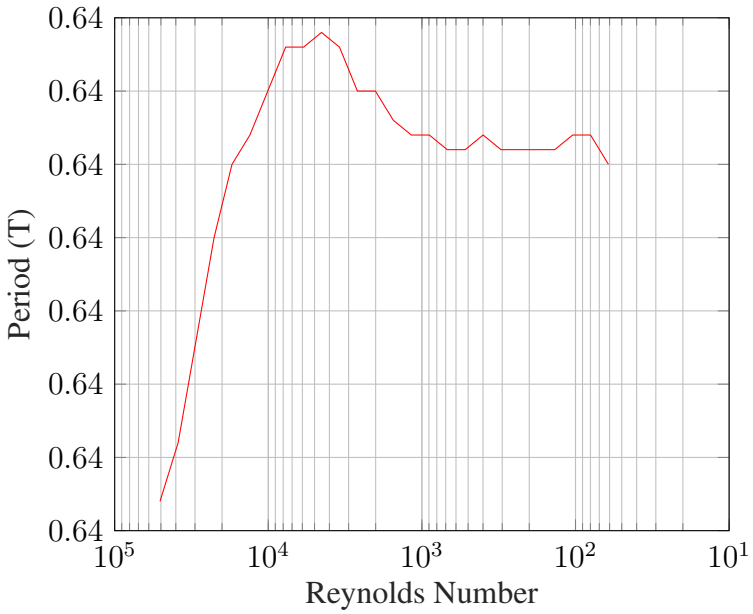

Figure 3.3.7: The Period of Oscillation For Sphere Case

Table 3.6: The periods and corresponding effective masses of cubes

T in the Vacuum [s]	T in Water [s]	Calculated m_{added}	Analytical m_{added}	% Difference
0.5236	0.6434	61.20 kg	62.39 kg	1.91

Table 3.7: Parameters of ellipsoid case

Max. Diameter [m]	Length	Mass [kg]	k [N/m]	Initial Excitation	T in the Vacuum [s]
0.191	1.33	30.5	4392	0.05	0.5236

Table 3.8: The periods and added mass values of ellipsoid

T in the Vacuum [s]	T in Water [s]	Calculated m_{added}	Analytical m_{added}	% Difference
0.5236	0.5313	0.91 kg	0.93 kg	-2.2

In the results, there seem to be a very small discrepancy. The most likely reason for the indicated discrepancy may be the effect of separation of flow from the sphere in the computational solutions. One should keep in mind that the analytically exact solution is done by using the potential flow theory which does not involve separation by its nature.

3.3.2.3 Added mass for ellipsoid geometry

In order to ensure the capability of the new method, the added mass value of an ellipsoid which has the same length and diameter as Remus AUV is calculated using the numerical approach proposed in this study. The physical parameters of the ellipsoid is given in Table 3.7 .

The axial added mass value of the ellipsoid obtained by the numerical method and the analytical value are given in Table 3.8.

CHAPTER 4

VALIDATION TESTS

In this section, verification of the methods explained in the previous chapters is presented. The verification subjects include

- the calculation of added mass,
- static hydrodynamic database and
- the trajectory simulation results.

The verification of the added mass calculations is performed on basic geometrical shapes for which the experimental or analytical data can be found in the literature. The verification of the static CFD analyses is performed by using the Darpa Suboff geometry [36], for which experimental results are present in the literature [37]. The verification of the trajectory results is performed by using Remus AUV model for which theoretical and experimental trajectory data are available [9].

4.1 CFD database extraction

As stated previously, the trajectory results of the Remus AUV that is obtained by using the added mass values proposed by this method is compared with the experimental and analytical results. In order to perform 6DOF motion simulation, the static hydrodynamic database of Remus geometry is generated by using Fluent CFD solver. Computations are performed by using the Pressure-Based Coupled algorithm with second-order upwind scheme. Since the flow is incompressible, the energy equation is not included in the computations. As the turbulence model Spalart-Allmaras one-

equation turbulence model is employed. The usage of Spalart-Allmaras turbulence model for incompressible external flows was found suitable by different authors in various studies [38, 39]. The verification of mesh independence of the static CFD simulations and comparisons with the experimental data are explained in the following sections.

4.1.1 Mesh independence study

In order to use the computational resources efficiently without compromising the accuracy of the solution, a mesh dependency study is carried out. For the mesh dependency study, 1.54 m/s of velocity and -4 degrees angle of attack is chosen as the flow condition. 6 different meshes with different surface mesh sizing, volume mesh sizing and growth ratio are generated. For all the 6 cases, the boundary layer grid parameters are kept constant. The first layer thickness of the boundary layer grid is determined by aiming to keep the y^+ values under unity and the number of layers and aspect ratio is determined by aiming to safely capture the boundary layer velocity profile. As a result, 15 layers of inflation mesh with the last aspect ratio of 4 are generated onto the Remus geometry by using a first layer thickness of 0.00001m. For the 6 meshes, static CFD calculations are carried out using the same solution parameters for all of them. The change of normal force with respect to the change in the grid element size is plotted in Figure 4.1.1.

When Figure 4.1.1 is analyzed, it can be seen that the normal force changes as the mesh element size increase up to 5 million cells. However, from 5 million to 6.5 million, there is no significant change in the value of the normal force coefficient. As a result of this study, one can conclude that 5 million cells can be enough to obtain mesh independent results. Therefore, the static CFD analyses are carried out by using the mesh having 5 million elements. Mesh resolution on the nose and tail of the Remus geometry is shown in Figure 4.1.2.

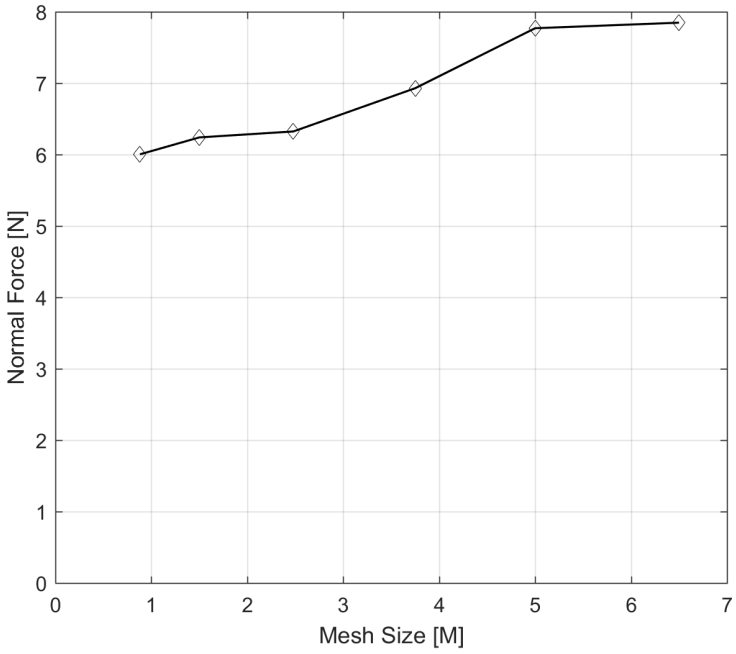

Figure 4.1.1: Normal force changing with element size

4.1.2 Verification of static CFD results with experimental data

In order to evaluate the CFD setup, a comparison study with the experimental data is conducted. For this purpose, Darpa Suboff geometry is used. In order to evaluate the CFD setup, all the solution parameters used for Remus AUV is directly used for Darpa model with a similar mesh density. Darpa Suboff model was generated by David Taylor Research Center [36] in order to supply experimental data for evaluation of CFD codes. Details of the Darpa Suboff geometry can be found in Figure 4.1.3.

The details of the geometry can be found in [36]. For the evaluation purposes, axial force, side force and yawing moment coefficients of Darpa model with bare hull configuration are compared with the experimental results obtained by Roddy [37].

The experimental and numerical results of the coefficients changing with the angle of drift/sideslip are presented in Figure 4.1.4.

As it can be observed from Figure 4.1.4 , except the acceptable difference in axial force coefficients, the static CFD analyses have an agreement with the experimental data. The source of discrepancy in the axial force data might either be the CFD

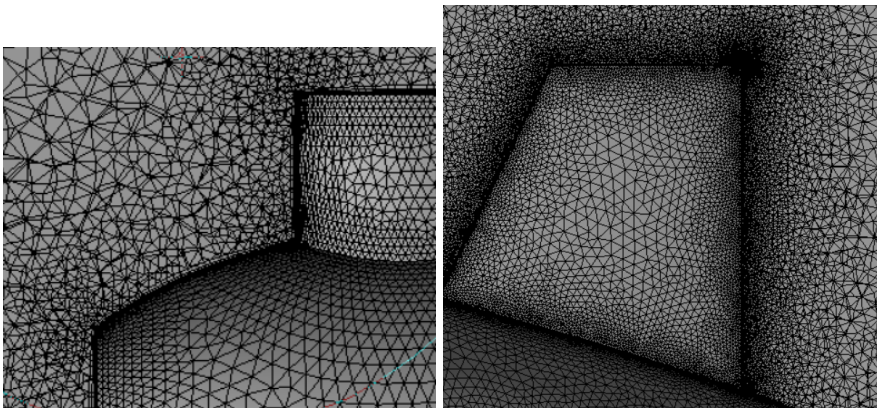

(a) Grid around the nose (b) Grid around tail fin

Figure 4.1.2: Final mesh resolution

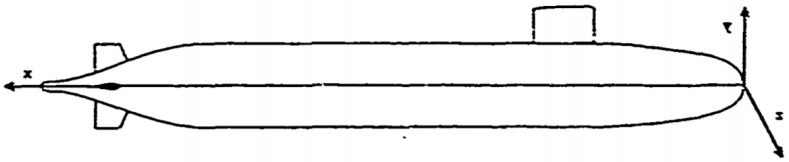

Figure 4.1.3: Darpa Suboff model

method or the interaction between the model and the towing tank struts. Nevertheless, the results are close enough to each other to say that the setup can safely be used for static hydrodynamic database extraction of Remus AUV geometry, which has a very similar shape with Darpa Suboff model.

4.2 Trajectory simulations

In this section, verification of the 6DOF trajectory simulations is discussed. For the validation of trajectory simulations, Remus AUV is chosen as the model. Remus is a compact light-weight Autonomous Underwater Vehicle designed and developed by Woods Hole Oceanographic Institution. Remus AUV is used for underwater research applications. Experimental trajectory data of Remus AUV was obtained by Prestero and can be found in Prestero's thesis [9]. The details of the Remus geometry can be found in Figure 4.2.1 and Table 4.1. Further details concerning the geometry of

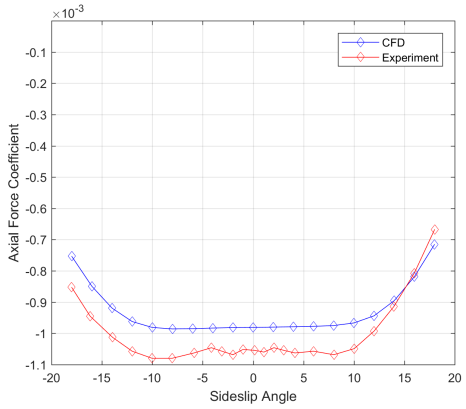

(a) Axial force coefficient

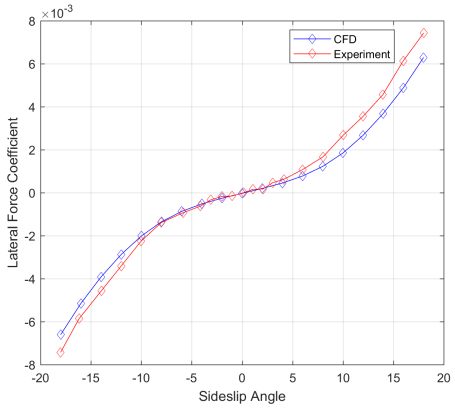

(b) Lateral force coefficient

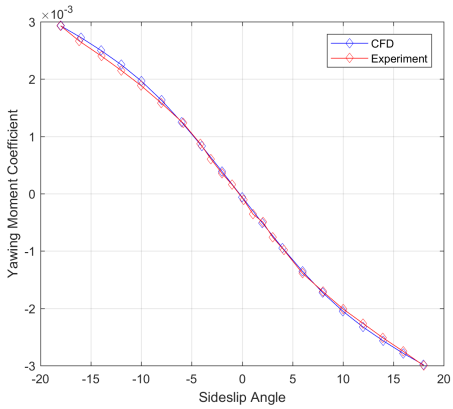

(c) Yawing moment coefficient

Figure 4.1.4: Comparison of the numerical data with the experimental data

Remus and its mass properties could be found at [9].

In order to perform the trajectory simulations, the static and dynamic hydrodynamic database and the added mass/inertia values of the vehicle are obtained using the methodologies explained previously.

4.2.1 Generation of the hydrodynamic database

The hydrodynamic database includes the static hydrodynamic coefficients and the dynamic (damping) derivatives of the corresponding vehicle. When generating the hydrodynamic database of a vehicle, one should be aware of the fact that the database should contain the hydrodynamic parameters of the vehicle correctly within the flow

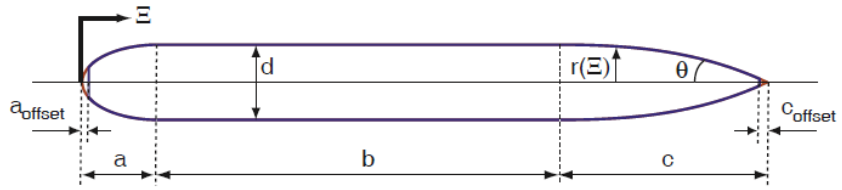

(a) Body

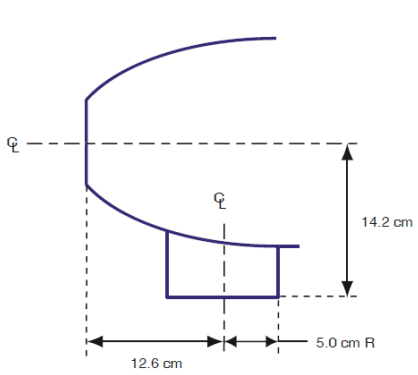

(b) Nose

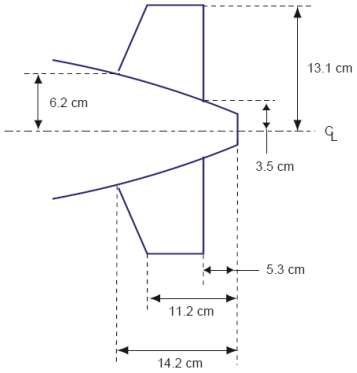

(c) Tail

Figure 4.2.1: Remus AUV body, tail and nose geometry details [9]

conditions that the vehicle will experience. In other words, care must be taken about determining the flow conditions at which the database will be generated. In order to determine the flow conditions, the velocity profile of the Remus AUV is analyzed [9]. In his thesis, Prestero stated that the cruising forward velocity of the Remus AUV is about 1.54 m/s. Additionally, in the results of the simulations carried out by Prestero, it's seen that total velocity of the Remus AUV is in some cases lower than 1.54 m/s but higher than 1 m/s at all times. As a result, three different velocities, namely 1 m/s, 1.54 m/s and 2 m/s is decided to be sufficient for representing the whole speed regime of the vehicle. For those speeds, corresponding Reynolds numbers based on the diameter of the vehicle are given in Table 4.2.

When defining the angle of attack range, again the velocity profiles in the Prestero's work has been analyzed [9]. When the ratio of the downward and forward velocities of the vehicle in body coordinates is examined, the angle of attack of the vehicle apparently maintains a maximum of 5 degrees. Therefore, in order to exploit the computational resources efficiently, the angle of attack regime was defined initially as changing from -4 degrees to +4 degrees. However, during the initial simulations

Table 4.1: Body parameters of Remus AUV

Parameter	Value	Units	Description
a	1.91E-01	m	Nose Length
a_{offset}	1.65E-02	m	Nose Offset
b	6.54E-01	m	Mid body Length
c	5.41E-01	m	Tail Length
c_{offset}	3.68E-02	m	Tail Offset
n	2	n/a	Exponential Coefficient
θ	4.36E-01	radians	Included Tail Angle
d	1.91E-01	m	Maximum Hull Diameter
l_f	8.28E-01	m	Vehicle Forward Length
l	1.33E+00	m	Vehicle Total Length

Table 4.2: Reynolds numbers for CFD database

V[m/s]	1.0	1.54	2.0
Re	160504	247176	321008

carried on using developed Simulink tool, it's seen that the angle of attack exceeds 4 degrees. Extrapolating the angle of attack range in Simulink might represent a favorable choice as long as flow separation is not observed. However, in order to defeat the consequences of ignoring flow separation, the angle of attack range of the analyses are extended. The resultant AOA range is changing from -11 degrees to +11 degrees with a 1 degree step size.

Since the Remus AUV has a -5 degrees rolled orientation when cruising, the vehicle inevitably maintain an angle of attack together with a non-zero sideslip angle. Therefore, in the simulations, there will be always a non-zero angle of sideslip when the angle of attack is non-zero. To satisfy the need to have coefficients at non-zero sideslip angles, the sideslip angles of -5 degree and 5 degree are added to the flow conditions.

The deflection angles of the tail fins are determined by the experimental study carried on by Prestero [9]. As a result, in addition to the zero deflection case, the elevator deflections of -4 and +4 degrees are included in the solution matrix.

The final solution matrix is composed of a total number of 621 runs as given in Table 4.3.

Table 4.3: The solution matrix of the static CFD database

Parameter Name	Values
Velocity [m/s]	1.0, 1.54, 2.0
Angle of Attack []	-11, -10, -9, -8, -7, -6, -5, -4, -3, -2, -1, 0, 1, 2, 3, 4, 5, 6, 7, 8, 9, 10, 11
Side Slip Angle []	-5, 0, +5
Elevator Deflection Angle []	-4, 0, +4

The static hydrodynamic database of the Remus AUV generated by using Fluent CFD solver. After the simulations, the force and moments on the vehicle are non-dimensionalized following the procedure explained in Section §4.1. Note that when obtaining the moments on the vehicle, the reference point is taken as the CB of the vehicle for which coordinates are given in Table 4.4.

Table 4.4: Coordinates of CB with respect to center of the nose

x_b	-0.611 m
y_b	0 m
z_b	0 m

Determination of the dynamic derivatives is performed by using Missile DATCOM. Missile DATCOM is a semi-empirical tool, generally used for obtaining the static and dynamic aerodynamic coefficients of air vehicles. Missile DATCOM is also utilized for low Mach/ Reynolds dependent flows around tubular bodies with fins. Therefore it is applicable to AUVs.

A similar study has also been carried out by Nahon [40]. In his study, Nahon used USAF DATCOM in order to obtain the hydrodynamic derivatives of an undersea vehicle. Nahon also claims a good agreement between the data generated by DATCOM with those obtained by experimental studies. The dynamic derivatives are obtained for the velocities and angles of attack in Table 4.3 for zero deflection and sideslip angles.

4.2.2 Added mass calculations

In order to have a proper simulation of an underwater vehicle, besides the static and dynamic hydrodynamic coefficients, the added mass values of the model should be obtained to be employed in the simulation tool. In this study, a new method for the numerical calculation of the added mass is used. The method is based on the difference of vibration behaviors of a single degree of freedom vibrating system in water and in vacuum.Time dependent RANS computations under 6 different modes of free oscillation of Remus AUV is performed in the FlowVision CFD software. FlowVision is a CFD software which is based on finite volume approach to approximation of the partial differential equations describing fluid motion.

In order to use the computational power efficiently, it is important to observe sufficient amount of vibration cycles in a limited computational time. For this purpose, the natural frequency of 12 s^{-1} seem to be a reasonable value. The physical parameters as spring constant and the mass of the model is arranged such that the natural frequency has value of 12 s^{-1} and resultant period in the vacuum is calculated as 0.5236 s. The magnitudes of torsional spring constant and the inertia of the vehicle in three main modes are kept the same with the linear spring constant and the mass, respectively, in order to keep the computations easy as possible. For a vehicle having a shape like Remus, having equal mass and inertia is physically impossible, however the method developed in this study does not require these values to be the same as the physical quantities of the vehicle. Note that the added mass is a function of the external geometry only and surrounding fluid has nothing to do with the physical mass or mass distribution of the vehicle. The computations are carried out along 55 to 60 periods, which is far enough for the natural frequency of the system to converge and the Reynolds number based on the diameter of the vehicle to drop below unity. The values of the parameters used in the computations for added masses and inertiae are given in Table 4.5 and Table 4.6, respectively.

The computational grid is generated by adapting the mesh density as explained in Section §3.2 . The Cartesian grid generated around the Remus AUV geometry can be seen in Figure 4.2.2

Table 4.5: The parameters of the linear oscillatory motion

Parameter	Value
k_v	4392 $N.m^{-1}$
e_i	0.05 m
m	30.5 kg

Table 4.6: The parameters of the angular oscillatory motion

Parameter	Value
k_v	4392 $N.m.rad^{-1}$
e_i	0.05 rad
I	30.5 $kg.m^2$

In Section §3.2, it's stated that the method is capable of obtaining 6 added mass/inertia values for 6 modes of motion. However, during the added mass calculations of Remus AUV, it is seen that the rolling added inertia of the geometry is too small. It's important to note that round body shapes does not have added mass in roll direction, the only contribution to rolling added mass of Remus AUV is that from the tail fins and sonar transducer. The contribution of tail fins and sonar transducer to the rolling added mass of Remus is too small compared to other components of added mass. Therefore, it is difficult to obtain numerically of such a small effect in a CFD environment. Therefore, the $K_{\dot{p}}$ value is not obtained by the numerical method, instead the analytical finding of Prestero is used in the trajectory simulations. The computations for 5 different modes, namely; forward, lateral, vertical and pitch and yaw oscillations are performed by using FlowVision and the resulting oscillatory velocities for these modes are given in Figure 4.2.3

The periods of the oscillations shown in Figure 4.2.3 are given in Table 4.7 with the period in the vacuum values.

Table 4.7: Periods of oscillation of Remus AUV in different modes

Mode	Period in the Vacuum	Period in Water
Forward	0.5236	0.5387
Lateral	0.5236	0.7393
Vertical	0.5236	0.7458
Pitch	0.5236	0.5489
Yaw	0.5236	0.5506

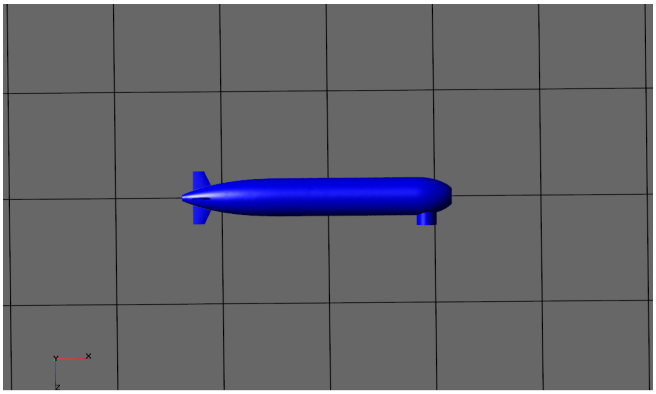

(a) Initial grid generated around Remus AUV

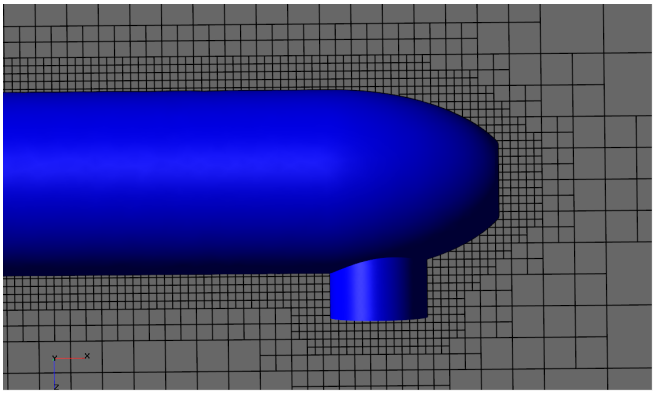

(b) Refined grid generated around Remus AUV

Figure 4.2.2: Computational grid generated around Remus AUV

The natural frequencies of the oscillations are found by substituting the period values in Table 4.7 into Equation (3.2.6), then the natural frequencies are used to calculate the added mass and inertia values bu using Equation (3.2.2) and Equation (3.2.4), respectively. The resultant added mass and inertia values of the calculations and the theoretical findings of Prestero are listed in Table 4.8.

As can be seen from the results, the largest percent difference occurs in the added mass value in forward motion, this can be because of Prestero, using axial added mass of an ellipsoid as the axial added mass value of Remus. This approach apparently is not precise enough. Because of the bluntness of the nose and the large perturbation element just after the nose makes the Remus geometry far from an ellipsoid, especially considering the nose shape. The axial added mass value of the ellipsoid obtained by the numerical method and the analytical value that's used by Prestero are given in Table 4.9.

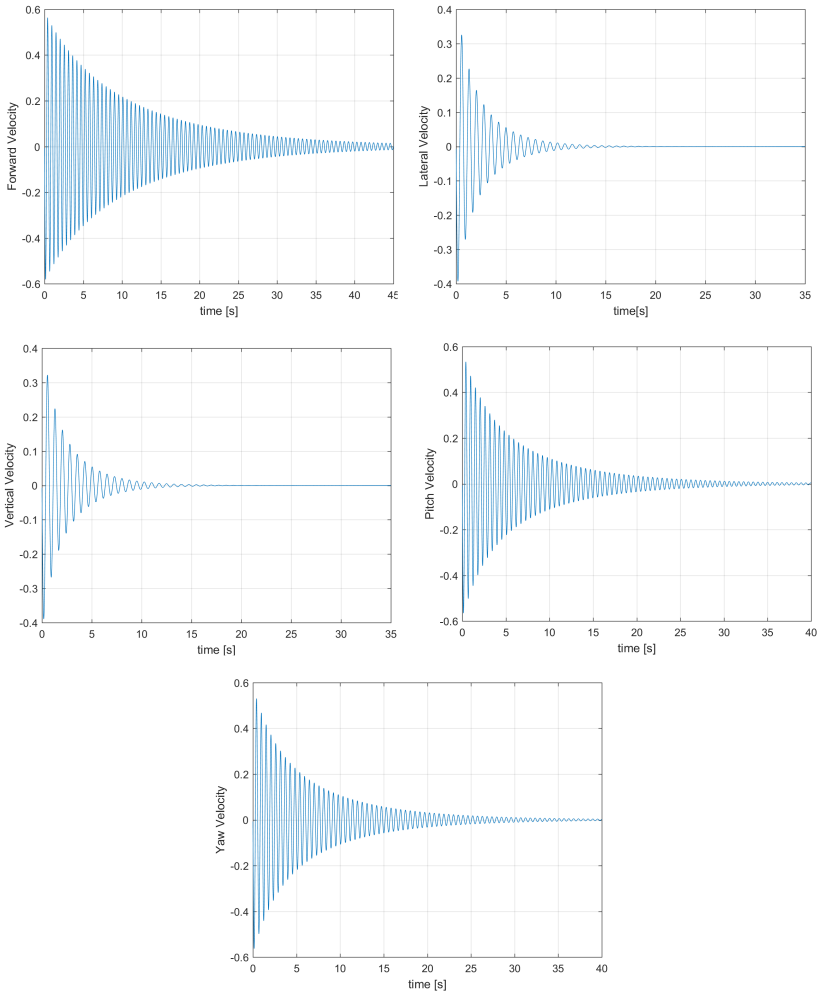

Figure 4.2.3: The oscillatory behaviors of the Remus AUV in 5 different modes

The results in Table 4.9 show that the difference can be due to the nose bluntness and sonar transducer of the Remus AUV. The improvements on calculation of added mass and inertia values by the method used in this study are as follows:

- The method perceive the difference between $M_{\dot{q}}$ and $N_{\dot{r}}$ values, due to the sonar transducer, which is not possible with the theoretical calculations.

- Similarly, the difference between $Y_{\dot{v}}$ and $Z_{\dot{w}}$ values is also perceived by the presented method.

Table 4.8: Values of added mass and inertia

Parameter	Computational Result	Prestero	% Difference
$X_{\dot{u}}$	1.785 kg	0.93 kg	92
$Y_{\dot{v}}$	31.38 kg	35.5 kg	-11.6
$Z_{\dot{w}}$	30.31 kg	35.5 kg	-14.62
$K_{\dot{p}}$	—	0.0704 $kg.m^2$	—
$M_{\dot{q}}$	3.02 $kg.m^2$	4.88 $kg.m^2$	-38.12
$N_{\dot{r}}$	3.24 $kg.m^2$	4.88 $kg.m^2$	-33.61

Table 4.9: Axial added mass value of ellipsoid

Numerical Data	Analytical Data	% Difference
0.91 kg	0.93 kg	-2.2

4.2.3 Trajectory simulations

After obtaining the hydrodynamic database including the static and dynamic coefficients and added masses, the trajectory simulations of Remus AUV are performed by using the simulation tool developed for this study. Note that Equation (2.2.2) is written for the most generalized case. When the geometry of Remus AUV is considered, it is obvious that some of the parameters of the 6-by-6 added mass matrix are zero. The Remus AUV geometry is symmetric in XZ plane and the only element that disturbs the symmetry on XY plane is the sonar transducer at the forward end of the vehicle. Therefore, an assumption of symmetry in XY plane is acceptable. With this assumption, the added mass matrix of Remus AUV reduces to Equation (3.1.2);

Due to the symmetry, the number of added mass parameters reduced from 36 to 10 and the magnitudes of the four off-diagonal terms are equal to each other. Noting that the proposed method is not capable of obtaining the off-diagonal terms of the added mass matrix and keeping in mind that the $K_{\dot{p}}$ value is not calculated by the numerical method, the number of the values taken directly from the method described at Prestero's thesis reduces to 2 which are $K_{\dot{p}}$ and any one of $Y_{\dot{r}}$, $Z_{\dot{q}}$, $M_{\dot{w}}$ and $N_{\dot{v}}$.

The Remus AUV geometry contains a propeller at the tail section. Therefore the propeller effects are added to the equations of motion as an axial force and rotational moment. Note that, Prestero did not report propeller thrust and torque, instead, he has calculated the propeller thrust from drag calculations estimated from the speed of the

AUV from the test data. Then, torque is estimated from the propeller thrust. The same method is utilized for this thesis. Since drag coefficients are different, thrust -hence torque- values are found to be significantly different than the original study. Notice, our drag database involve the effects of the radar dome, as well as the actual shape of the Remus, which is more blunt than the approximate shape utilized by Prestero. Therefore, this difference is expected.

With the simulation tool and provided data in this study, two different trajectory simulations with a duration of 4 seconds are performed and the results are compared with the experimental trajectory data given in Prestero's thesis [9].

In the first case, the vehicle is under 4 degrees of negative elevator deflection for the first 2 seconds then 4 degrees of positive elevator deflection for another two seconds. The results are compared in Figure 4.2.4.

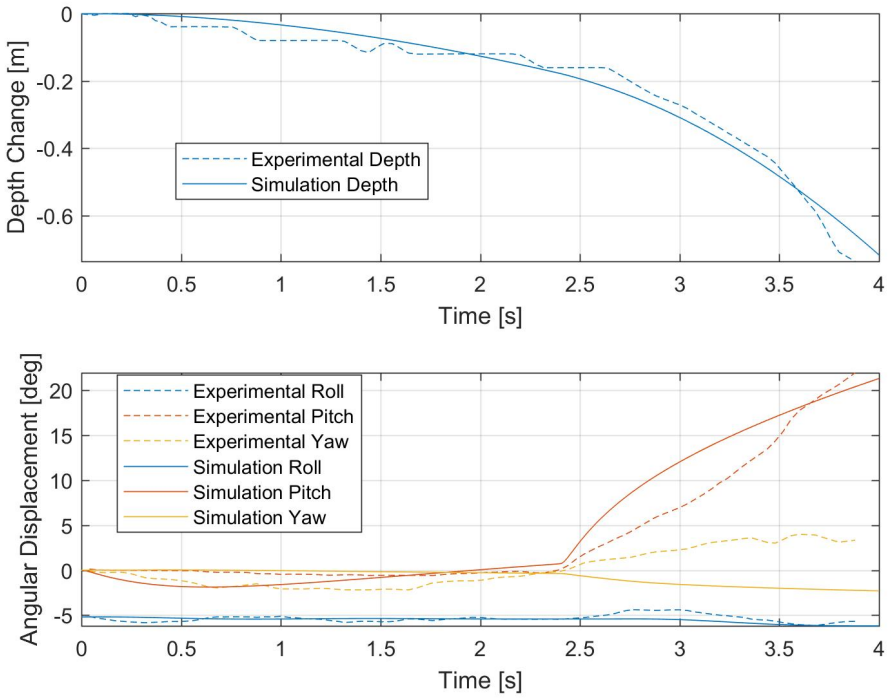

Figure 4.2.4: Vehicle depth and orientation change in simulation case 1

In the second case, for the first two seconds, the vehicle is applied 4 degrees of negative elevator deflection again, for the next 2 seconds, the vehicle has 8 degrees of negative elevator deflection. The results are compared in Figure 4.2.5.

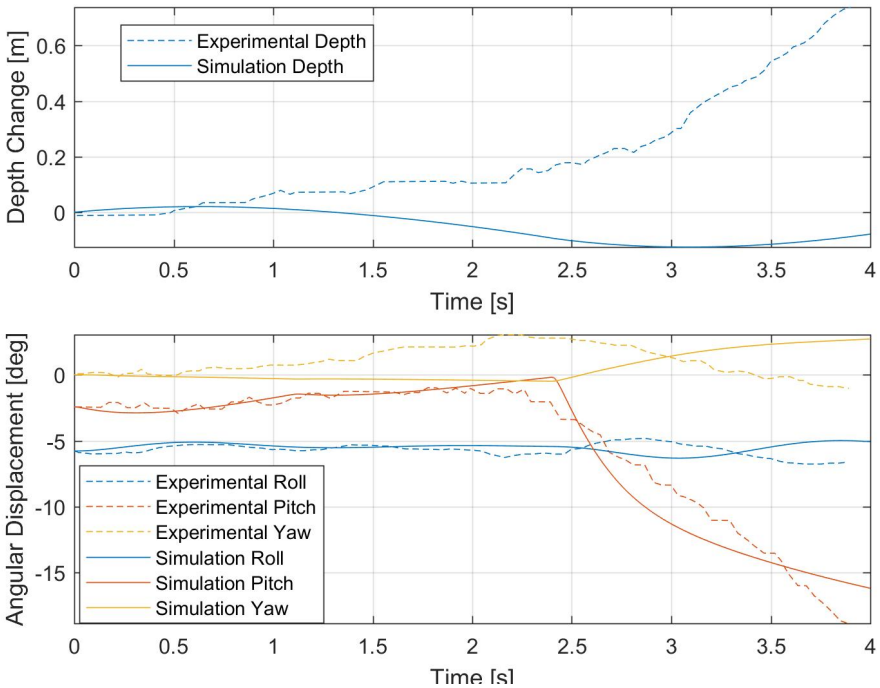

Figure 4.2.5: Vehicle depth and orientation change in simulation case 2

When the results seen on Figure 4.2.4 are analyzed, it can be realized that there is a disagreement between the yaw results. However, the magnitude of yaw angle is very small compared to the pitch angle seen in the simulation results. Except the difference in yaw, it can be stated that simulation results are in a good agreement with the experimental data.

When the results of the second case, seen in Figure 4.2.5 are analyzed, a significant difference in depth change values can be observed. The orientation of the vehicle seem to be consistent with the experimental data. Prestero reported uncertainties on vehicle center of gravity and buoyancy, indicting that some ballasts to adjust those properties slides during the maneuvers. Actually, it is possible to re-calibrate our simulation tool for each case by adjusting the center of gravity and buoyancy. However, since the two tests are performed at the same day, we have avoided the buoyancy and CG alteration. Therefore, this discrepancy can be explained by this reported uncertainty.

Thanks to the reliable source of hydrodynamic data and the new method applied for the added mass calculations, the simulations code developed during this thesis study

performs well and simulation results are satisfactory, given that Remus AUV utilized for the Prestero's study is an unstable vehicle. For more precise results, an autopilot similar to the actual vehicle should be provided in the simulation code. When the vitality of the proper simulation method for an autonomous underwater vehicle is considered, the proposed simulation method in this study appears to be a very efficient and practical way.

CHAPTER 5

SUMMARY AND CONCLUSION

In this study, a 6DOF simulation tool is generated for underwater vehicles like AUVs and torpedoes. For the development of the simulation tool, the generation of the hydrodynamic database is generated by using reliable CFD simulation, rather than the analytical correlations, which is common practice in this field. For the calculation of added mass and inertia values, a novel method is developed and utilized.

The developed method is, in fact, the numerical application of an experimental setup used to determine the added mass values of submerged bodies. The theory behind the method relies on the relation between the vibration characteristics of 1DOF system under natural oscillation and their equivalent mass. The added mass values obtained by the developed method are also validated with the experimental data and exact solutions for basic geometries.

The development of the 6DOF simulation tool is performed in Matlab Simulink environment. Since the 6DOF simulation block in the Simulink library is not suitable for the underwater applications, necessary changes are applied on the block in order to have a simulation block suitable with the underwater trajectory simulations. The unit tests were also performed on the simulation tool and promising results are obtained. The trajectory simulations are performed by using Remus AUV geometry, for which the theoretically and experimentally obtained trajectory data is available in the literature [9]. The static CFD computations are done by employing the Fluent CFD tool with a computational grid having about 5 million elements. The dynamic derivatives are obtained by Missile DATCOM semi-empirical tool. The added mass values used in the trajectory simulations are obtained by applying the developed method in FlowVision CFD software with a non-dimensional time step of $\pi/52$.

The trajectory results obtained by the generated simulation tool were compared with the theoretical and experimental data. In some cases,s both the theoretical and numerical trajectory data showed a considerable difference from the experimental data. On the other hand, in some cases the numerically obtained trajectory data was in a very good agreement with the experimental data. However, in all of the trajectory comparisons, it's seen that the trajectory data obtained by the developed tool shows better agreement then the trajectory data obtained by traditional methods as it is applied by Prestero, who is employing a similar method with analytical correlations as hydrodynamic parameters.

It can be concluded from the study that, thanks to the developed numerical method for calculating added mass and the usage of reliable CFD tools, accurate trajectory simulations of an AUV can be performed in a very cost effective and practical way with the developed tool. Especially compared to the usage of the experimental methods for the added mass values, the developed method in this study offers effective and efficient solution with a good accuracy.

5.1 Future work

As a future work, the following improvements are addressed:

- Due to the requirements on the time step size, the damping derivatives of the vehicle have not been calculated. With a higher computing power, the proposed method can also be employed for obtaining the damping coefficients of the vehicle by appropriate sizing of the timescale.
- In this study, the off-diagonal elements of the vehicle have not been found by using the proposed method. A study for obtaining the off-diagonal added masses of the vehicle is addressed.
- For the evaluation of the developed simulation tool, a new set of experimental data with less experimental ambiguity can be generated in a more controlled environment.

REFERENCES

[1] C. H. Houpis, S. N. Sheldon, and J. J. D'azzo, *Linear Control System Analysis and Design: Revised and Expanded*. Crc Press, 2003.

[2] P. B. Donald, "A virtual world for an autonomous underwater vehicle," *Washington: Naval Postgraduate School*, 1994.

[3] J. C. Alexander and J. H. Maddocks, "On the kinematics of wheeled mobile robots," in *Autonomous Robot Vehicles*, pp. 5–24, Springer, 1990.

[4] J. Yuh, "Modeling and control of underwater robotic vehicles," *Ieee Transactions On Systems, Man, and Cybernetics*, vol. 20, no. 6, pp. 1475–1483, 1990.

[5] G. Birkhoff, "Hydrodynamics princeton univ," *Press, Princeton*, 1960.

[6] H. Lamb, *Hydrodynamics*. Cambridge University Press, 1932.

[7] F. H. Imlay, "The complete expressions for added mass of a rigid body moving in an ideal fluid," tech. rep., David Taylor Model Basin Washington Dc, 1961.

[8] J. N. Newman, *Marine Hydrodynamics*. Mit Press, 1977.

[9] T. T. J. Prestero, *Verification Of A Six-Degree Of Freedom Simulation Model For The Remus Autonomous Underwater Vehicle*. PhD thesis, Massachusetts Institute Of Technology, 2001.

[10] J. JournÉE, "Quick strip theory calculations in ship design," *Newcastle Upon Tyne: Sn*, 1992.

[11] R. Blevins, "Formulas for natural frequency and mode shape, 1979," *Kreiger Publ. Comp., New York*.

[12] R. Beck, W. Cummins, J. Dalzell, and W. Webster, "Principles of naval architecture," *Vol. Iii Motions In Waves and Controllability*, 1989.

[13] D. Humphreys and K. Watkinson, "Prediction of acceleration hydrodynamic coefficients for underwater vehicles from geometric parameters," tech. rep., Naval Coastal Systems Lab Panama City Fl, 1978.

[14] S. Arslan, "Su Alti Araclari Icin Yeni Gelistirilen Hidrodinamik Modelleme Yontemleri Kullanilarak Otonom Bir Su Alti Aracinin Hidrodinamik Karakteristiginin Incelenmesi," Master's thesis, Istanbul Teknik Univeritesi, Turkiye, 2013.

[15] M. Gertler, "The dtmb planar-motion-mechanism system," tech. rep., David W Taylor Naval Ship Research and Development Center Bethesda Md Dept Of Hydromechanics, 1967.

[16] E. W. Palmer, "The influence of added mass on the natural vibrations and impulse response of long, thin cylindrical shells," tech. rep., David W Taylor Naval Ship Research and Development Center Bethesda Md, 1970.

[17] D. C. Johnson, "A coning motion apparatus for hydrodynamic model testing in a non-planar cross-flow," tech. rep., Massachusetts Inst Of Tech Cambridge Dept Of Ocean Engineering, 1989.

[18] N. Kimber and K. Scrimshaw, "Hydrodynamic testing of a 3/4 scale autosub model," in *Oceanology International*, vol. 94, Citeseer, 1994.

[19] A. Phillips, M. Furlong, and S. Turnock, "Virtual planar motion mechanism tests of the autonomous underwater vehicle autosub," 2007.

[20] R. Coe and W. Neu, "Virtual planar motion mechanism tests in a cfd environment," in *Virginia Space Grant Consortium Student Research Conference*, 2012.

[21] M. Can, "Numerical Simulation Of Hydrodynamic Planar Motion Mechanism Test For Underwater Vehicles," Master's thesis, Middle East Technical University, Ankara, Turkiye, 2014.

[22] S. Lihua, "Calculation of added mass for underwater vehicles based on fvm," 2016.

[23] a. Cura-Hochbaum, "Virtual pmm tests for manoeuvring prediction," 11 2017.

[24] C. Conca, A. Osses, and J. Planchard, "Added mass and damping in fluid-structure interaction," *Computer Methods In Applied Mechanics and Engineering*, vol. 146, no. 3-4, pp. 387–405, 1997.

[25] L. S. Ping, "Hydrodynamic Coefficients Of Maoneuvring For Small Vessels," Master's thesis, Universiti Teknologi Malaysia, Malaysia, 2004.

[26] Y. Ikeda, T. Katayama, H. Okumura, and Others, "Characteristics of hydrodynamic derivatives in maneuvering equations for super high-speed planing hulls," in *The Tenth International Offshore and Polar Engineering Conference*, International Society Of Offshore and Polar Engineers, 2000.

[27] V. Bertram, "Practical ship hydrodynamics butterworth," 2000.

[28] J.-H. Jeong, J.-H. Han, J. Ok, H.-D. Kim, D.-H. Kim, Y.-K. Shin, and S.-K. Lee, "Prediction of hydrodynamic coefficients for underwater vehicle using rotating arm test," *Journal Of Ocean Engineering and Technology*, vol. 30, no. 1, pp. 25–31, 2016.

[29] S. Chen, M. T. Wambsganss, and J. Jendrzejczyk, "Added mass and damping of a vibrating rod in confined viscous fluids," *Journal Of Applied Mechanics*, vol. 43, no. 2, pp. 325–329, 1976.

[30] J. Planchard and M. I. Zahir, "Natural frequencies of tube bundle in an uncompressible fluid," *Computer Methods In Applied Mechanics and Engineering*, vol. 41, no. 1, pp. 47–68, 1983.

[31] Y. Fu and W. Price, "Interactions between a partially or totally immersed vibrating cantilever plate and the surrounding fluid," *Journal Of Sound and Vibration*, vol. 118, no. 3, pp. 495–513, 1987.

[32] M. Haddara and S. Cao, "A study of the dynamic response of submerged rectangular flat plates," *Marine Structures*, vol. 9, no. 10, pp. 913–933, 1996.

[33] V. Vu, M. Thomas, A. Lakis, and L. Marcouiller, "Effect of added mass on submerged vibrated plates," in *Proceedings Of The 25th Seminar On Machinery Vibration, Canadian Machinery Vibration Association Cmva*, vol. 7, pp. 40–1, 2007.

[34] J. Bavsic and J. Parunov, "Analytical and numerical computation of added mass in ship vibration analysis," *Brodogradnja: Teorija I Praksa Brodogradnje I Pomorske Tehnike*, vol. 64, no. 2, pp. 0–0, 2013.

[35] L. Meirovitch and R. Parker, "Fundamentals of vibrations," *Applied Mechanics Reviews*, vol. 54, p. B100, 2001.

[36] N. C. Groves, T. T. Huang, and M. S. Chang, "Geometric characteristics of darpa (defense advanced research projects agency) suboff models (dtrc model numbers 5470 and 5471)," tech. rep., David Taylor Research Center Bethesda Md Ship Hydromechanics Dept, 1989.

[37] R. F. Roddy, "Investigation of the stability and control characteristics of several configurations of the darpa suboff model (dtrc model 5470) from captive-model experiments," tech. rep., David Taylor Research Center Bethesda Md Ship Hydromechanics Dept, 1990.

[38] D. Jones and D. Clarke, "Simulation of flow past a sphere using the fluent code," tech. rep., Defense Science and Technology Organization Victoria (Australia) Maritime Platforms Div, 2008.

[39] C. E. Wasberg and B. a. P. Reif, "Hydrodynamical simulations in fluent," tech. rep., Tech. Rep., Norwegian Defence Research Establishment (Ffi), Kjeller, Norway, 2010.

[40] M. Nahon, "Determination of undersea vehicle hydrodynamic derivatives using the usaf datcom," in *Oceans'93. Engineering In Harmony With Ocean. Proceedings*, pp. Ii283–Ii288, Ieee, 1993.

APPENDIX A

UNIT TESTS

As stated in Section 2.2, the unit tests are performed for the assessment of the 6DOF motion simulation tool generated in this study. The observed output of the unit tests is the following.

- Net forces on the body
- Net moments on the body
- Velocities in body coordinates
- Velocities in earth coordinates
- The orientation of the body
- The angle of attack and the sideslip angle of the body
- Angular velocities
- Position in earth coordinates

The aim of this section is to test the 6 Degrees Of Freedom Simulation system which is constructed by using Simulink environment of Matlab. The aim of these test is to asses the 6DOF simulation algorithm by using predefined inputs which have expected results, logically.

A.1 Gliding test

This test is planned to see the simulation output of the Remus AUV with the effect of only the gravity and buoyancy. The vehicle CG location is changed in the simulation

such that the locations of the CG and CB coincides with each other. The CG and CB loaction results in the hydrostatic moments to be zero during the simulation. The only effect on the motion is the hydrostatic and hydrodynamic forces. The expected result is a gliding motion which is composed of forward and upright motion. The only non-zero initial condition is the forward velocity of the AUV having a magnitude of 1.54 m/s. The results of the gliding test are given in Figure A.1.1 through Figure A.1.8.

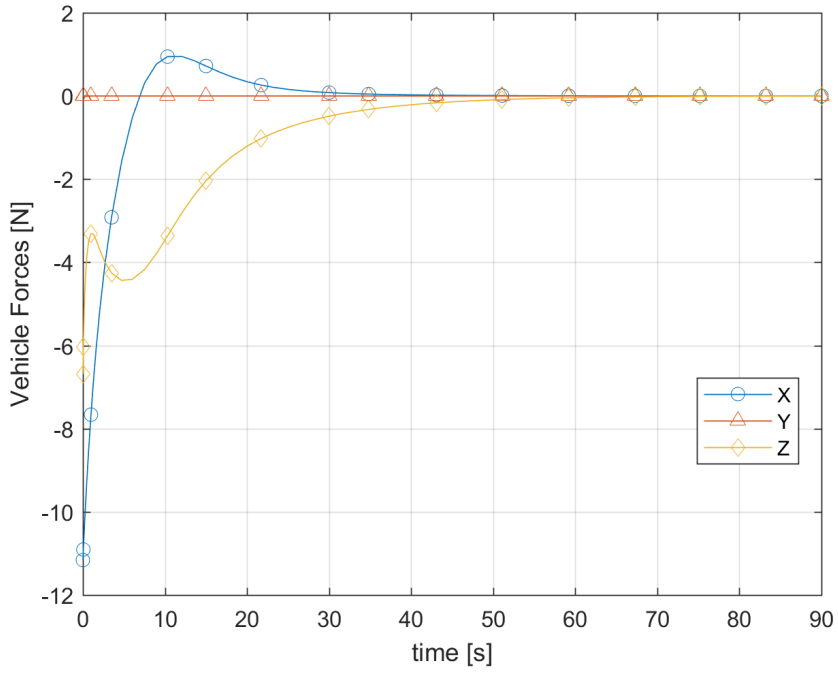

Figure A.1.1: The forces acting on the body in gliding motion

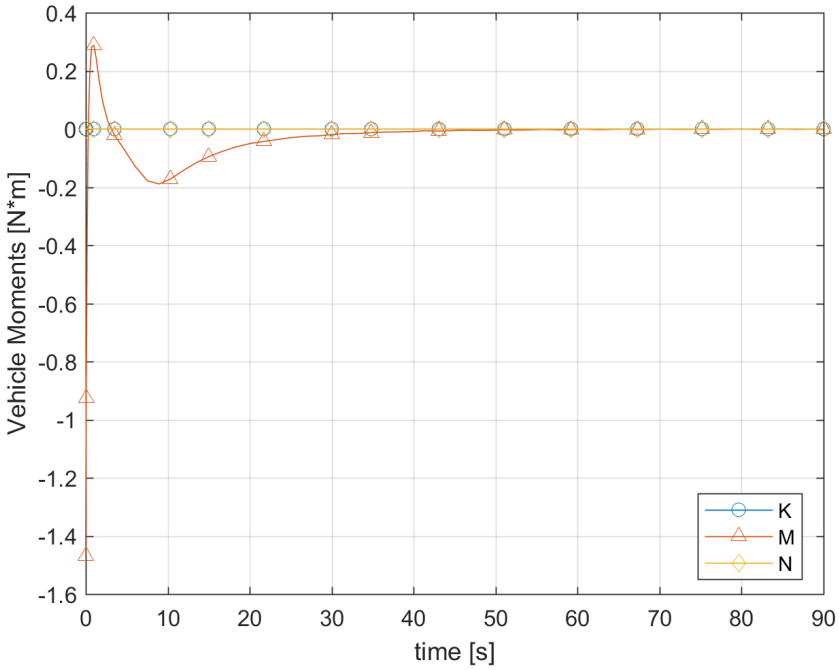

Figure A.1.2: The moments acting on the body in gliding motion

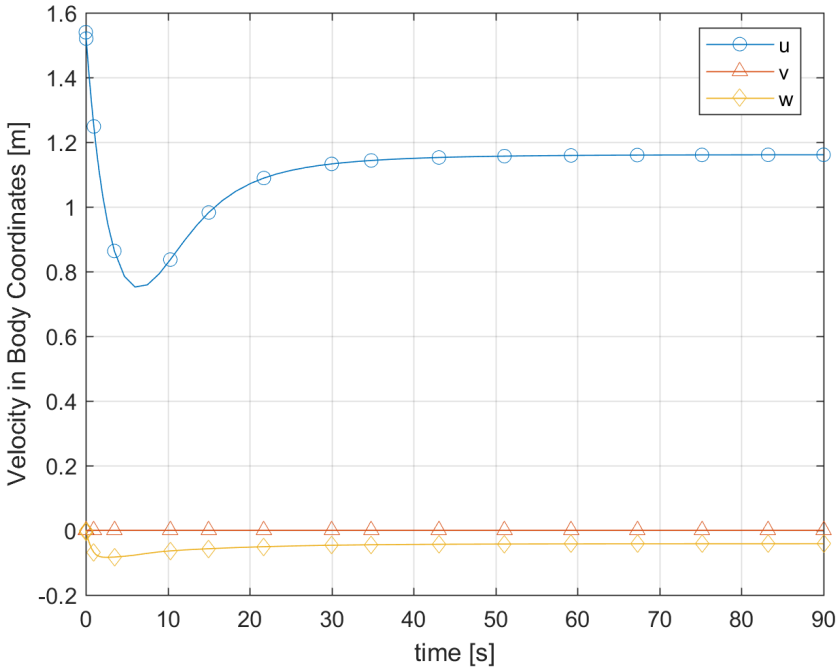

Figure A.1.3: The velocity of the body in body coordinates in gliding motion

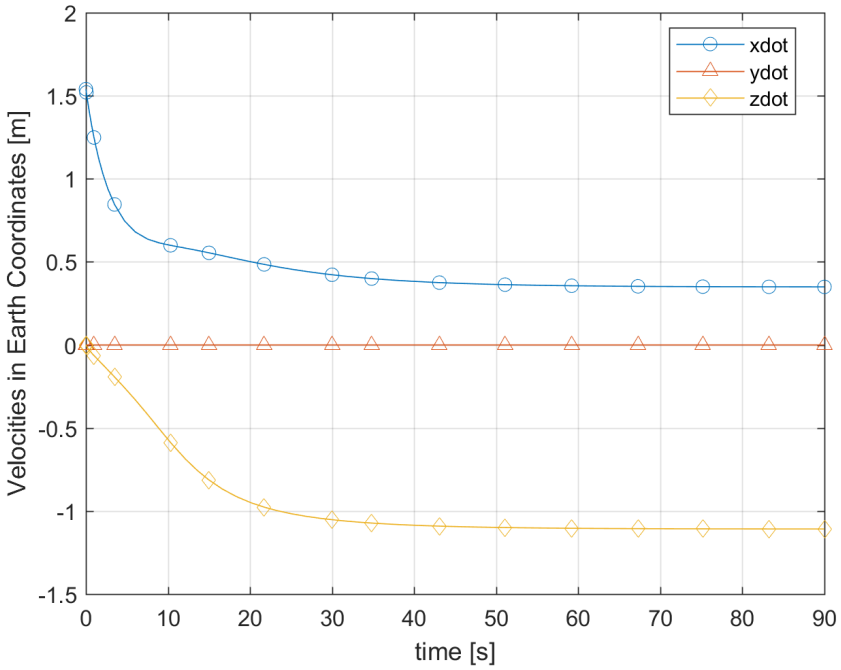

Figure A.1.4: The velocity of the body in earth coordinates in gliding motion

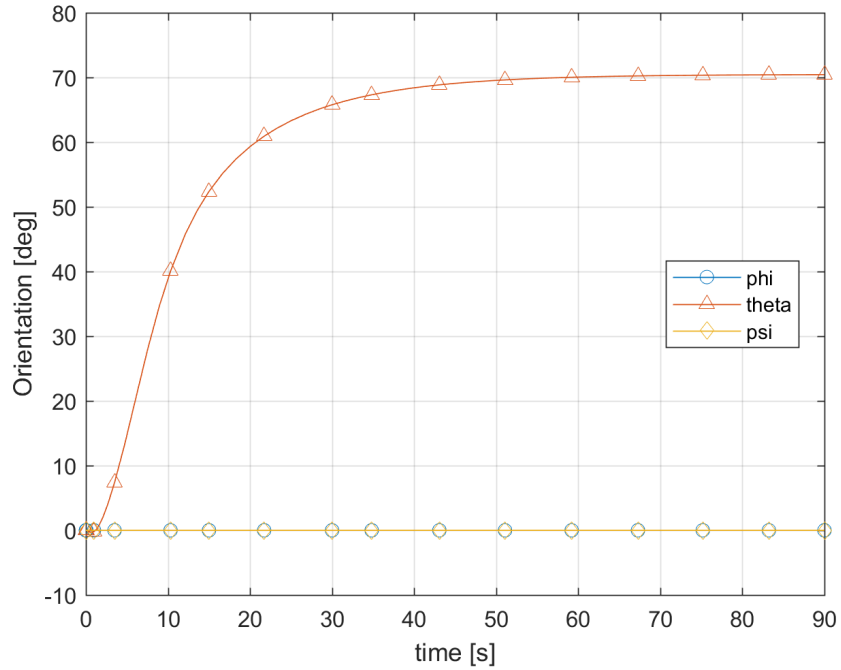

Figure A.1.5: The orientation of the vehicle in gliding motion

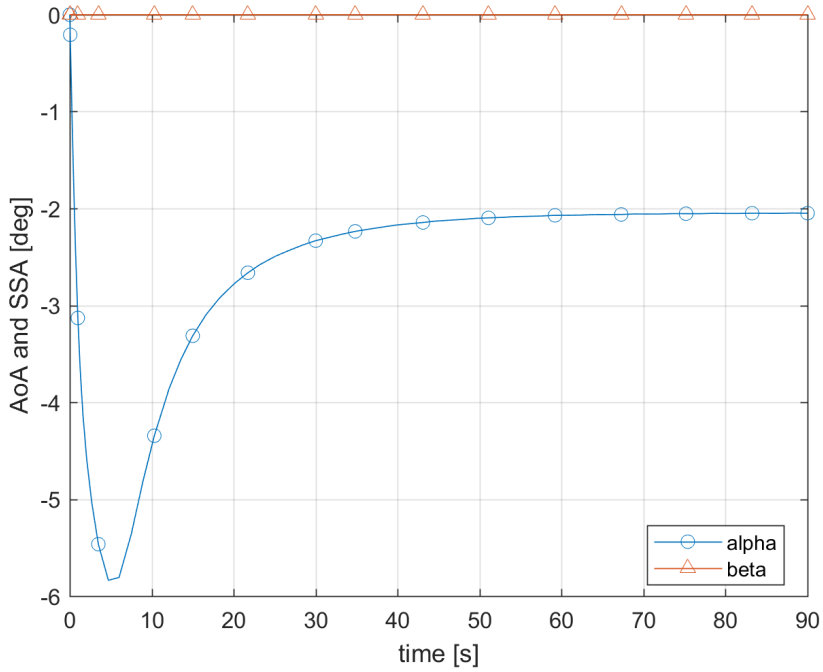

Figure A.1.6: The angles of attack and sideslip of the body in gliding motion

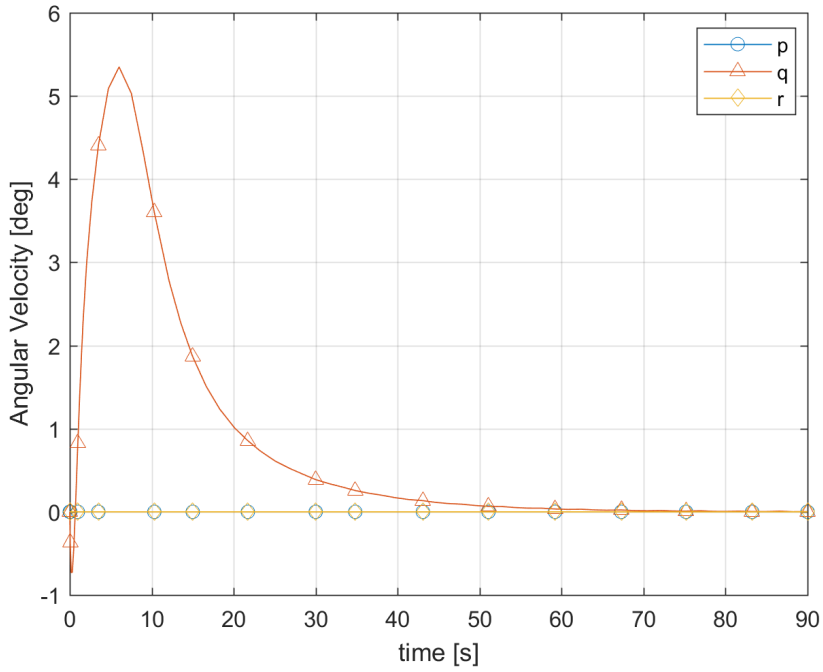

Figure A.1.7: The angular velocities of the body in gliding motion

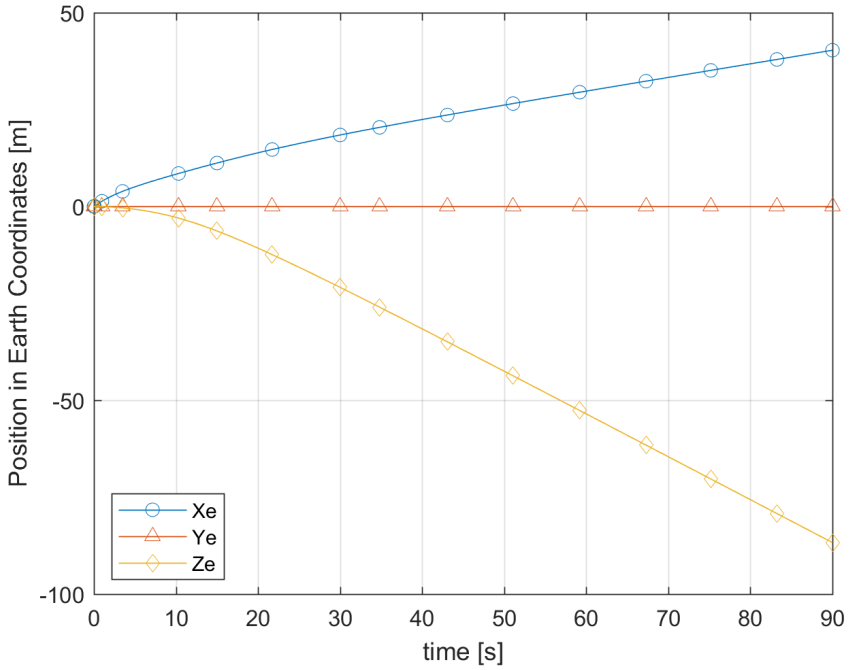

Figure A.1.8: The position of the vehicle in earth coordinates in gliding motion

As a first inspection of the results, it is seen that the angle of attack of the vehicle has reached about -6 degrees, then it starts to decrease and reach about -2 degrees as a final value. It should be noted that this instance of -6 degrees angle of attack corresponds to the time at which forward velocity of the vehicle shown in Figure A.1.3 gets its minimum value throughout the simulation. After that instance, the forward velocity of the vehicle starts to increase due to the buoyancy force and its positive pitch orientation. Additionally, one can say that the forces and moments on the vehicle reach equilibrium at about 30 seconds after starting of the simulation by looking at Figure A.1.1 and Figure A.1.2. Which is also the time at which the vehicle reaches its terminal velocity and final position of gliding. At Figure A.1.5, it is seen that the final pitch orientation of the vehicle is about 70 degrees in nose-up direction. At first, it may seem strange because the hydrostatic moments are zero during the simulation. However, when the vehicle starts to move upward, a positive pitching moment starts to be present which is generated by the horizontal tail fins producing a downward force on the body centered at the aft of CB.

A.2 Gliding test with longitudinal eccentricity

This test is used to asses the output of a 90-second simulation of gliding motion of an eccentrically buoyant model, i.e a buoyant model having a CG located at the aft of the CB. The propeller effects on forward and rolling motion are not taken into account. The motion in this test is driven by only the hydrostatic forces and moments. The initial velocity of the model is given as 1.54 m/s of forward velocity, which is the predefined cruise velocity of Remus AUV. The initial Euler angles and rates are defined as zero. The fin angles of the model are kept constant at zero deflection throughout the simulation. The distance between the CG and the CB is defined as 0.191 m which is the maximum cross-sectional diameter of Remus AUV. The results of the gliding with eccentricity test are given in Figure A.2.1 through Figure A.2.8.

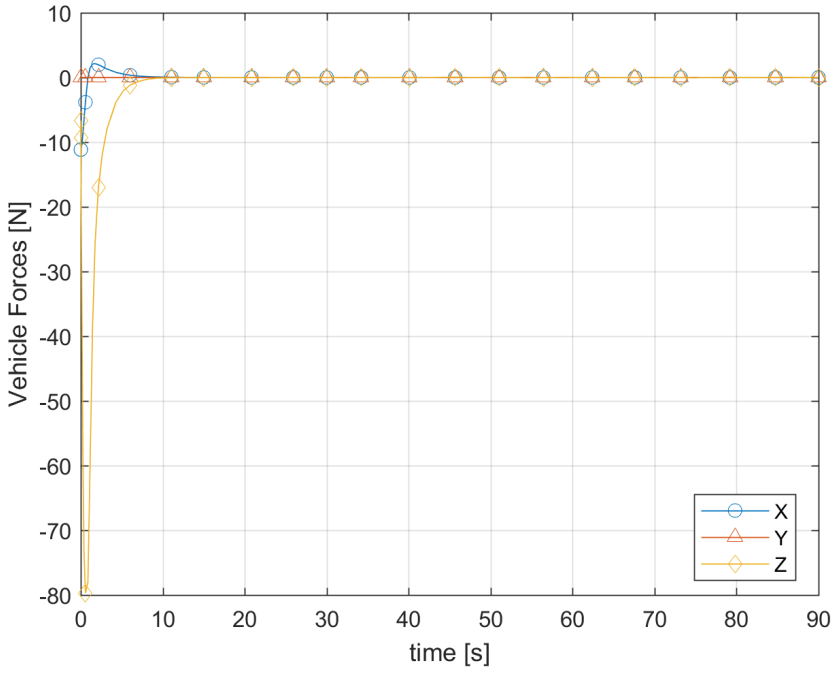

Figure A.2.1: Forces acting on the body in gliding with eccentricity

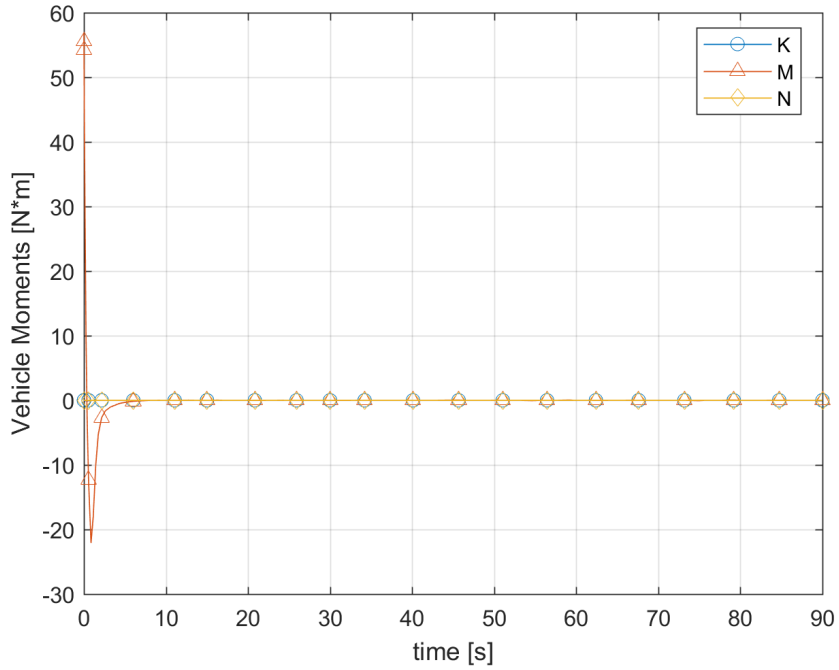

Figure A.2.2: Moments acting on the body in gliding with eccentricity

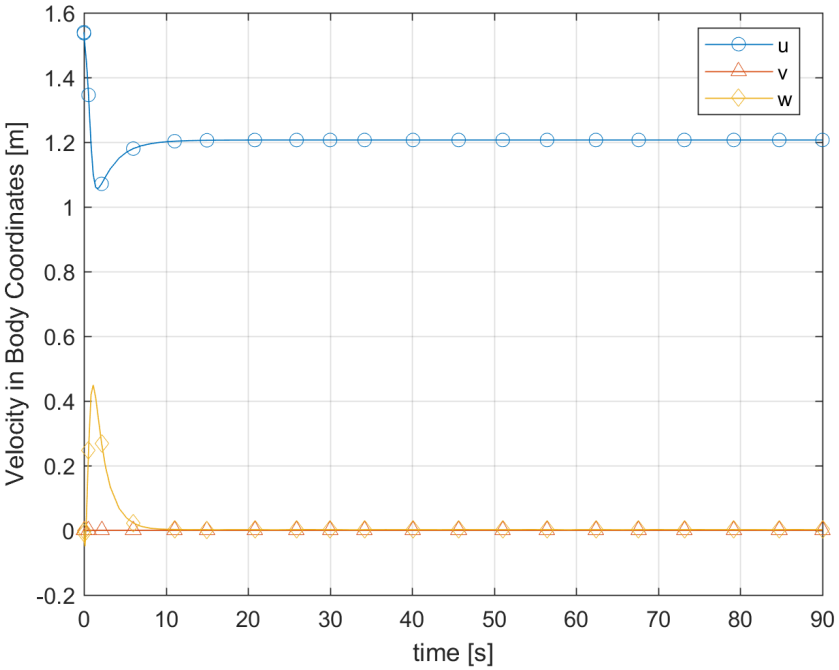

Figure A.2.3: The velocity of the body in body coordinates in gliding with eccentricity

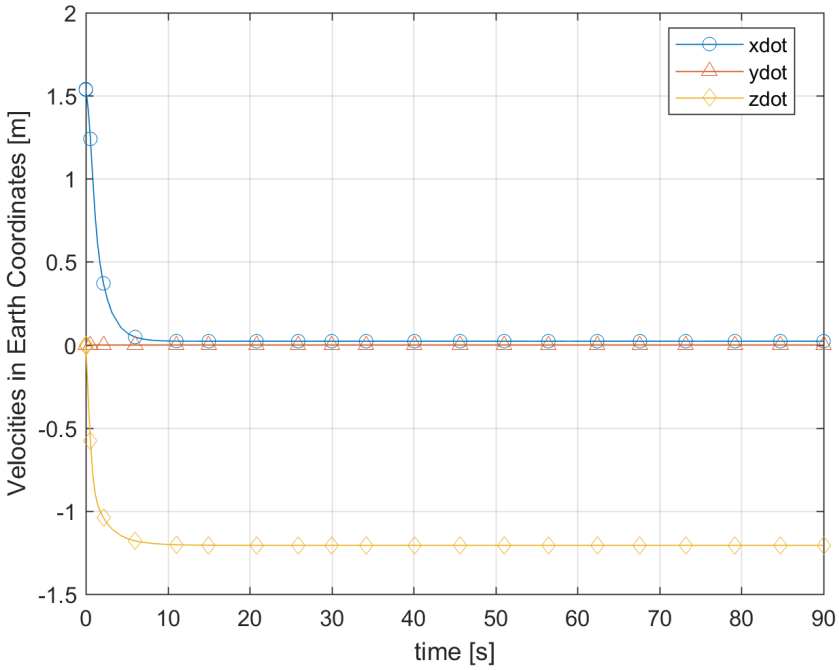

Figure A.2.4: The velocity of the body in earth coordinates in gliding with eccentricity

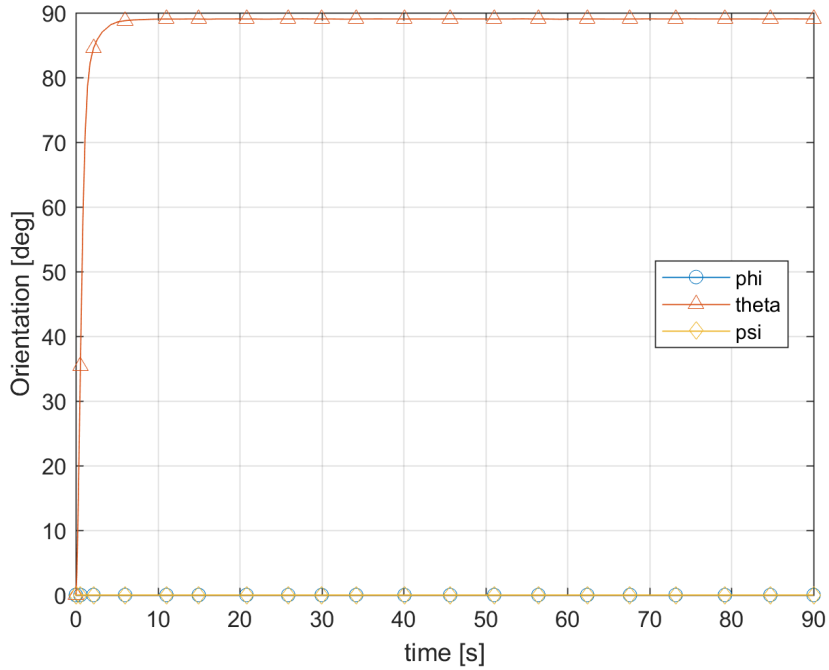

Figure A.2.5: The orientation of the vehicle in gliding with eccentricity

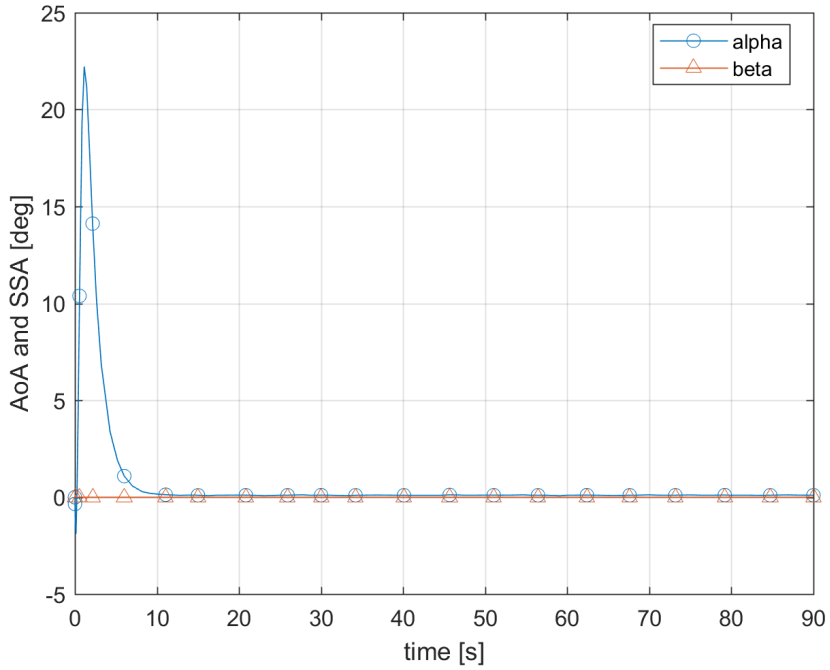

Figure A.2.6: The angles of attack and sideslip of the body in gliding with eccentricity

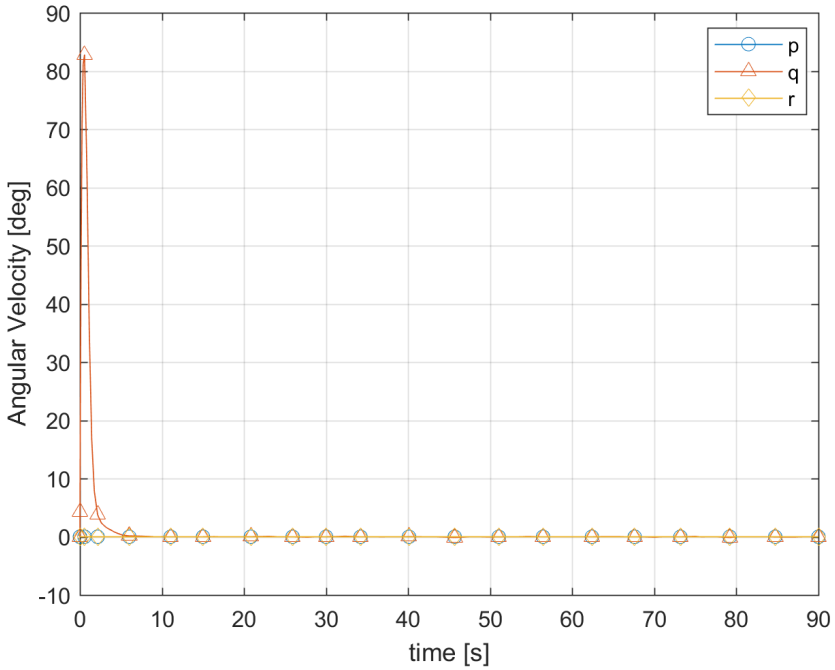

Figure A.2.7: The angular velocities of the body in gliding with eccentricity

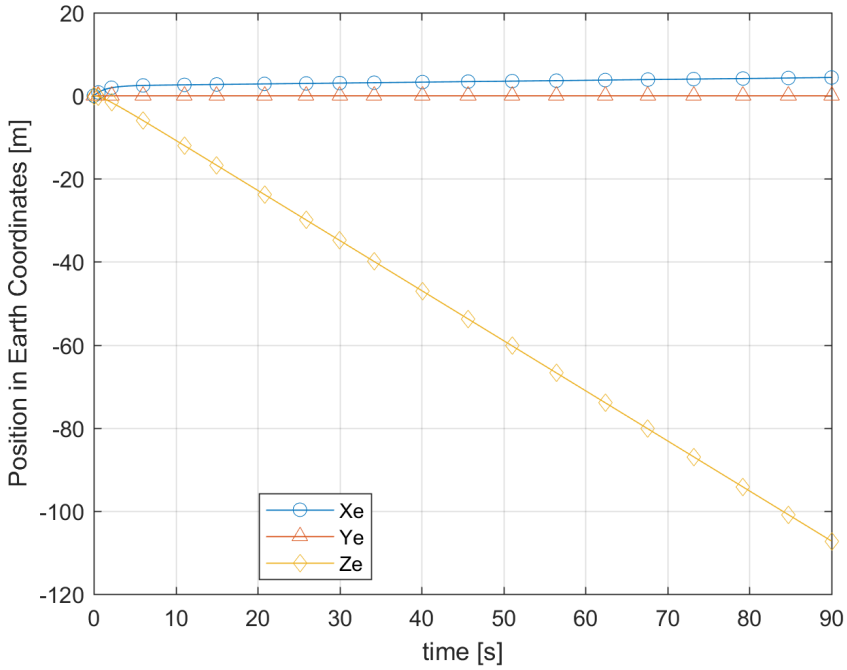

Figure A.2.8: The position of the vehicle in earth coordinates in gliding with eccentricity

As can be seen from Figure A.2.1 and Figure A.2.2, the forces and moments on the body start to diminish and reach nearly zero in the first 10 seconds of the simulation, which means that the vehicle has reached its terminal velocity under these conditions. To better understand, in the Figure A.2.3 and Figure A.2.4 one can observe that the velocities in body and earth frame become nearly constant after 10th second. By looking at the orientation and the angles of attack and sideslip of the vehicle shown in Figure A.2.5, it can be seen that the vehicle has reached an angle of attack of 22 degrees in a very short time, then the angle of attack has decreased to reasonable values. This sudden rise of angle of attack seems a bit strange, however, when the pitch angle change in Figure A.1.5 and the velocities in earth coordinates shown in Figure A.1.4 are analyzed, it can be said that the reason for the sudden rise in angle of attack is due to the pitch up motion of the vehicle while having a positive forward velocity and nearly zero upward velocity. After that sudden pitch, the angle of attack of the vehicle starts to decrease while the vehicle starts to move upward rather than forward. By observing Figure A.2.6 again, one can say that the vehicle pitched up at about 89 degrees which is nearly vertical and the angle of attack and sideslip is

very close to zero. Comparing Figure A.1.5 and Figure A.2.5 it can be seen that the final orientation has become about 20 degrees larger when the hydrostatic moments in favor of pitching up the body is included. The small difference of pitch attitude of the vehicle from 90 degrees can be explained by the vehicle, not being symmetrical in XY plane because of the low-frequency sonar transducer.

A.3 Flip over test

In this test, the effect of the vertical position of the CG on the orientation of the vehicle will be tested. In this test, the vertical location of the CG is defined as -0.0196m which is above the CB. The expected resultant motion is a pitch angle between 90 and 180 degrees. In this test, like the previous ones, the propeller forces and moments are not included and the only non-zero initial condition is the forward velocity of 1.54 m/s. The longitudinal position of the CG coincides with that of the CB. the results of this 90 seconds simulation are given Figure A.3.1 through Figure A.3.8.

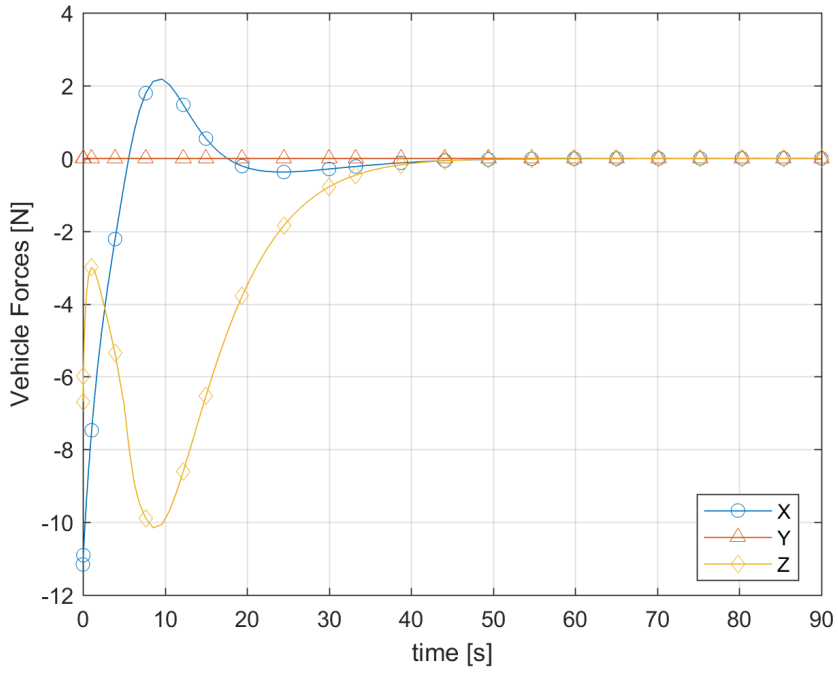

Figure A.3.1: The forces acting on the body during flip over test

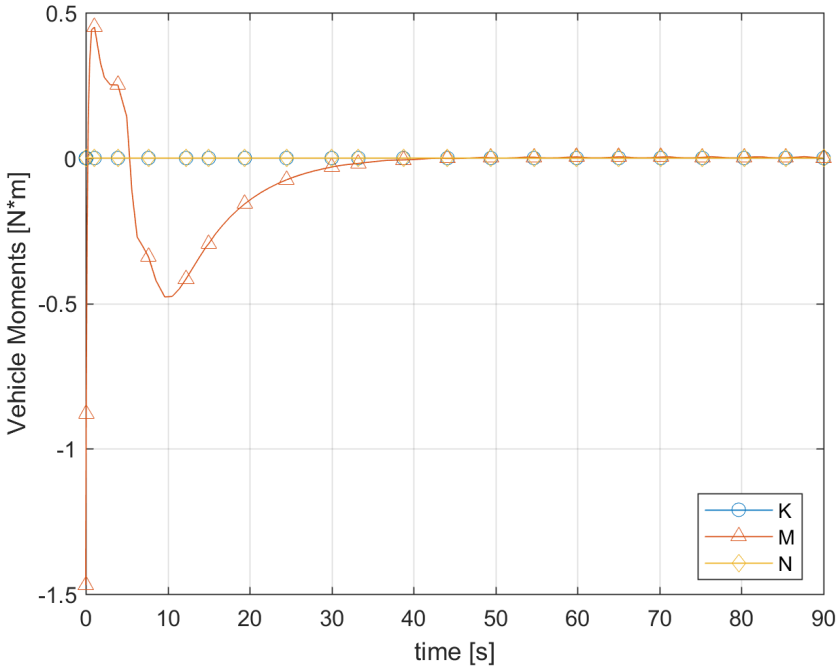

Figure A.3.2: The moments acting on the body during flip over test

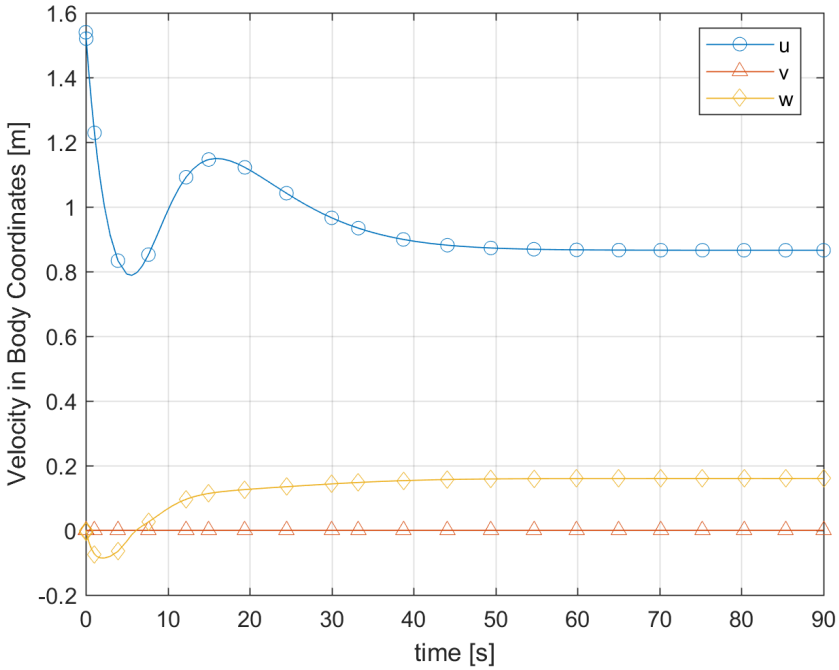

Figure A.3.3: Velocities in body coordinates during flip over test

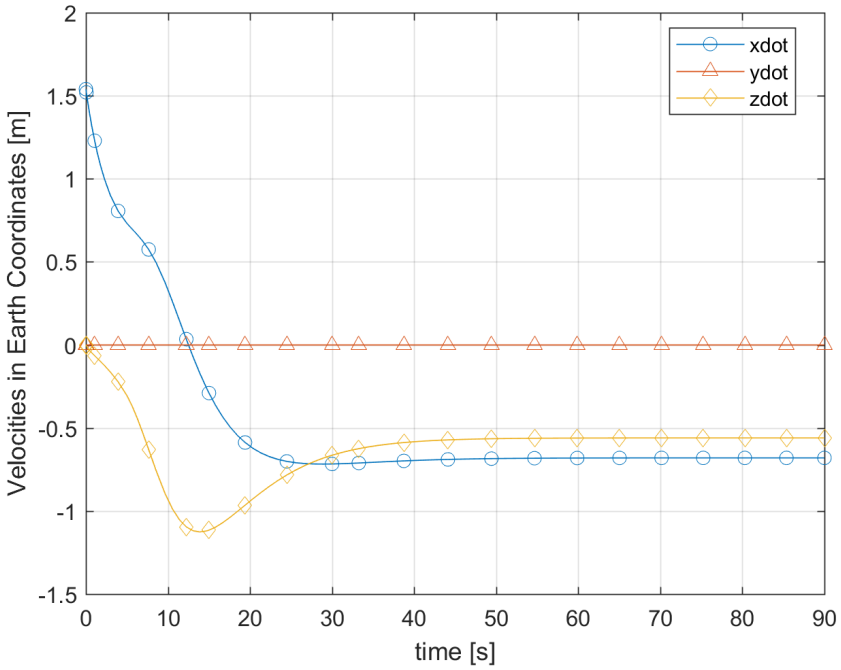

Figure A.3.4: Velocities in earth coordinates during flip over test

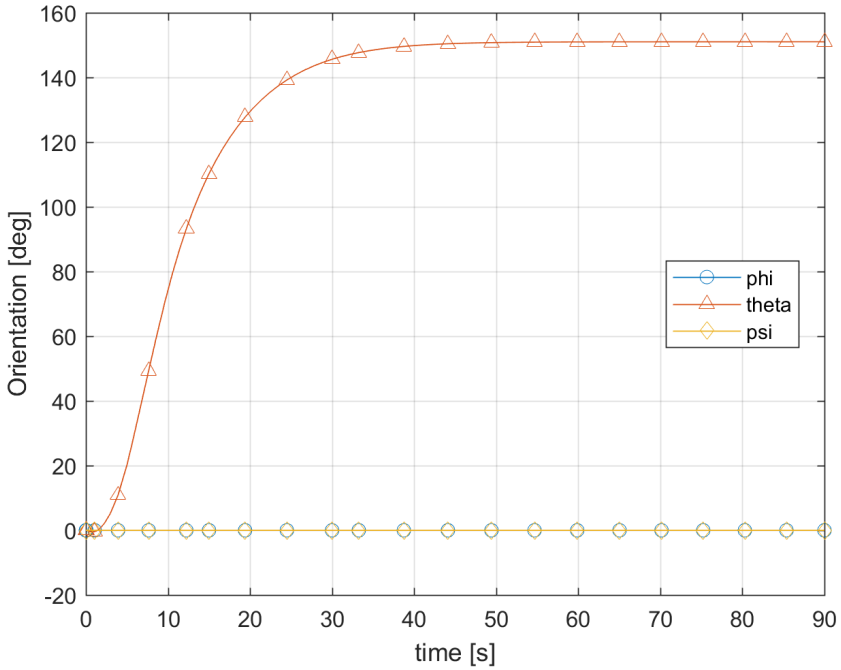

Figure A.3.5: The orientation of the body during flip over test

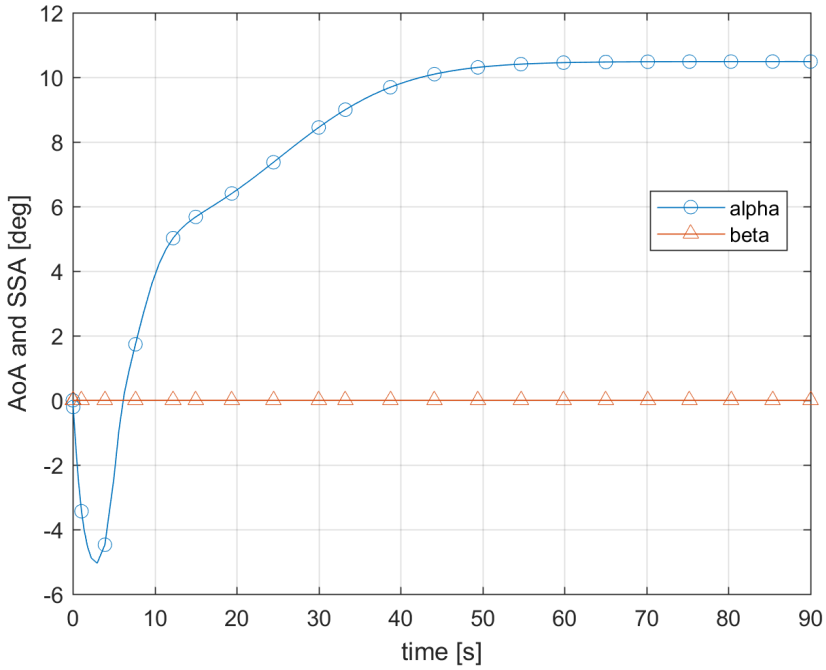

Figure A.3.6: Angles of attack and sideslip during flip over test

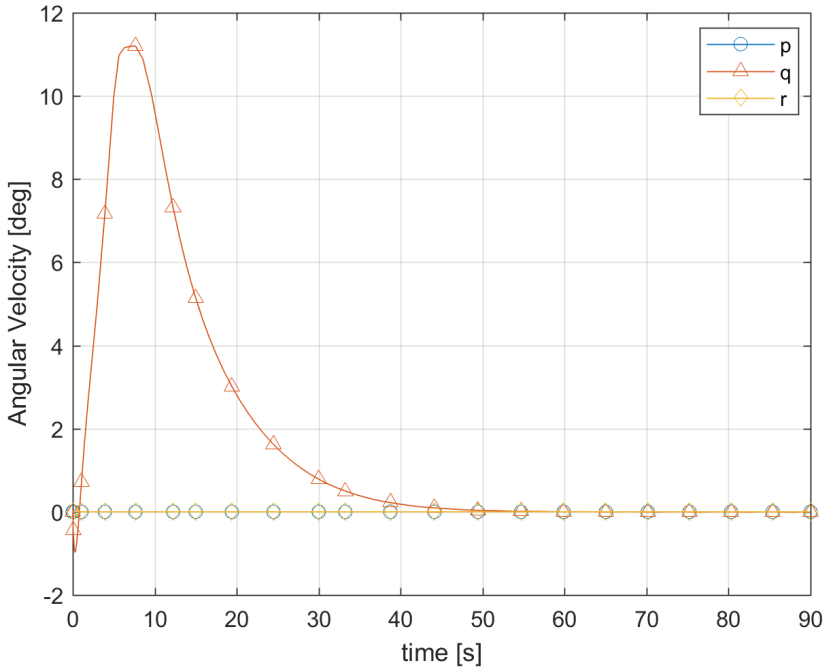

Figure A.3.7: The angular velocities of the body during flip over test

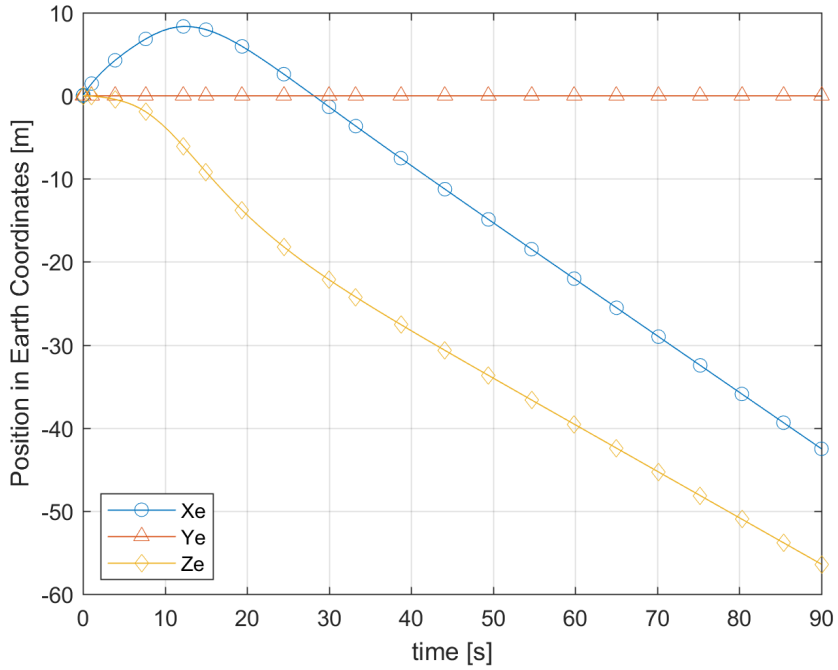

Figure A.3.8: The position of the body during flip over test

In the results, one can observe that the resultant pitch angle of the vehicle is about 150 degrees. This is an expected result, because, the restoring moments are forcing the body to turn "upside-down" and the hydrodynamic moments generated by the horizontal tail fins are resisting to it. The forward motion of the body, represented in body and earth coordinates have opposite signs, which is also a result of the model having a pitch angle much greater than 90 degrees.

A.4 Initial condition tests

A.4.1 Initial velocity test

The aim of this test is to see the effects of initial conditions of the simulation. If the only driving effect is the gravitational and hydrostatic forces, one can expect that the terminal velocities and positions will be the same for different initial conditions. In a properly running simulation tool, the only difference would be the time that the vehicle reaches its equilibrium state. To observe the effects of different initial

conditions, the propeller torques and forces are not taken into account. The forward and downward velocities in body axes, pitch orientations and angles of attack will be compared for three different initial velocities as 1.54 m/s, 5 m/s and 10 m/s. The other initial conditions are set to zero. The simulation time is set to 90 seconds in order to ensure that the vehicle reaches equilibrium position for all three initial velocities. The results can be seen in Figure A.4.1 through Figure A.4.3.

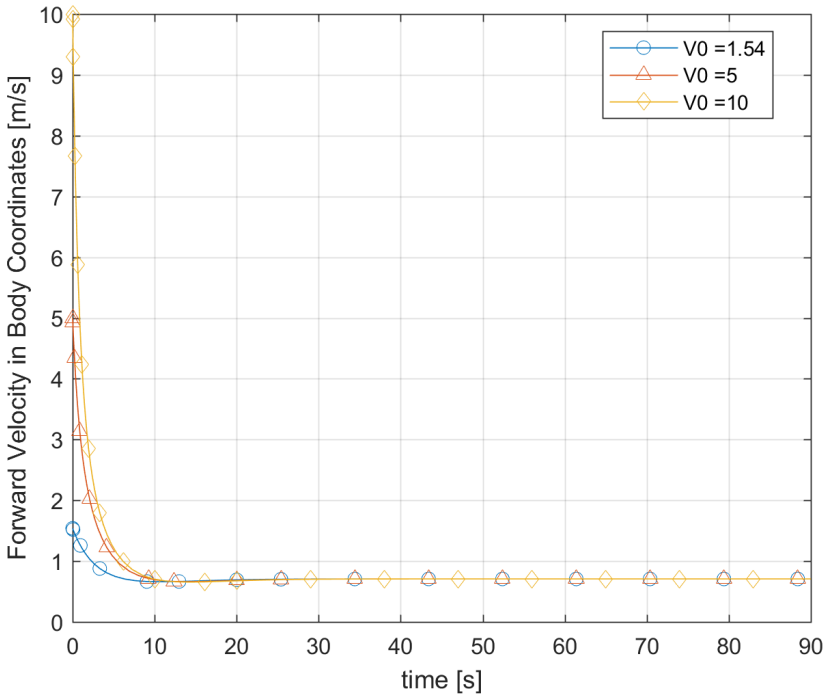

Figure A.4.1: Forward velocities of the body for three initial velocities

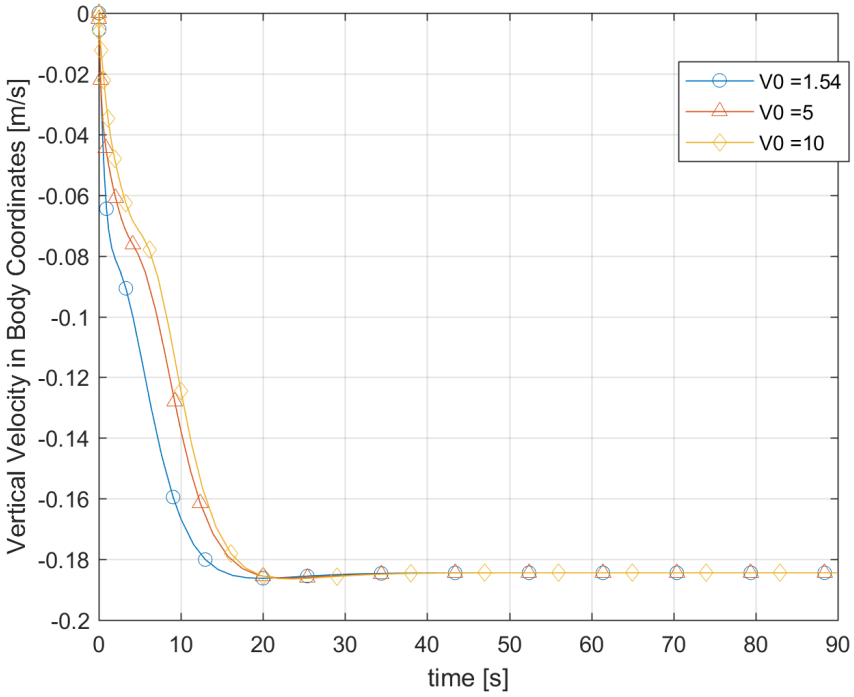

Figure A.4.2: Downward velocities of the body for three initial velocities

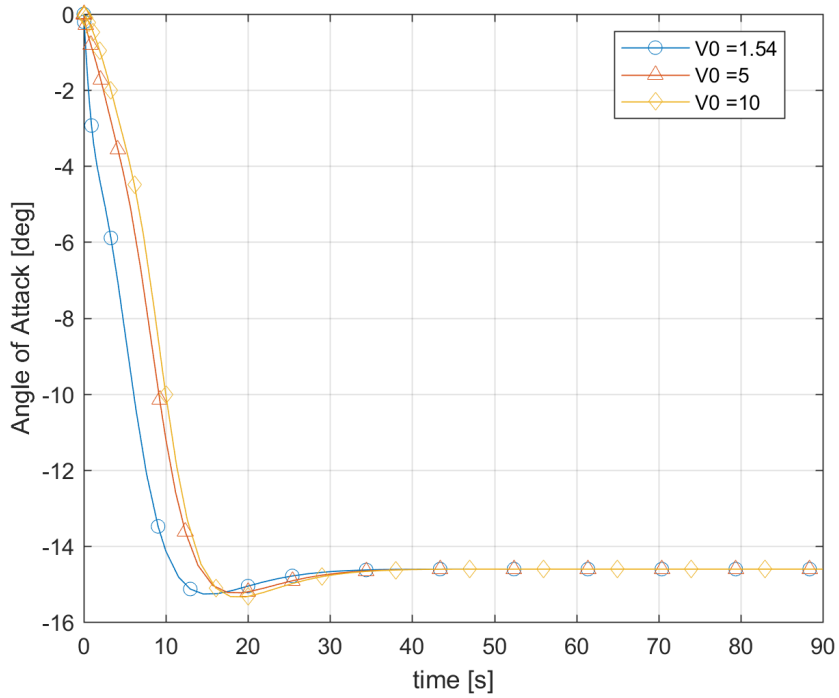

Figure A.4.3: Angles of attack of the body for three initial velocities

As can be seen from the figures, the final condition of the vehicle is not affected by the initial condition. However, the time required to reach the final condition is changing with the change of initial velocity. The results are similar to the expected results.

A.4.2 Initial orientation test

In this test, the effect of initial orientation of the vehicle to the final attitude and velocities of the vehicle is tested. The expected result is again having the same final conditions. In order not the complicate the results, the propeller torque is not included in the simulation. Propeller force of 9.25 N and initial velocity of 1.54 m/s is defined. Three initial pitch angles were tested. First, 0 degrees, then -30 and 30 degrees are tested. The forward and backward velocities, pitch angle and angle of attack change with time are shown in Figure A.4.4 through Figure A.4.7.

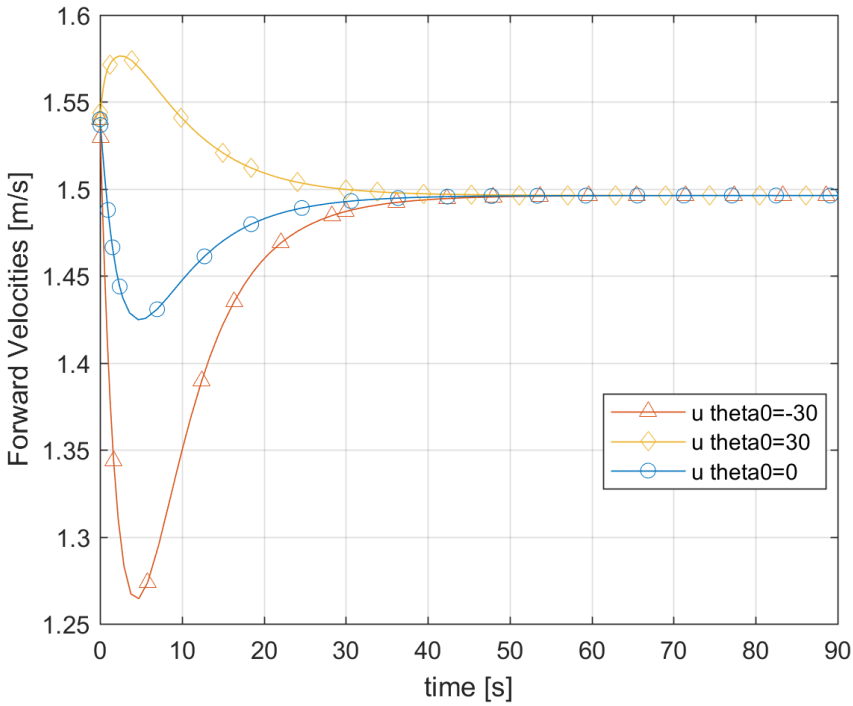

Figure A.4.4: Forward velocities during initial orientation test

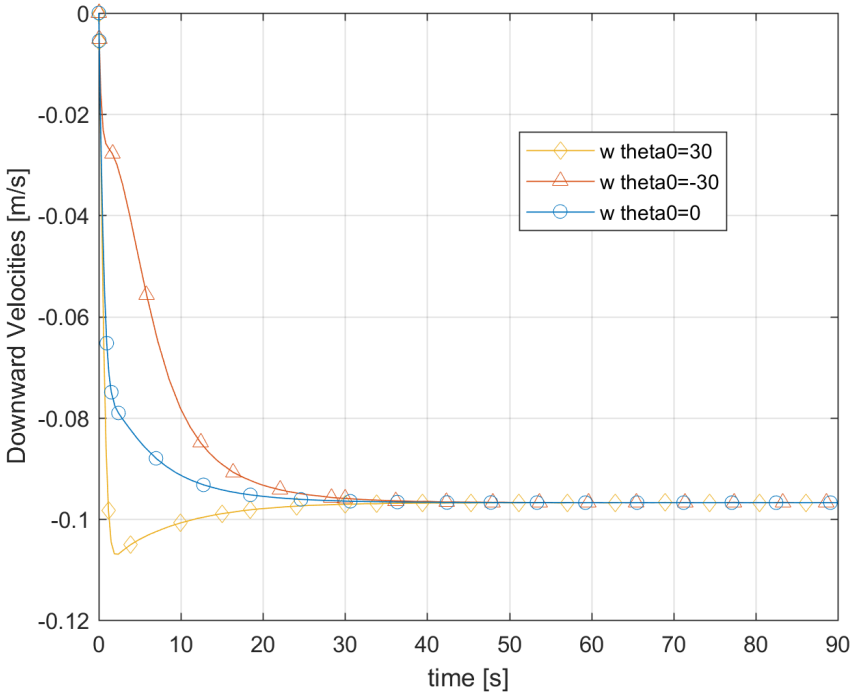

Figure A.4.5: Downward velocities during initial condition test

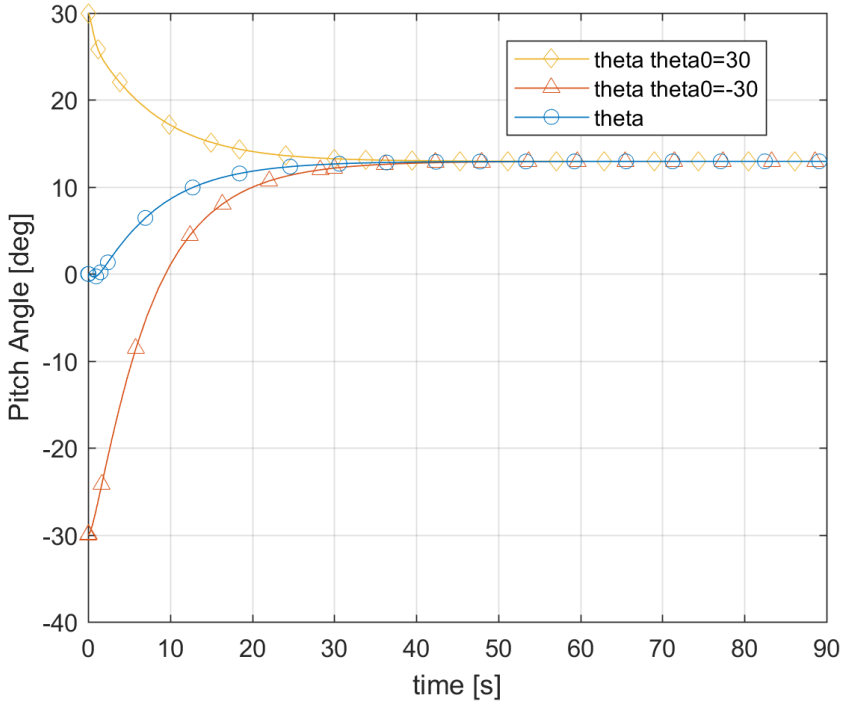

Figure A.4.6: Pitch orientation during initial orientation test

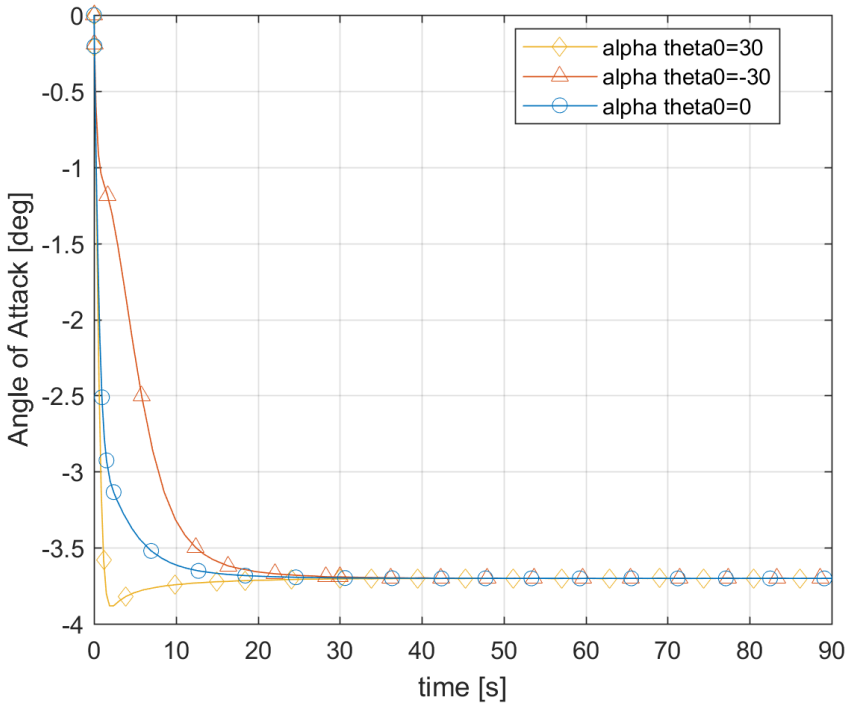

Figure A.4.7: Angle of attack during initial orientation test

First, it can be said that the final orientations and velocities are the same for three initial orientations. The final pitch orientation seems to have a value near 15 degrees, which is an acceptable value when the effect of the propeller is considered. On the other hand, the highest magnitude of the angle of attack is seen at $theta_0 = 30$ degrees condition, this is also an expected result. Because, when the pitch is higher than its final value in that condition. This makes the vehicle have more angle of attack than the other cases.

A.5 Angle of attack control tests

In this section, the angle of attack of Remus AUV is controlled by the autopilot code generated on MATLAB by the author. In all of the angle of attack control cases, the CG of the vehicle is set at 0.0196m below the CB.

A.5.1 Zero angle of attack test

At this part, trimming the vehicle at zero angle of attack is aimed. The angle of attack gain of the controller is set as 2000, in order to decrease the difference between final and desired values of angle of attack. The propeller thrust is defined as 9.25 N and the propeller torque of -0.543 Nm is defined. The initial roll angle is set to -5 degrees in order to balance the propeller torque by hydrostatic means. The results of the simulation are given in Figure A.5.1 through Figure A.5.9.

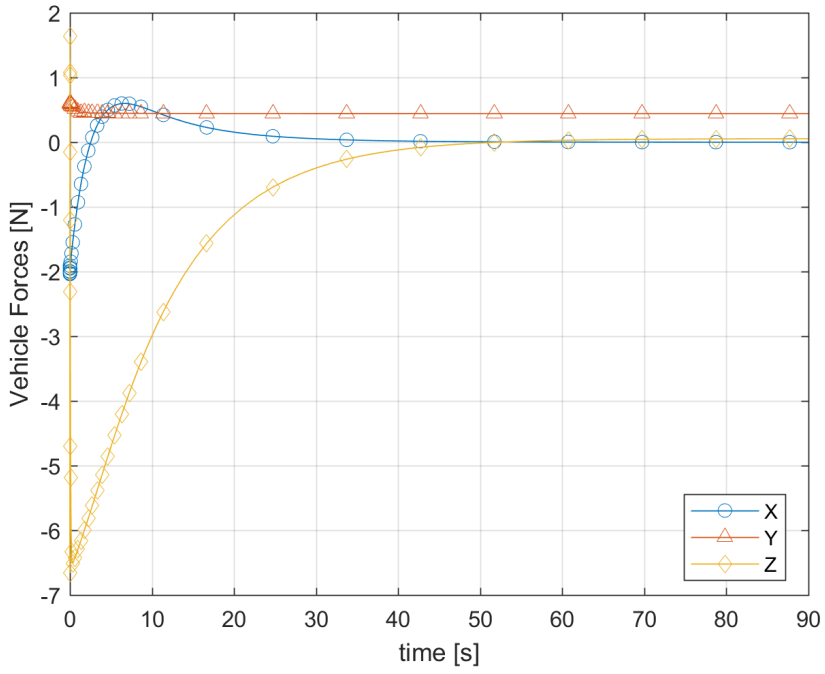

Figure A.5.1: The forces acting on the body during zero angle of attack test

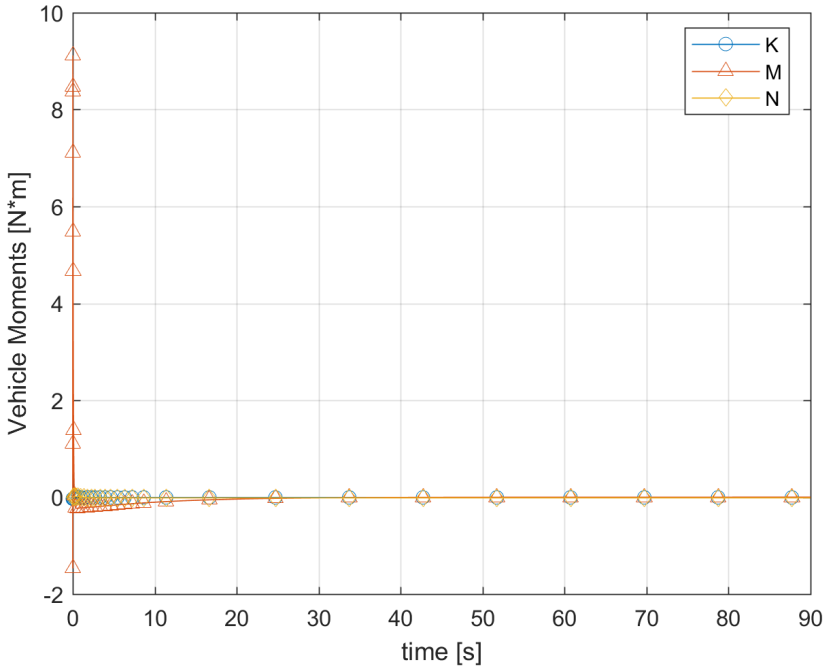

Figure A.5.2: The moments acting on the body during zero angle of attack test

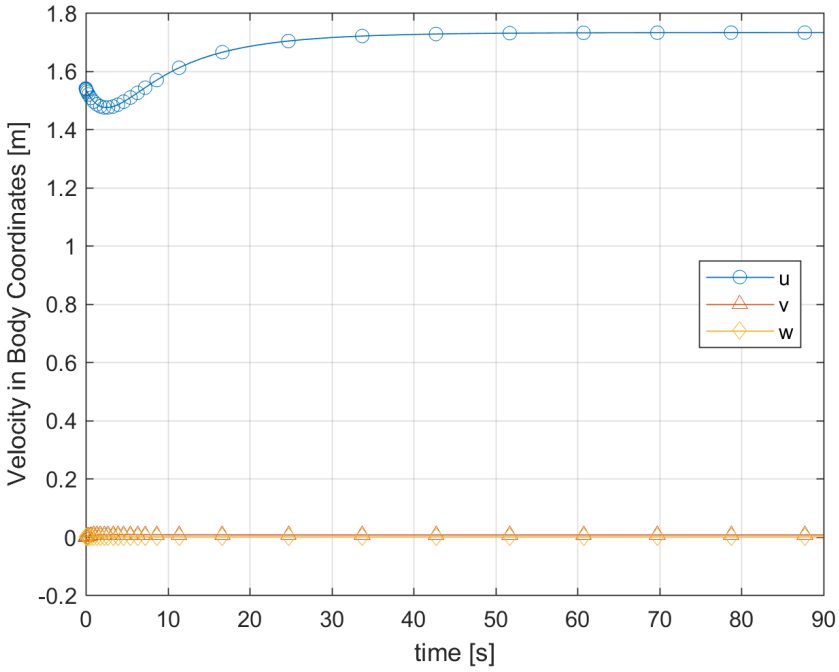

Figure A.5.3: The velocity in body coordinates during zero angle of attack test

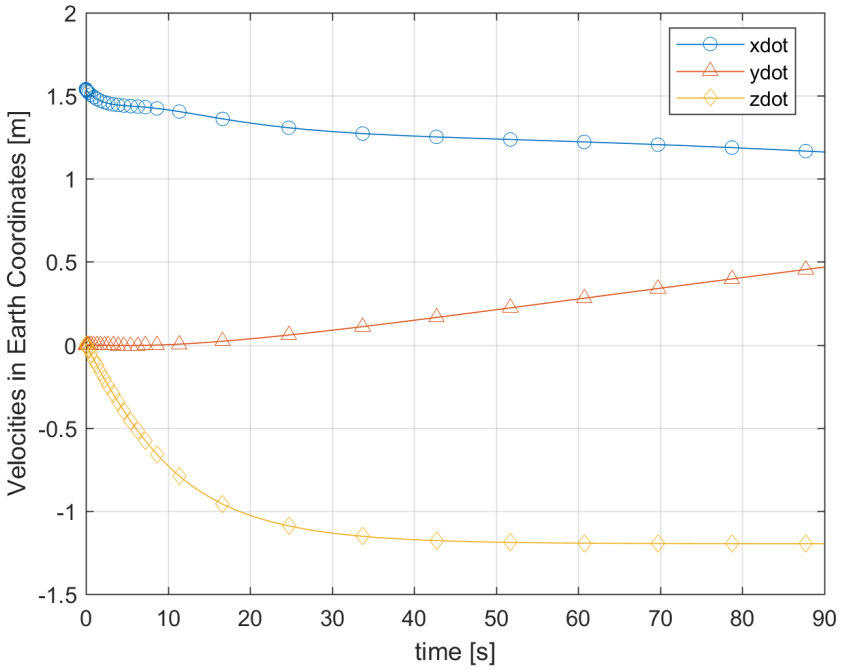

Figure A.5.4: The velocities in earth coordinates during zero angle of attack test

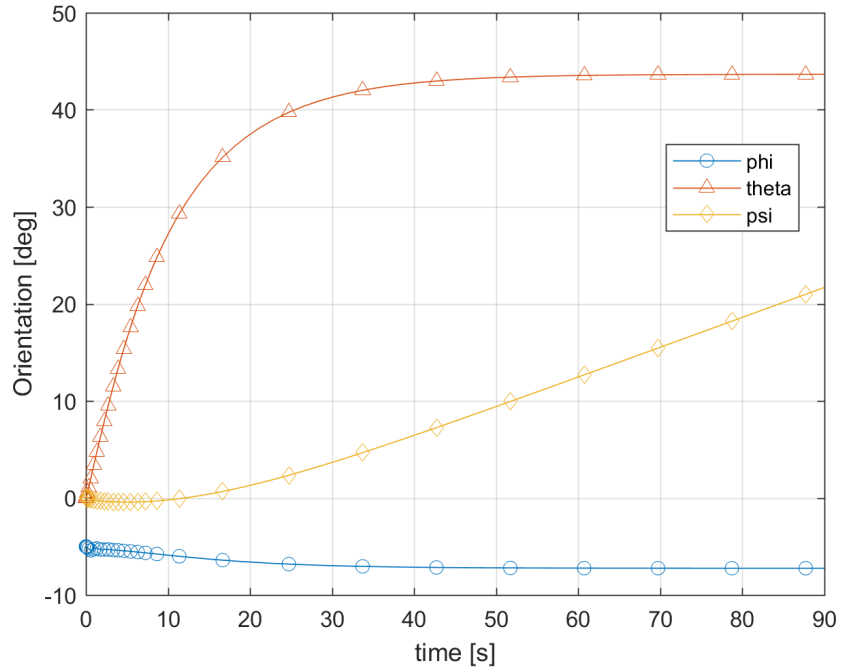

Figure A.5.5: The orientation of the body during zero angle of attack test

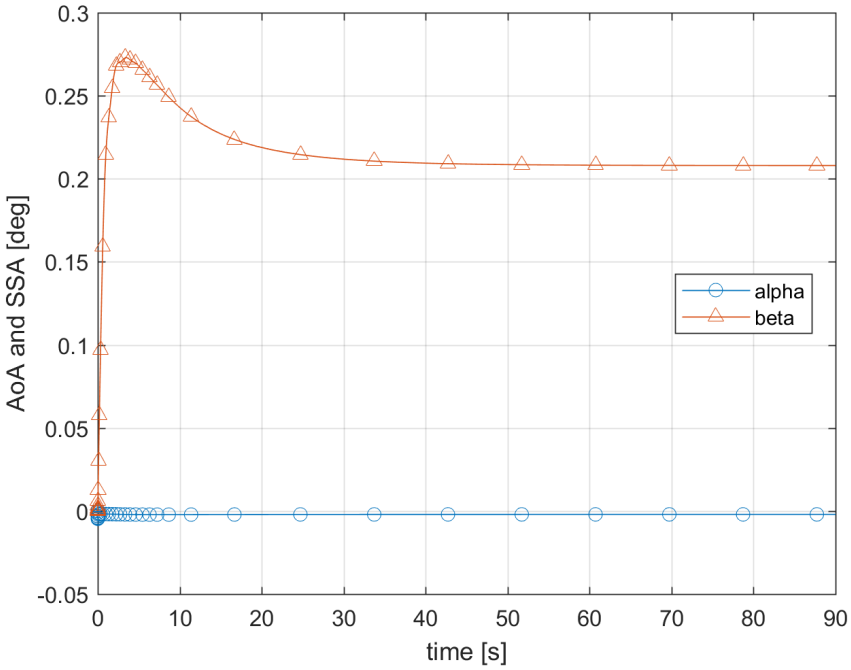

Figure A.5.6: Angles of attack and sideslip during zero angle of attack test

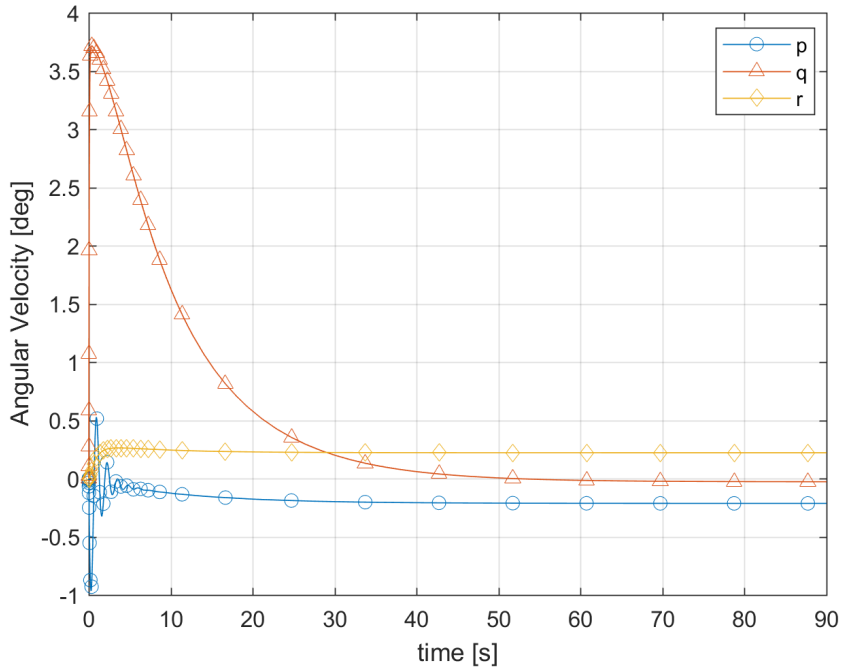

Figure A.5.7: The angular velocities of the body during zero angle of attack test

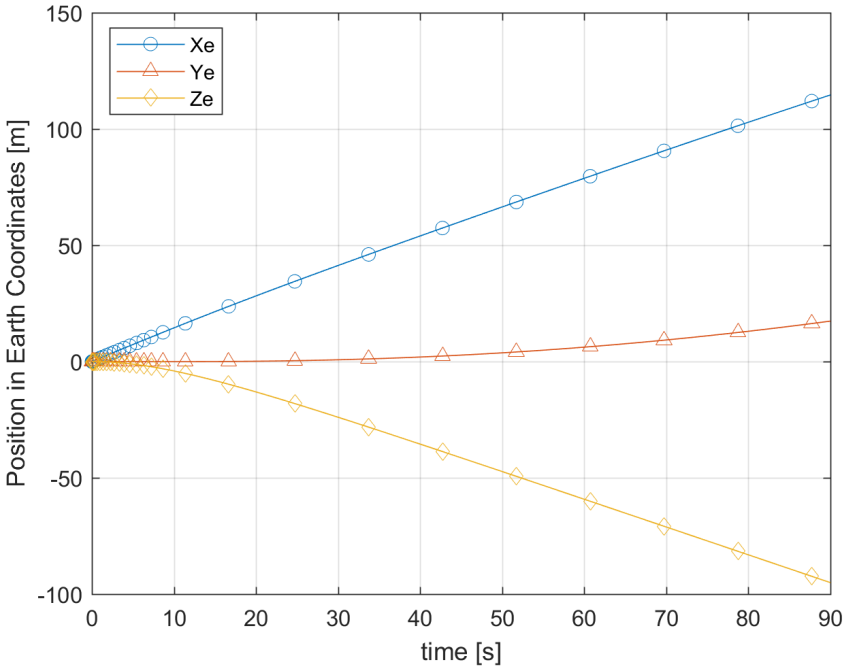

Figure A.5.8: The position of the vehicle in earth coordinates during zero angle of attack test

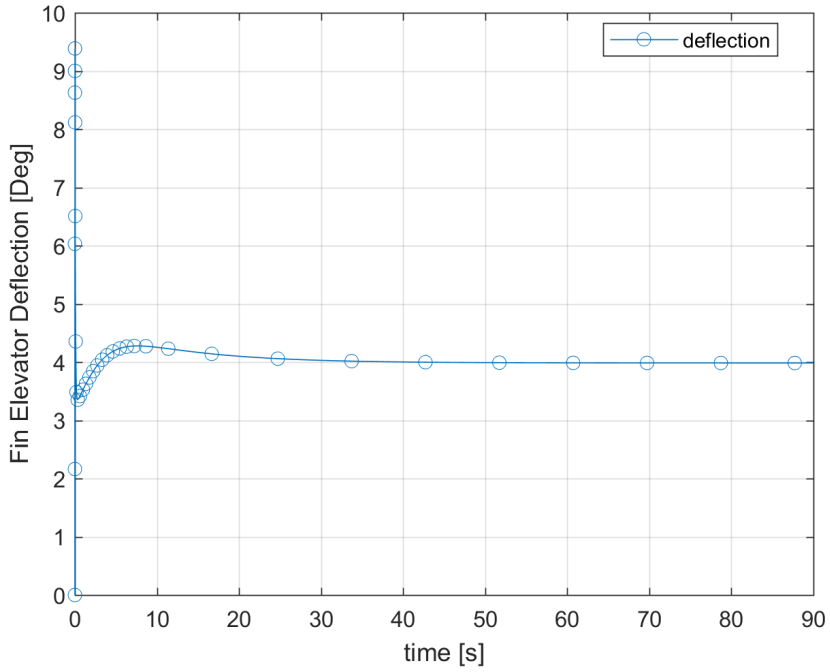

Figure A.5.9: The elevator deflection of the tail fins during eero angle of attack test

As can be seen from Figure A.5.9, the deflection of the tail fins first start at about 9 degrees, in order to neutralize the negative angle of attack started to develop at very first instances of the simulation. The development of that negative angle of attack is due to the w velocity of the vehicle starting to have a negative value because of positive buoyancy. At the final position, the angle of attack of the vehicle is balanced at a value very close to 0 degrees with the tail fins having an elevator deflection of about positive 4 degrees.

A.5.2 Positive angle of attack test

In this test, propeller torque is not included in the calculations and the initial orientation of the vehicle is set as zero. At the results, it is expected to not to see any yaw behaviors. The results of the simulation are presented in Figure A.5.10 through Figure A.5.18 .

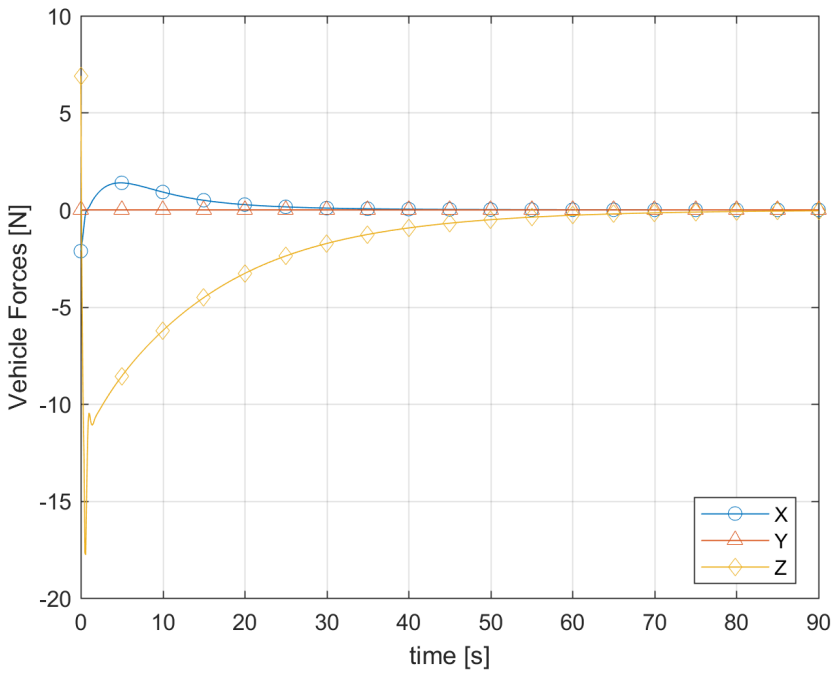

Figure A.5.10: Forces Acting On The Body During Positive Angle of Attack Test Without Propeller Torque

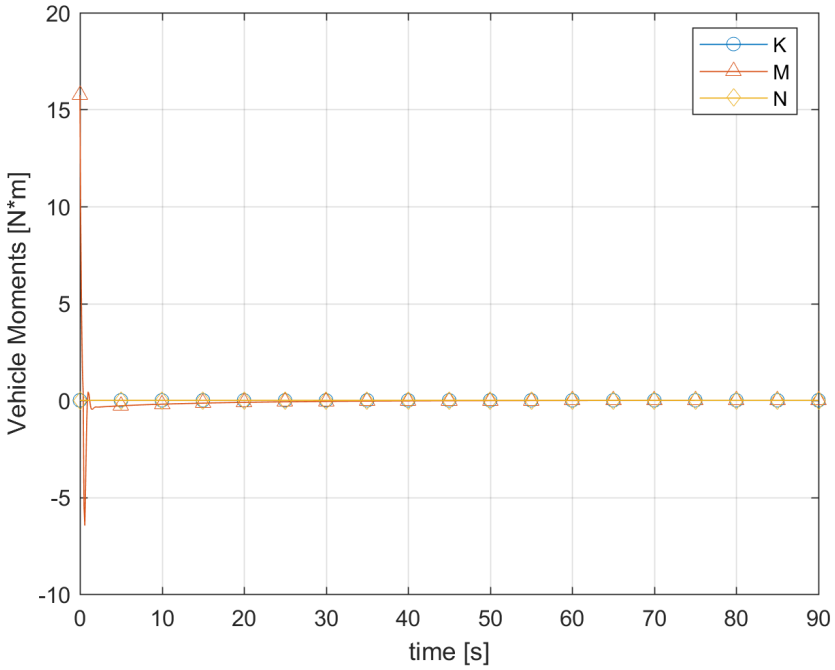

Figure A.5.11: Moments Acting On The Body During Positive Angle Of Attack Test Without Propeller Torque

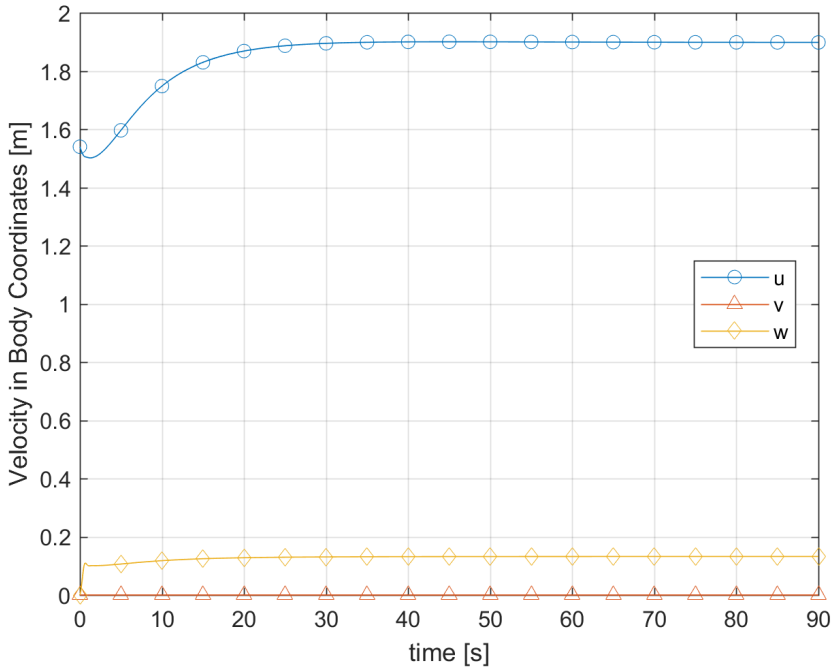

Figure A.5.12: Velocities in Body Coordinates During Positive Angle of Attack Test Without Propeller Torque

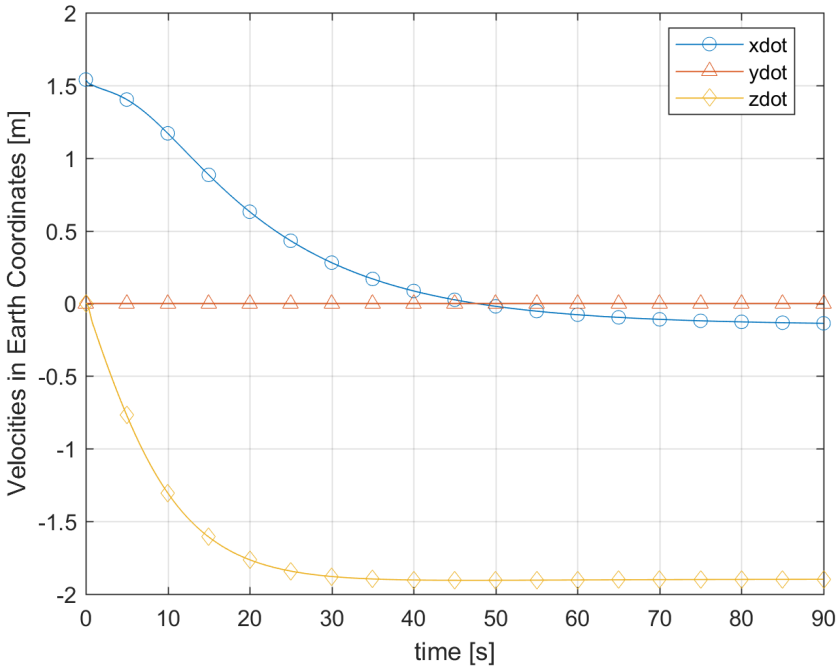

Figure A.5.13: Velocities in Earth Coordinates During Positive Angle of Attack Test Without Propeller Torque

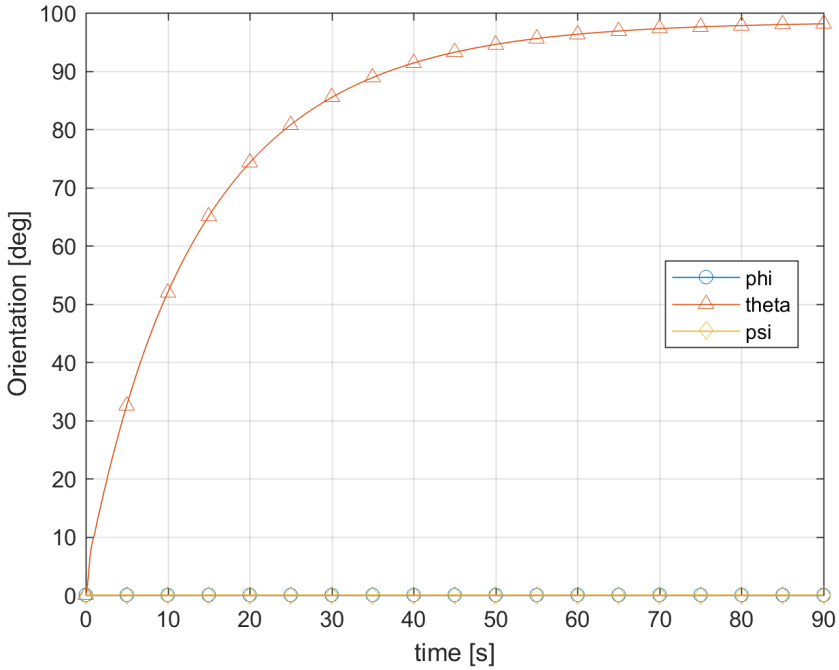

Figure A.5.14: Orientation of The Body During Positive Angle of Attack Test Without Propeller

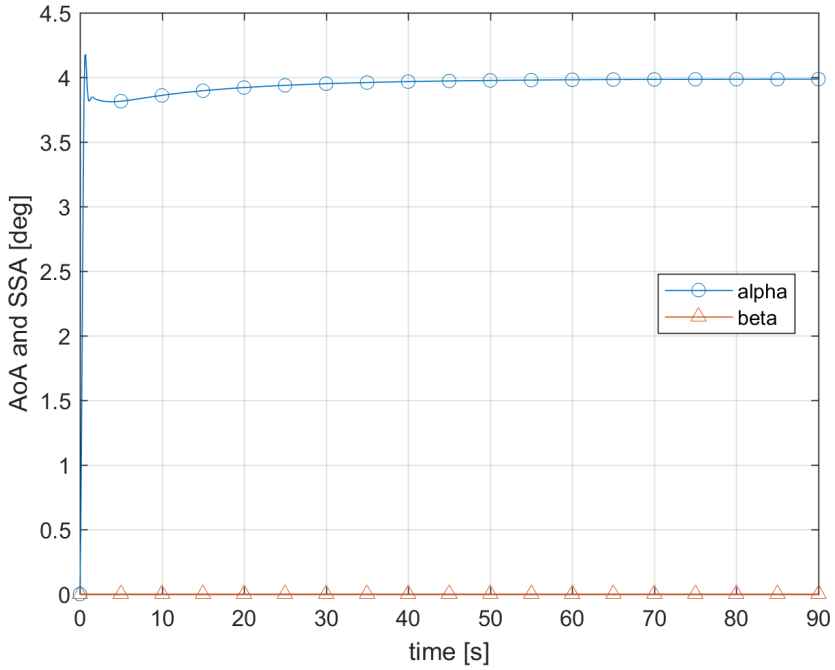

Figure A.5.15: Angles of Attack and Sideslip During Positive Angle of Attack Test Without Propeller Torque

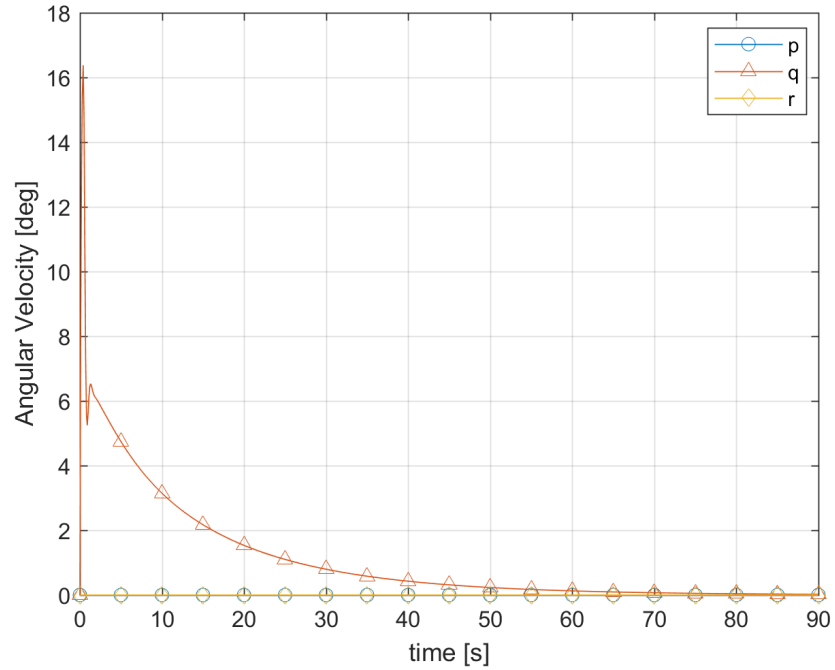

Figure A.5.16: Angular Velocities of The Vehicle During Positive Angle of Attack Test Without Propeller Torque

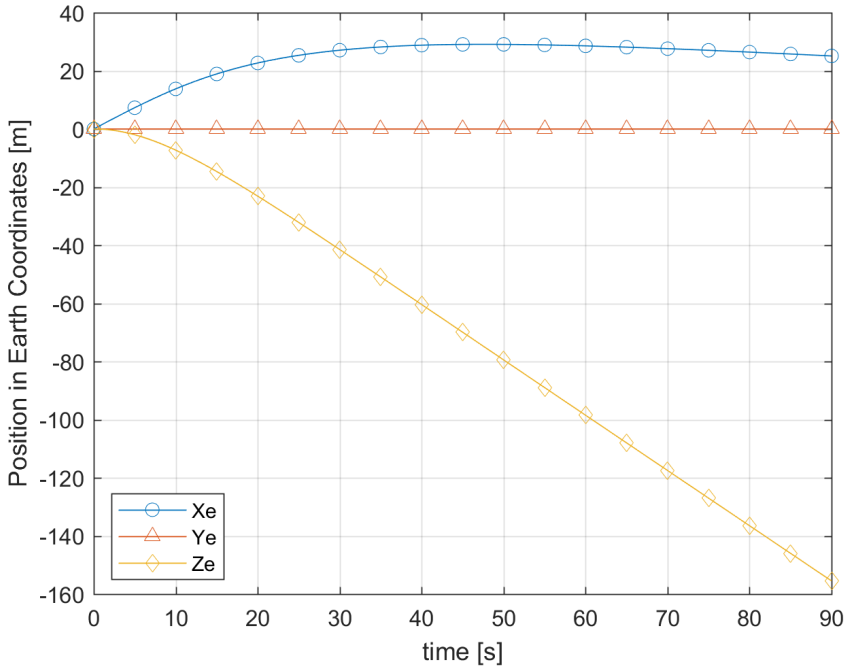

Figure A.5.17: Position of The Vehicle in Earth Coordinates During Positive Angle of Attack Test Without Propeller Torque

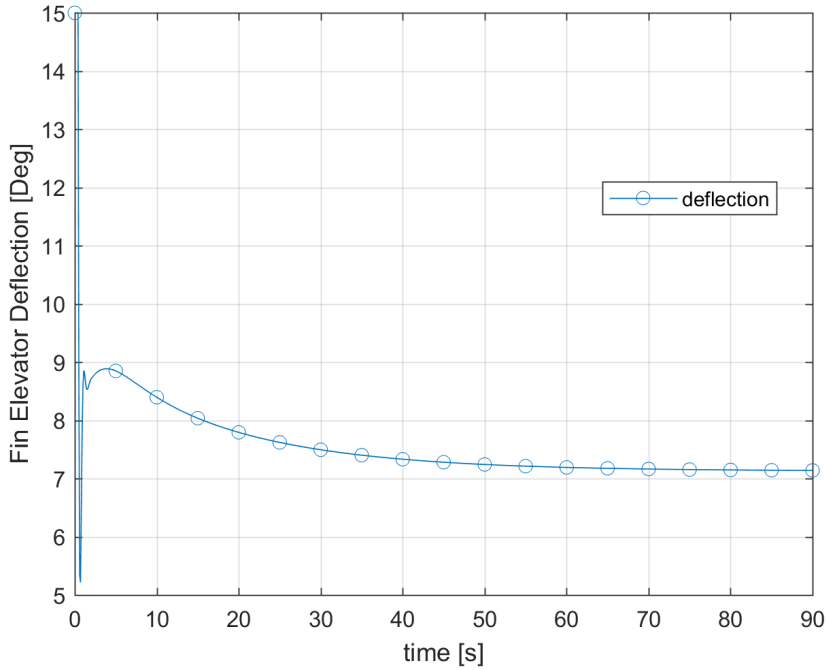

Figure A.5.18: Elevator Deflection of The Tail Fins During Positive Angle Of Attack Test Without Propeller Torque

As seen in Figure A.5.18 the tail fin deflections reach up to 15 degrees first, then comes to the equilibrium state after 80 seconds. It's also seen that the vehicle exceeds the pitch of 90 degrees, this is also normal when the elevator deflection is considered.

A.6 Roll over test

In this test, it is aimed to see the effect of the eccentricity of the model in both y and z directions. In this test, the CG of the vehicle is located at z=-0.0196 and y=0.0196 stations. This location of the CG makes the vehicle unstable in the roll axis. Since the CG is eccentric with a negative 45 degree in the roll direction, the vehicle is expected to have a final position of 135 degrees of positive roll. In order to better understand the effect of the location of the CG to the roll movement, the propeller torque is not included in the calculations and initial roll orientation is defined as "zero" in three directions. The results are presented in Figure A.6.1 through Figure A.6.8 .

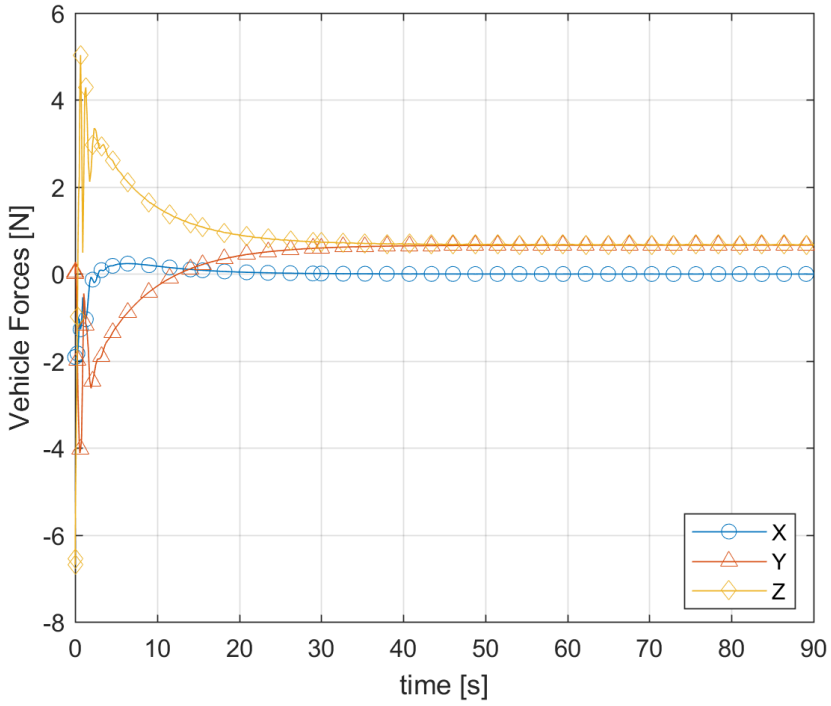

Figure A.6.1: The forces acting on the body during roll-over test

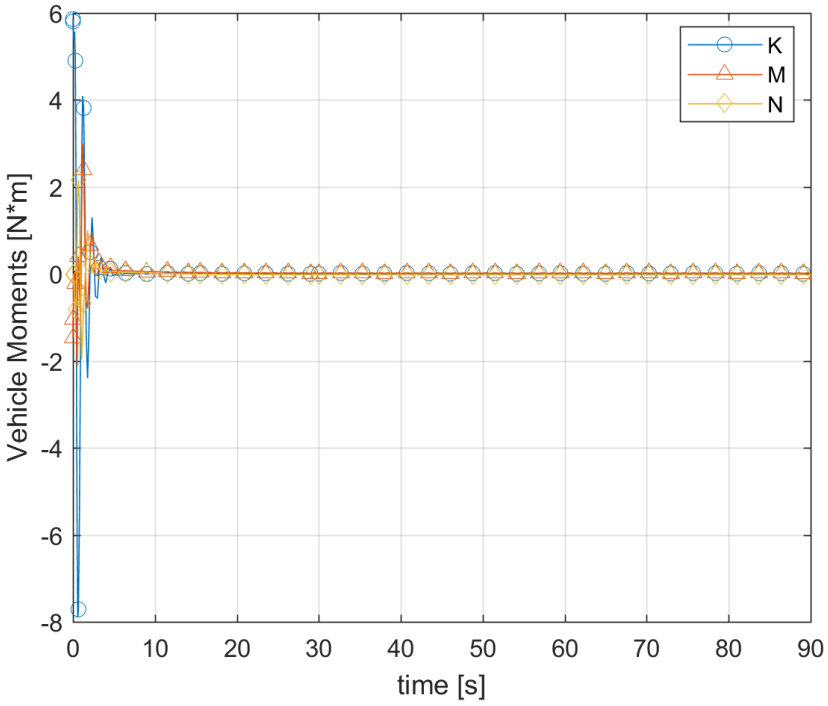

Figure A.6.2: Moments acting on the body during roll-over test

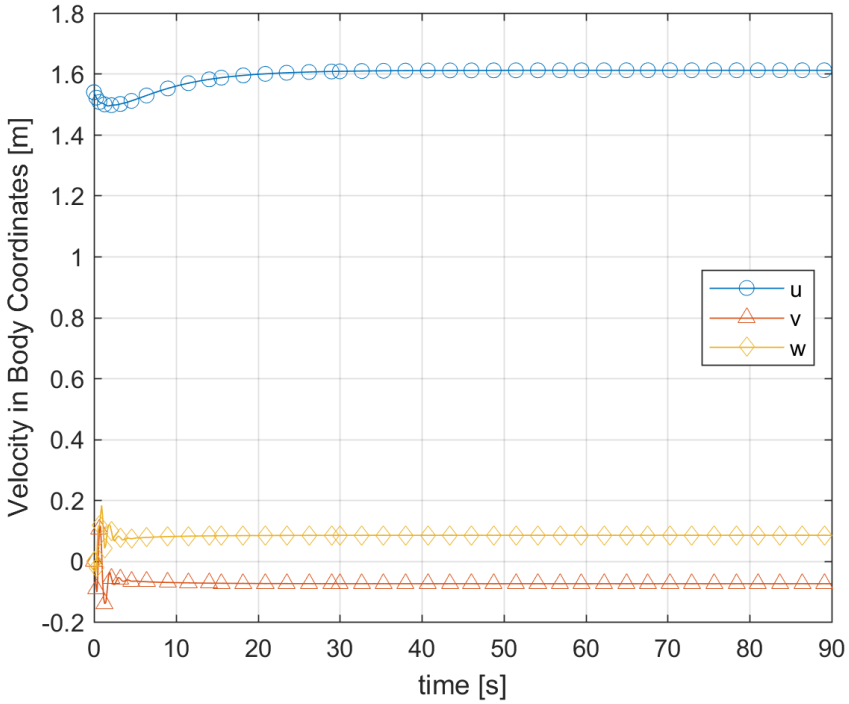

Figure A.6.3: Velocities in body axis during roll-over test

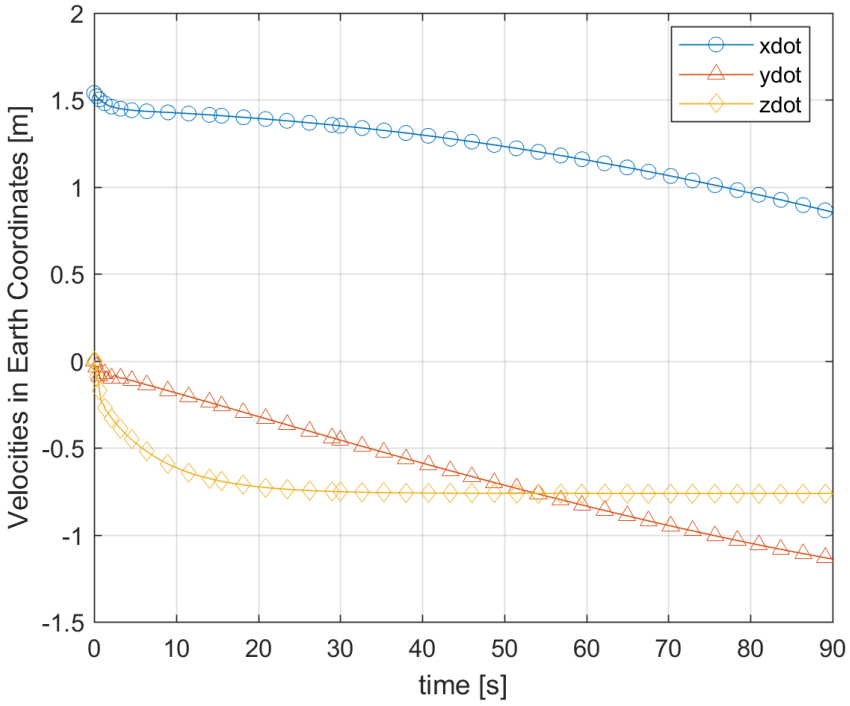

Figure A.6.4: Velocities in earth coordinates during roll-over motion

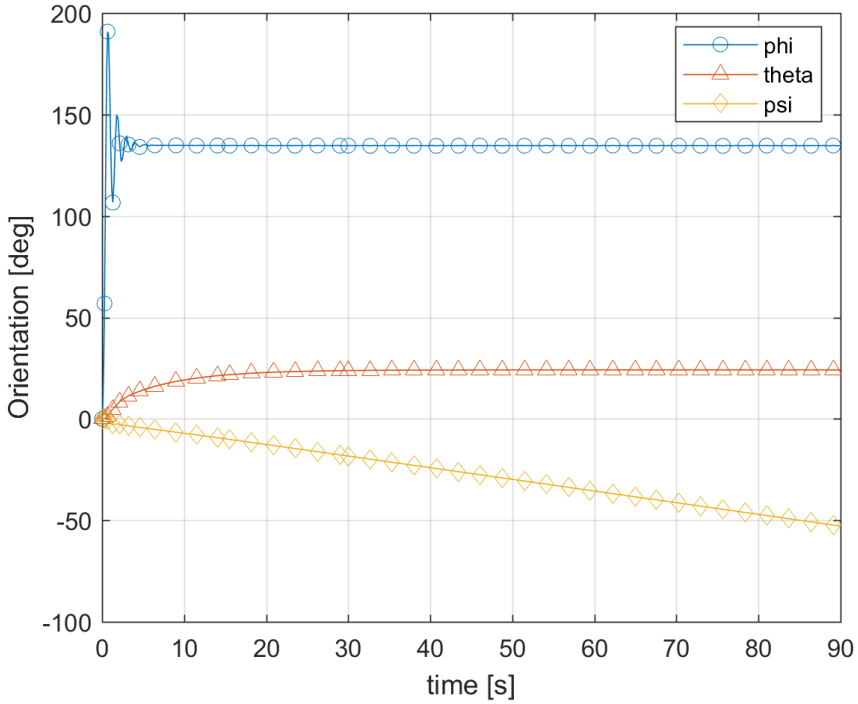

Figure A.6.5: Orientation of the body during roll-over test

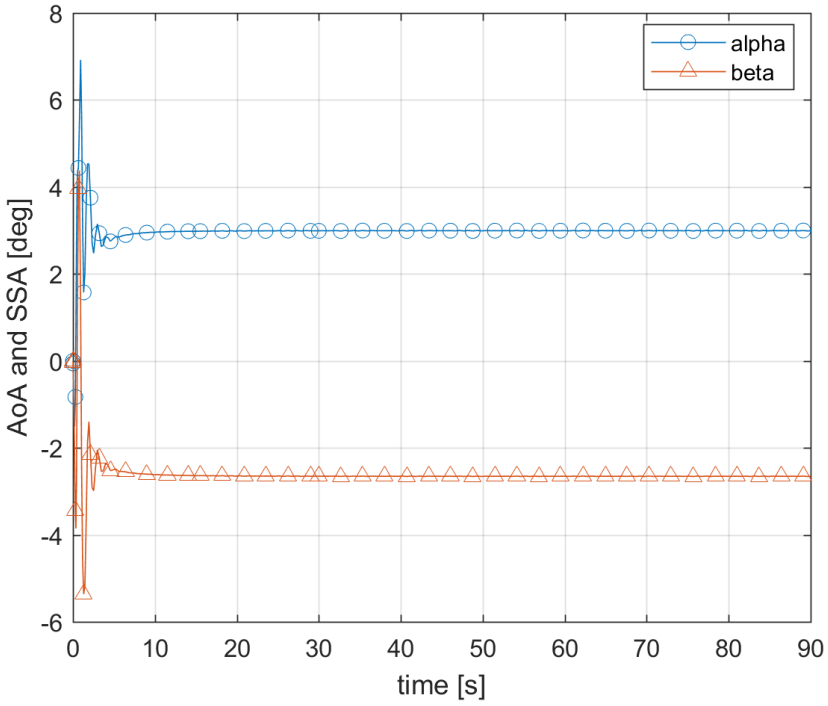

Figure A.6.6: Angles of attack and sideslip during roll-over test

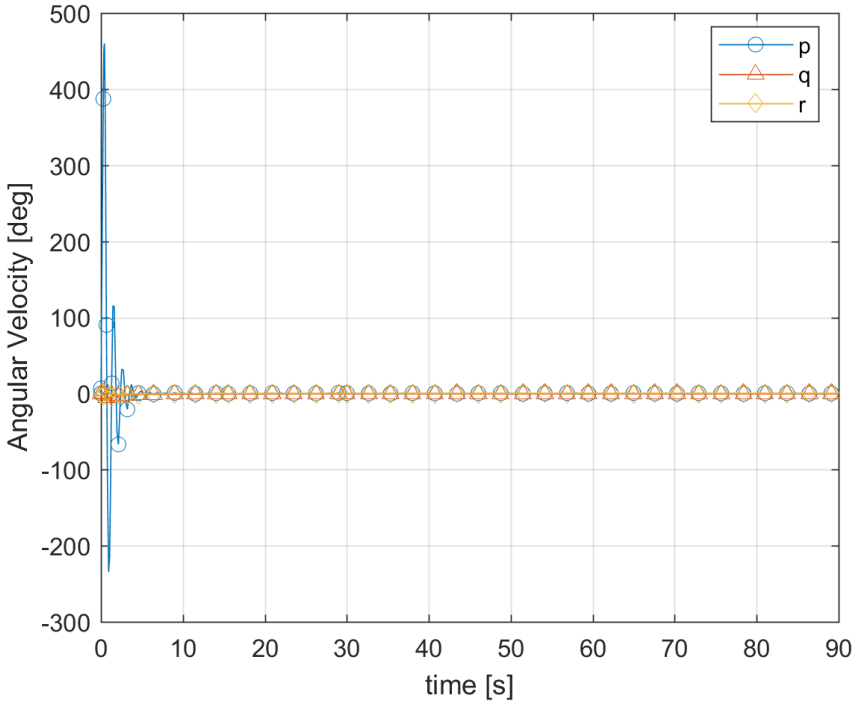

Figure A.6.7: Angular velocities of the body during roll-over test

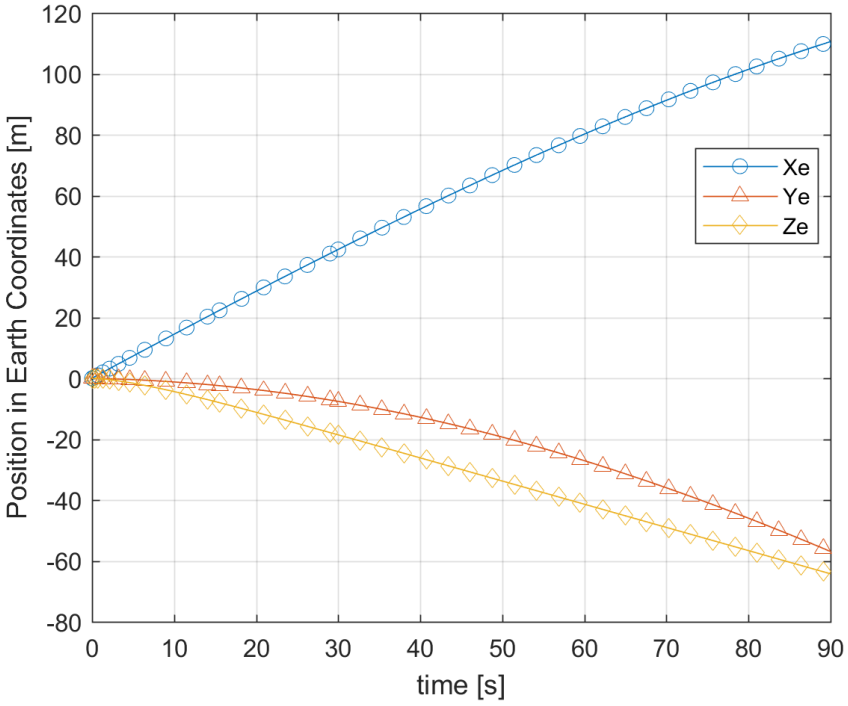

Figure A.6.8: Position of the vehicle during roll-over test

Results are satisfactory, when the expectations of having positive 135 degrees of roll is met.